CERN-THESIS-2012-378

Jet multiplicities in the $W \to \mu\nu_\mu$ process in proton-proton collisions at 7 TeV

ISBN: 978-94-6191-517-7

About the front cover: A close look at a plot somewhere in this thesis.

Dit werk maakt deel uit van het onderzoekprogramma van de Stichting voor Fundamenteel Onderzoek der Materie (FOM), die deel uit maakt van de Nederlandse Organisatie voor Wetenschappelijk Onderzoek (NWO).

Jet multiplicities in the $W \to \mu\nu_\mu$ process in proton-proton collisions at 7 TeV

Proefschrift

ter verkrijging van de graad van doctor
aan de Radboud Universiteit Nijmegen
op gezag van rector magnificus prof. mr. S.C.J.J. Kortmann,
volgens besluit van het college van decanen
in het openbaar te verdedigen op donderdag 29 november 2012
om 10.30 uur precies

door

Marcel Johannes Petrus Raas

geboren op 16 mei 1983
te Doetinchem

Promotor:	Prof. dr. N. de Groot
Copromotor:	Dr. F. Filthaut
Manuscriptcommissie:	Prof. dr. D. Froidevaux
	Prof. dr. A. Achterberg
	Prof. dr. J.F.J. van den Brand — Vrije Universiteit Amsterdam
	Dr. C.W.J.P. Timmermans
	Dr. M. Vreeswijk — Universiteit van Amsterdam

Contents

1 Introduction

Since ancient times people have wondered about the origin of matter. The ancient Greek philosophers argued that there were four elementary substances: fire, earth, air and water. These considerations were purely rational and the scientific method of testing this hypothesis experimentally was not yet agreed upon. It is therefore not a great wonder that the ancient philosophers were proven wrong.

Nowadays we believe to have a good understanding of the origin of matter. Matter is composed of a small set of elementary particles that have no substructure. The forces between these particles arise through the exchange of force carrying particles. The theoretical framework underlying these phenomena is called the standard model. In contrast to the purely theoretical argumentation of the Greeks, the standard model has been tested extensively in experiments. Whether the standard model offers a satisfactory explanation of the origin of matter can be argued, but its successes, surviving for so many years so many experiments, cannot be denied.

The success of the standard model should not blind the critical eye. Since the start of the Large Hadron Collider (LHC) in December 2009 (see Section 3.1), the frontier of experimental particle physics has been located at CERN, Geneva. One of the aims of building this collider is finding an important missing link in the standard model, the Higgs particle. But the LHC offers much more. Namely, the standard model enters the arena again. Maybe it will stand firm, maybe we find the some cracks hinting at new physics to be discovered.

1. Introduction

In the last decades a multitude of extensions of the standard model have been put forward by the theoretical community, commonly referred to as beyond the standard model (BSM) physics. The most notorious extension of the standard model is supersymmetry [1], where each elementary particle has a supersymmetric, heavy partner. The list of BSM theories is quite large: from composite Higgs models [2] to quantum gravity [3].

The first hint of the existence of an exotic BSM theory or the Higgs boson can be found by searching for a deviation of the number of events compared to what is predicted by the standard model alone. These searches are therefore heavily dependent on validity and the quality of the predictions of the standard model processes at these energies. In addition to these searches, the validity of the standard model will be re-evaluated at a higher energy through precision measurements. These measurements are the observations of the critical eyes looking at the standard model again and they are crucial for the understanding of the standard model physics and the detector.

In this thesis the critical eyes are directed towards the jet multiplicity distribution in events where a W boson decays into a muon and a neutrino. Since the W + jets process is a background to any physics search looking for a final state with a lepton and any number of non-interacting particles, it is important to understand this process. The special interest in looking at the number of jets accompanied with the W boson comes from the fact that many analyses also require a specific number of jets. This means that the predicted background yields can be off even when the inclusive cross section[1] is right.

The research for this thesis is done in two disjunct periods, the period before data taking and the period during data taking. Before data taking the detector was installed, but only a few studies assessing its performance could be done using cosmic muons. When the LHC was eventually switched on, the analyses quickly branched out. In the beginning, basic detector-level observables, like the number of detector hits per particle, were checked and the simulation was made consistent. This was then followed by measurements like the charged-particle multiplicity, the fraction of muons originating from the decay of long-lived hadrons, etc. These initial analyses are crucial for the understanding of the detector. The W + jets process is well understood theoretically and therefore it offers a good test of the validity of the standard model at these energies. Although the analysis presented in this thesis is not one of the final goals of ATLAS, it is definitely an important milestone on the road to new physics.

This thesis is organised as follows. After the introduction you are reading

[1] The inclusive cross section is irrespective any additional observable.

right now, the standard model is introduced in Chapter 2. In addition attention is given to methods and models used for the theoretical predictions that are so vital in this area. A description of the experimental setup, which consists of the 27 km long Large Hadron Collider and the biggest microscope on earth, the ATLAS detector[2], is given in Chapter 3. The reconstruction of physics objects, such as charged particles, jets, collision vertices and non-interacting particles is described in Chapter 4. Extra attention is paid to analyses measuring the performance of these algorithms. At the end of Chapter 4 in Section 4.6, a measurement of the source of muon production at the LHC is done. Chapter 5 is devoted to the identification of muons in the calorimeter. The core topic of the thesis is described in Chapter 6, where the jet multiplicity measurement in W + jets is described in detail. This is followed by concluding remarks in Chapter 7.

[2]the CMS collaboration should get some credit here as well, but ATLAS, albeit being lighter, really is bigger...

1. Introduction

2 Theoretical Introduction

2.1 The Standard Model

The standard model is the name of theoretical framework for the elementary particles. It successfully describes three fundamental forces in nature: electrodynamics, the weak interaction and the strong interaction. Most of our daily-life phenomena can be explained by electrodynamics. For instance, if we touch a table the electrons inside the atoms in our hand are repelling the electrons in atoms of the object. It manifests itself as well in chemistry. Molecules are bound states having a lower electromagnetic potential than the individual atoms. However, electrodynamics cannot explain why a nucleus is stable. At the heart of this is the strong interaction. Nucleons are composite particles containing quarks. Quarks have a special type of charge called colour charge and the corresponding force is called the strong force. As the name suggests, this force is substantial and overcomes the repelling same-sign charges of protons even in large atoms. However, not all atoms are stable and some do decay. The weak interaction is at the basis of these phenomena as well as explaining the fusion chain in our sun. Although these three forces are described to great accuracy, there is no description of gravity within the standard model.

The standard model is not suitable for making calculations for the phenomena described above. Instead, it aims at a better understanding of the microscopic processes that underlie these phenomena. The ideal way of probing the standard model is through collision experiments. Since the standard model

Lepton	Mass (MeV)	Q	Quark	Mass (MeV)	Q
ν_e	~ 0	0	u	$1.7 - 3.3$	$^2/_3$
e	0.511	-1	d	$4.1 - 5.8$	$-^1/_3$
ν_μ	~ 0	0	c	$1.29^{+0.05}_{-0.11} \times 10^3$	$^2/_3$
μ	105.65	-1	s	101^{+29}_{-21}	$-^1/_3$
ν_τ	~ 0	0	t	$4.19^{+0.18}_{-0.06} \times 10^3$	$^2/_3$
τ	1776	-1	b	$172.0^{+1.6}_{-1.6} \times 10^3$	$-^1/_3$

Table 2.1: the elementary fermions in the standard model. The masses are obtained from [4]. The quark masses are renormalised (see Section 2.1.4) in the $\overline{\text{MS}}$ scheme [5, 6]. The electrical charge Q is given in units of elementary charge.

is a quantum theory, the examination of these collisions on a microscopic scale can only be achieved through high energy experiments where the wavelengths become small. At the time when this thesis was written, the standard model has been subjected to many precision measurements and failed none of them significantly.

Throughout this section and the bulk of this thesis, the convention $c = \hbar = 1$ is used for respectively the speed of light and the Planck's constant. This implies that masses and momenta are given in units of energy.

Quantum field theory forms the basis of the standard model. The elementary particles constituting matter are described by spin-$^1/_2$ fermions, while the forces are mediated by bosons. In Table 2.1, the elementary fermions in the standard model are listed. There are three generations of leptons and three generations of quarks. The neutrinos masses are very small and only an upper limit of 2 eV can be set. The particle in a higher generation has a higher mass than a particle in a lower generation, but is completely identical apart from that. Since no evidence is found for substructure of these particles, they are called elementary.

The gauge bosons in the standard model carry the forces and are listed in Table 2.2, together with the corresponding name of the force. All the bosons listed in the table have their spins equal to 1. The photon and gluon are massless, but the W and Z bosons have masses of 80.4 GeV and 91.2 GeV, respectively.

The Lagrangian of the standard model will be derived in the following subsections. Using the Lagrangian, transition probabilities between quantum mechanical states can be calculated using perturbation theory. A detailed treatment of the derivation of the perturbation theory rules can be found in [7, 8].

Name	Force	Elec. charge
Photon	Electromagnetism	0
W boson	Weak force	± 1
Z boson	Weak force	0
Gluon	Strong force	0

Table 2.2: the elementary bosons in the standard model.

2.1.1 QED

Quantum electrodynamics is the simplest theory in the standard model and describes the interactions of charged fermions with photons. The fields describing spin-1/2 fermions, $\psi(x)$, are Dirac fields and therefore have the following Lagrangian density, $\mathcal{L}$:

$$\mathcal{L} = \overline{\psi}(x)(i\gamma_\mu \partial^\mu - m)\psi(x), \tag{2.1}$$

where γ_μ are the Dirac matrices and m is the fermion mass. Indeed, applying the Euler-Lagrange equations to Eq. 2.1 yields the Dirac equation:

$$(i\gamma_\mu \partial^\mu - m)\psi(x) = 0. \tag{2.2}$$

Eq. 2.1 is invariant under a global phase rotation:

$$\psi \rightarrow e^{i\alpha}\psi, \quad \text{with} \quad \alpha \in \mathbb{R}. \tag{2.3}$$

Now it is postulated that the Lagrangian should in fact be invariant under a local phase rotation,

$$\psi \rightarrow e^{i\alpha(x)}\psi, \quad \text{with} \quad \alpha(x) \in \mathbb{R}, \tag{2.4}$$

which in fact is not the case since the ∂^μ operator does not commute with the $e^{i\alpha(x)}$ term. By introducing the covariant derivative

$$D^\mu = \partial^\mu - ieA^\mu(x), \tag{2.5}$$

we see that the Lagrangian is invariant:

$$\mathcal{L} = \overline{\psi}(x)e^{-i\alpha(x)}(i\gamma_\mu D^\mu - m)e^{i\alpha(x)}\psi(x) \tag{2.6}$$

if the vector field A^μ transforms as:

$$A^\mu(x) \rightarrow A^\mu(x) - \frac{1}{e}\partial^\mu \alpha(x). \tag{2.7}$$

This can easily be seen by realising that the only non-commuting term encountered is the $\partial^\mu e^{i\alpha(x)}$ when shifting the $e^{i\alpha(x)}$ term to the left in order to cancel the $e^{-i\alpha(x)}$ term. If we explicitly write out the covariant derivative,

$$\mathcal{L} = \overline{\psi}(x)(i\gamma_\mu\partial^\mu - m)\psi(x) - ie\overline{\psi}(x)A^\mu(x)\psi(x), \tag{2.8}$$

we see that an interaction term is added to the original Lagrangian density from Eq. 2.1. In this case it describes the interaction between a vector field, which shall later be identified with the photon, and a fermion field. The coupling strength e is the electric charge in QED. The QED Lagrangian is finalised by also including a kinetic term for the photon:

$$\mathcal{L}_{\text{QED}} = \overline{\psi}(x)(i\gamma_\mu\partial^\mu - m)\psi(x) - ie\overline{\psi}(x)\gamma_\mu A^\mu(x)\psi(x) - \frac{1}{4}F_{\mu\nu}F^{\mu\nu}, \tag{2.9}$$

where

$$F_{\mu\nu} = \partial_\mu A_\nu - \partial_\nu A_\mu. \tag{2.10}$$

Summarising, the QED Lagrangian is of the form:

$$\mathcal{L}_{\text{QED}} = \mathcal{L}_{\text{fermion}} + \mathcal{L}_{\text{interaction}} + \mathcal{L}_{\text{photon}} \tag{2.11}$$

It should be noted that the Maxwell equations are obtained by applying Euler-Lagrange equations to the $\mathcal{L}_{\text{photon}}$ term.

2.1.2 Non-Abelian Gauge Theories

QED is an example of a gauge theory. The Lagrangian is postulated to be invariant under a local gauge symmetry, which in QED is the unitary, abelian group $U(1)$. In the standard model there are two additional symmetry groups: $SU(2)$, for the weak interaction and $SU(3)$ for the strong interaction. The general idea from QED still remains, but Eq. 2.4 takes on the more general form:

$$\psi \rightarrow e^{iT^a\omega^a}\psi, \tag{2.12}$$

with T_a the generators of the corresponding symmetry group and ω_a are real parameters. It should be noted that the exponent now is a matrix and that the fields are vectors from the fundamental representation of the symmetry group. For $SU(2)$ there are three generators, usually represented with the Pauli matrices. For $SU(3)$ the eight Gell-Mann matrices are a common representation. The

covariant derivative can be derived after requiring 2.12 to leave the Lagrangian invariant under gauge transformations, in a similar fashion as in the QED case:

$$D_\mu \quad = \quad \partial_\mu - igT^a A^a_\mu. \tag{2.13}$$

Contrary to the QED case, multiple gauge fields A^a_μ appear. In $SU(2)$, three gauge fields are introduced, while in $SU(3)$, one finds eight gauge fields. This can only be satisfied if under infinitesimal transformations the gauge fields transform as

$$A^a_\mu \quad \rightarrow \quad A^a_\mu + \frac{1}{g}\partial_\mu \omega^a - f^{abc}\omega^b A^c_\mu, \tag{2.14}$$

where f^{abc} are the structure constants defining the Lie algebra of the corresponding group. In order to preserve the local invariance, the gauge tensor has to modified:

$$\mathcal{L}_{\text{gauge fields}} \quad = \quad \frac{1}{4}F^a_{\mu\nu}F^{a\mu\nu}, \tag{2.15}$$

$$F^a_{\mu\nu} \quad = \quad \partial_\mu A^a_\nu - \partial_\nu A^a_\mu + g f^{abc} A^b_\mu A^c_\nu. \tag{2.16}$$

Notice that the Lagrangian now contains cubic and quartic gauge field terms. This in turn implies gauge boson self interactions, which do not occur in abelian QED.

2.1.3 Electroweak Interactions

In the weak interaction, the $SU(2)$ gauge symmetry works only on the left-handed chirality eigenstates of the fermions. A projection on these eigenstates is given by

$$\psi_{\text{L}} \quad = \quad \frac{1}{2}(1-\gamma^5)\psi, \tag{2.17}$$

$$\psi_{\text{R}} \quad = \quad \frac{1}{2}(1+\gamma^5)\psi. \tag{2.18}$$

Each left-handed neutrino and its lepton partner form a two-dimensional $SU(2)$ representation

$$\begin{pmatrix} \nu_l \\ l \end{pmatrix}, \tag{2.19}$$

called an isospin-1/2 doublet.[1] The doublets are not restricted to the lepton sector: also the left-handed quarks are arranged in doublets, as shown in Table 2.3. The up-type quarks q_{u} are the u, c and t quarks, while the down-type quarks q_{d} are the d, s and b quarks. The isospin quantum number, T, is 1/2 for the left-handed doublets and zero for the right-handed singlets. The third component of isospin, T_3, is also displayed. The up-type neutrinos and quarks have $T_3 = 1/2$, while the down-type leptons and quarks have $T_3 = -1/2$. The hypercharge, Y, relates electromagnetic charge and the third component of isospin:

$$Q = T_3 + \frac{Y}{2}. \tag{2.20}$$

It is on the left-handed doublets that the $SU(2)$ gauge invariance, explained in Section 2.1.2, is required.[2] The symmetry group for the electroweak interactions is $SU(2)_{\mathrm{L}} \times U(1)_Y$. Following the derivation of the covariant derivative, see Eq. 2.13, we find three gauge fields for $SU(2)$ and one gauge field for the hypercharge symmetry:

$$D_\mu \;=\; \partial_\mu + i\frac{g}{2}\sigma^a W_\mu^a + i\frac{g'}{2} Y B_\mu, \tag{2.21}$$

with gauge couplings g and g'. The Lagrangian we can construct at this point is given by:

$$\begin{aligned} \mathcal{L}_{\mathrm{EW}} \;=\; & \sum_i \overline{\psi}_{\mathrm{L}i} i\gamma^\mu D_\mu \psi_{\mathrm{L}i} + \sum_i \overline{\psi}_{\mathrm{R}i} i\gamma^\mu D'_\mu \psi_{\mathrm{R}i} \\ & -\frac{1}{4} W^{a\mu\nu} W^a_{\mu\nu} - \frac{1}{4} B^{\mu\nu} B_{\mu\nu}, \end{aligned} \tag{2.22}$$

where $W^{a\mu\nu}$ is defined as in Eq. 2.16 and $B^{\mu\nu}$ as in Eq. 2.10. The covariant derivative for the right-handed sector D'_μ is similar to Eq. 2.21 but does not contain the $SU(2)$ specific $i\frac{g}{2}\sigma^a W_\mu^a$ term. Note that the weak gauge fields do not have mass terms and that the fermion masses have been omitted since the $m\overline{\psi}\psi$ term contains terms like $\overline{\psi}_{\mathrm{R}}\psi_{\mathrm{L}}$. These terms are problematic since they have an incompatible inner product between an isospin doublet and an isospin singlet.

This is where the Higgs fields comes to the rescue [9, 10, 11]. The Higgs field is defined as a complex scalar field (spin-0) and has an isospin of 1/2:

$$\Phi \;=\; \frac{1}{\sqrt{2}} \begin{pmatrix} \phi_0 + i\phi_1 \\ \phi_2 + i\phi_3 \end{pmatrix}, \tag{2.23}$$

[1] The term isospin refers to the fact that it resembles spin, which also described by the $SU(2)$ symmetry group.

[2] Actually, the $SU(2)$ symmetry works trivially on the right handed singlets.

Type	Symbol	Elec. charge	T	T_3	Hypercharge
leptons	$\begin{pmatrix} \nu_l \\ l \end{pmatrix}_{\mathrm{L}}$	0	1/2	1/2	-1
		-1	1/2	-1/2	-1
	l_{R}	-1	0	0	-2
quarks	$\begin{pmatrix} q_{\mathrm{u}} \\ q_{\mathrm{d}} \end{pmatrix}_{\mathrm{L}}$	2/3	1/2	1/2	1/3
		-1/3	1/2	-1/2	1/3
	q_{uR}	2/3	0	0	4/3
	q_{dR}	-1/3	0	0	-2/3

Table 2.3: the quantum numbers of the fermions in the standard model.

where ϕ_i are real-valued fields. The Lagrangian of the Higgs field is

$$\mathcal{L}_{\mathrm{Higgs}} = (\partial^\mu \Phi)^\dagger \partial_\mu \Phi + V(\Phi), \tag{2.24}$$

where the potential due to self interactions:

$$V(\Phi) = \mu^2 |\Phi|^2 + \lambda |\Phi|^4, \tag{2.25}$$

has the famous Mexican-hat shape if $\mu^2 < 0$ and $\lambda > 0$. With these conditions for μ^2 and λ, the global minimum is then located at a non-zero value of

$$|\Phi|^2 = \frac{1}{2} v^2 = -\frac{\mu^2}{2\lambda},$$

which can be interpreted as a non-zero vacuum expectation value of the Higgs field. Since the Mexican-hat potential is invariant under rotations, we can rewrite the Φ field as:

$$\Phi = \frac{1}{\sqrt{2}} \begin{pmatrix} \phi_0 + i\phi_1 \\ v + H(x) + i\phi_3 \end{pmatrix}, \tag{2.26}$$

where we see through substitution in Eq. 2.24 that there are three massless real-valued fields (Goldstone bosons) and one massive, real-valued field $H(x)$. Interaction terms quadratic in the non-abelian gauge fields with the vacuum expectation value v show up by diagonalising the gauge fields in their mass eigenstates:

$$\begin{aligned} W_\mu^\pm &= \frac{1}{\sqrt{2}} \left(W_\mu^1 \mp i W_\mu^2 \right); \\ Z^\mu &= \cos\theta_W W_\mu^3 + \sin\theta_W B_\mu; \\ A^\mu &= -\sin\theta_W W_\mu^3 + \cos\theta_W B_\mu. \end{aligned}$$

Here the massive $W^{\pm}$ and Z bosons and the massless photon (A^{μ}) are identified. The weak-mixing angle is defined as $\tan\theta_W = g'/g$. Here the $W^{\pm}$ and Z fields have acquired mass. The degrees of freedom needed for the longitudinal polarisation of the massive $W^{\pm}$ and Z bosons can be shown to be provided by the three massless Goldstone bosons. The masses of the W and Z bosons are related to the vacuum expectation value v as follows:

$$\begin{aligned} m_{W^{\pm}} &= \frac{v}{2}g, \\ m_Z &= \frac{v}{2}\sqrt{g^2+g'^2}. \end{aligned}$$

The three degrees of freedom from the massless, scalar bosons in the Higgs doublet can be shown to be absorbed as longitudinal helicity states of the massive vector bosons. In addition, a scalar boson with mass $\sqrt{\lambda}v$, called the Higgs boson, is predicted.

The Higgs field Φ offers a solution for the previously problematic couplings between the left-handed doublets and the right-handed singlets of the form $\overline{\psi}_L\psi_R$ by introducing the following coupling between the fermion field and the Higgs field:

$$\lambda_{f_d}\Psi_L^{\dagger}\Phi\psi_R^d - i\sigma_2\lambda_{f_u}\Psi_L^{\dagger}\Phi^*\psi_R^u. \tag{2.27}$$

Note that $\psi_L^{\dagger}\Phi\psi_R^{u/d}$ is a well defined inner product now. The up and down fields are represented in the doublet representation of the fermion field, Ψ_L. Since there are no right-handed neutrinos, the second term is only available for the quark fields. These coupling are called the Yukawa couplings. They provide mass terms for the fermions, with the masses given by $m_f = \lambda_f v/\sqrt{2}$.

In the weak interaction, the interaction eigenstates (denoted with a prime) of the quarks mix with the mass eigenstates:

$$\begin{pmatrix} d' \\ s' \\ b' \end{pmatrix} = V_{\mathrm{CKM}} \begin{pmatrix} d \\ s \\ b \end{pmatrix}, \tag{2.28}$$

where V_{CKM} is the unitary CKM (Cabbibo-Kobyashi-Maskawa) matrix [12, 13], and d, s and b are the mass eigenstates of the quark's fermion fields. Similarly the neutrino interaction states are mixed with the neutrino mass states via the Pontecorvo-Maki-Nakagawa-Sakata matrix [14]. The neutrino mixing can be safely ignored for the physics studied in this thesis.

2.1.4 QCD

Besides electrical charge and isospin, quarks have another type of charge called colour charge. The quark fermion field is written in the fundamental representation as:

$$q_i = (q_{i,\mathrm{r}}, q_{i,\mathrm{g}}, q_{i,\mathrm{b}}), \tag{2.29}$$

where, 'r' stands for red, 'g' stands for green and 'b' stands for blue[3] and q_i can be any quark (up-type, down-type and any generation). The covariant derivative leads to eight massless gauge fields called gluons. The QCD Lagrangian is described in Section 2.1.2 where the local, non-abelian $SU(3)$ symmetry is imposed.

Calculations in QFT can proceed perturbatively, expanding in the coupling parameter, or by lattice calculations of the Feynman path integral [7]. In perturbation theory one finds that loop diagrams are divergent. These divergences are regulated by an unphysical parameter μ. Of course, physical predictions should not depend on this parameter. This is called the renormalisation condition. The renormalisation group equations require that any observable σ is independent of μ:

$$\mu \frac{\mathrm{d}\sigma}{\mathrm{d}\mu} \quad = \quad 0. \tag{2.30}$$

The coupling parameter obtains an energy-scale dependence through these renormalisation equations. This renormalisation scale is commonly denoted as μ_R. For a more detailed treatment of renormalisation consult [7, 8].

The QCD fine-structure constant $\alpha_s = g^2/4\pi$ obtains the following dependence through the renormalisation equations:

$$\alpha_s(\mu_R) \quad = \quad \frac{12\pi}{(11N_c - 2N_f)\log(\mu_R^2/\Lambda_{\mathrm{QCD}}^2)}. \tag{2.31}$$

Here N_f is the number of active flavours[4], $N_c = 3$ the number of colour charges and Λ_{QCD} sets the scale and is measured to be approximately 200 MeV. From Eq. 2.31 we see that the coupling increases at lower energy transfers, while it decreases at a higher scale. This is a direct result of the non-abelian, self interactions of the gluon. At low energies, QCD calculations cannot be done

[3] The use of colours is merely pedagogical and in fact has no relation to QED at all.

[4] Quarks flavours with masses much larger than the typical energy scale of the process can be ignored.

perturbatively anymore and the physics is described by phenomenological models. A similar procedure can be followed for the couplings in the electroweak interaction. The weak-coupling strength and the electromagnetic charge have the opposite behaviour and increase at higher energies.

The dependence of α_s on the energy scale has two important implications on the phenomenology of QCD interactions:

Asymptotic freedom: at high energy transfers, quarks and gluons have a very weak interaction;

Confinement: colour charge can never be isolated. As the distance between two coloured objects increases, the colour field strength between them increases up until the point where it becomes energetically favoured to split the field into a quark-antiquark pair. Eventually these quark pairs form colour-neutral hadrons.

2.2 Event Generation

Event generators are important tools for making predictions in the field of experimental high energy physics. These generators calculate scattering-matrix elements and use Monte Carlo techniques in order to arrive at representative distributions. An event generator produces a collection of four-momenta together with the particle type (pion, proton, muon, etc.) of every particle generated in the event. An example of such an event record is the `HepMC` event record which is described in [15]. There are many different event generators, some of them are general-purpose generators, like `Pythia` [16] and `HERWIG` [17, 18], while others are specialised in a subset of processes.

Only the hard scattering is calculated perturbatively and many factors complicate the event generation. In Figure 2.1 a schematic illustration of a pp collision is shown. In the middle, from both sides the incoming protons are shown. Since the protons are a confined state of three quarks, perturbation theory is not valid there. The implications for the event generation is discussed in Section 2.2.1. In the middle of the picture is the hard scattering (HS). In this case two gluons collide and produce at $t\bar{t}$ pair accompanied by a Higgs boson (indicated by the dashed line). The decay can be traced by following the graph outwards to the top. Both tops decay via the emission of a W boson, where the right W boson decays into a lepton-neutrino pair.

Coloured objects (quarks and gluons) are never measured directly due to confinement. Instead they form bunches of (stable) hadrons, called jets. The

first step in jet formation is the radiation of gluons and gluon splitting, called the parton shower. This process is modelled by a parton showering (PS) algorithm since the matrix-element computation is too complicated. This is discussed in Section 2.2.2. Note that not only the outgoing, but also the incoming coloured objects are subjected to parton showering. The non-perturbative recombination of quarks into hadrons (indicated by Frag., from fragmentation) is covered in Section 2.2.3. This is followed by the modelling of the decay of the unstable hadrons formed in this process.

The underlying event, displayed at the bottom of the figure, is covered in Section 2.2.4.

The cross sections of many important physics channels have been calculated as a function of the centre-of-mass energy and are shown in Figure 2.2. The low-energy part of the curve indicates $p\bar{p}$ cross sections while the high-energy part of the curve indicates pp cross sections, which explains the discontinuity. This is done in order to compare Tevatron [19] predictions with LHC predictions [20] (see Section 3.1).

2.2.1 Parton Distribution Functions

At the LHC protons collide with protons, which themselves are not elementary particles. The proton is a complicated bound state of three quarks uud. Besides these three valence quarks the proton contains gluons and quark-antiquark pairs (sea quarks). An elementary constituent of the proton is called a parton. The hard interaction in a proton-proton collision is initiated by two partons, one from each proton. The probability of finding parton i in hadron h with a momentum fraction x is given by the parton distribution function, commonly denoted as $\phi_{i/h}(x)$. The calculation of a cross-section for $pp \to f$, where f is some final state consisting of elementary particles can then be factorised:

$$\sigma_{pp\to f} = \sum_{i,j} \int_0^1 \mathrm{d}x_0 \int_0^1 \mathrm{d}x_1 \phi_{i/h}(x_0, \mu_f)\phi_{j/h}(x_1, \mu_f)\sigma_{ij}(x_0 p, x_1 p, \mu_f), \tag{2.32}$$

where i and j denote the colliding parton types and p is the momentum of the proton in the centre-of-mass frame. The factorisation scale, μ_f, is included in order to separate the non-perturbative processes in the proton from the hard scattering. Like the renormalisation scale, this scale is not physical and the results should have a minimal dependence on μ_f. Any relic dependence of calculated observables is treated as a theoretical uncertainty. Leading order

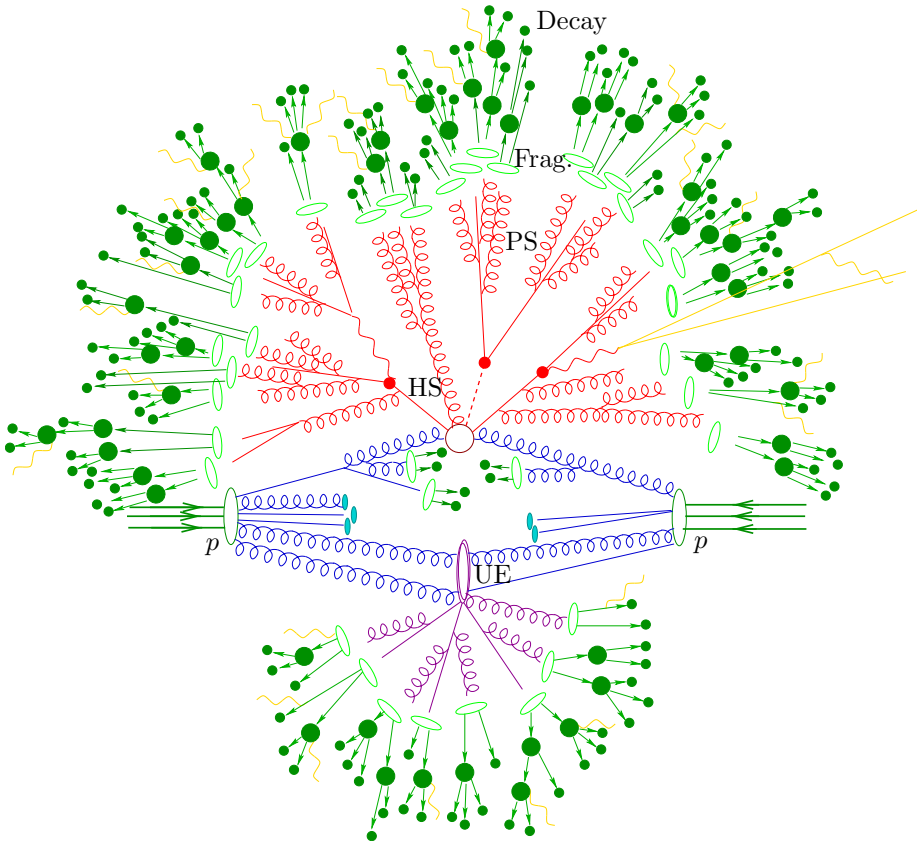

Figure 2.1: a typical collision of two protons at the LHC (figure taken from [21]).

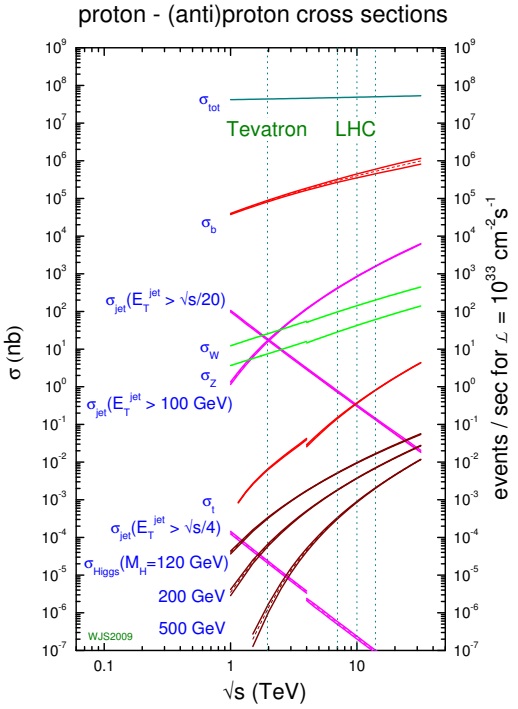

Figure 2.2: cross sections for various processes at a hadron collider as function of the centre-of-mass energy. The discontinuity comes from the fact that the low-energy part of the curve is dedicated to $p\overline{p}$ collisions (figure taken from [22]).

results usually have a larger dependence on the arbitrary scale than higher order calculations.

2.2.2 Parton Showers

When calculating the matrix element for initial- or final-state radiation one encounters the problem of a divergent contribution if the opening angle is small or the momentum of the radiated parton is zero. These divergences are called collinear or soft divergences, respectively. This divergent part cancels the virtual contributions of the loop diagrams of the same order. Since the loop calculations become increasingly difficult with more loops, the parton shower is a solution to model the initial- and final-state radiation.

The parton shower performs a number of branchings on an initial- or final-state parton. For instance, a quark can radiate a gluon: $q \to qg$. A gluon can split into a gluon pair or a quark pair: $g \to gg$, $g \to q\overline{q}$. From these branchings a tree of partons is constructed. These emissions are controlled by some 'time-ordering' variable, which ensures that the next branching has less energy transfer than the previous one. `HERWIG` uses the angle between the created partons and its parent, while `Pythia` uses the virtuality of the parton.[5] Eventually the parton shower evolves into the non-perturbative regime, and the evolution of the parton shower is terminated.

Parton showers neglect interference and helicity structure. They do a good job at describing the jet substructure, but one should not rely on their predictions of events where multiple hard jets are produced by the parton shower. For more information on parton showering algorithms consult [7]. Although the parton showering is only described here in terms of coloured objects, it should be noted that for electromagnetic radiation similar procedures are applied.

Matching Methods

Matrix-element calculations require the inclusion of loop diagrams in order to describe radiation since at the tree level they suffer from soft and collinear divergences. However, hybrid methods divide the phase space into two realms: the higher p_{T} realm[6] is covered by the tree-level matrix element while the lower

[5] In `Pythia` the virtuality increases for initial-state radiation, while for final-state radiation it decreases.

[6] p_{T} denotes the transverse momentum relative to the radiating parton. In the literature it is often denoted by $p_{\perp}$.

p_T realm is covered by a parton shower algorithm. This works since for high-p_T radiated partons the virtual contribution can be neglected. The problem with this approach is that the parton shower can produce partons that have an overlap with the matrix element. The CKKW and MLM [23, 24, 25] matching schemes resolve this ambiguity. The MLM matching scheme is used for the predictions in Chapter 6.

2.2.3 Hadronisation/Fragmentation

The final state is not fully developed after the parton shower, since coloured objects are not directly observed. Instead, the quarks and gluons form hadron bound states. At this point perturbative QCD is not longer valid and only phenomenological models are able to describe what happens next. Below the string fragmentation model is outlined. A nice generic description of fragmentation/hadronisation models is given in [7]. For more information on the cluster model implemented in `HERWIG` see [17]. A detailed description of string fragmentation can be found in [16].

The string-fragmentation model owes its name to the tube-like shape of the colour field between two quarks. Since the colour field induces a potential between two outgoing quarks which increases with distance, it becomes energetically favoured to split the gluon field in a quark-antiquark pair. The string break-ups continue until only groups of colour neutral $q\bar{q}'$ exist. These quark-antiquark pairs are subsequently merged into mesons.

It is also possible to create a quark-antiquark pair with a colour that differs from the colour field between the two outgoing quarks. Since it does not break up the colour field, it is not energetically favoured. However, it is not prohibited due to fluctuations. In this case the colour of the field is effectively changed. The colour of the field is then complementary to the colours of the quarks, e.g. if the quarks are red and green, the field will be blue-antiblue[7]. If this colour field breaks into a quark-antiquark pair, there are three quarks and three antiquarks, all having a different colour, thus making a colour-singlet state. These groups can then form baryons.

2.2.4 Underlying Event

Since the interacting protons have donated one of their partons to the hard scattering these beam remnants are not colour neutral anymore. Albeit usually

[7]Note that there are antiquarks with antired and antigreen colour charges on the other side of the string.

at a lower energy than the hard scattering, they also interact and can produce forward jets. This process is called the underlying event. When the final state of the hard scattering is not colour neutral, the final state particles of the hard interaction connect with colour flow of the underlying event. In some cases there are multiple parton interactions which means that two partons from the beam remnants collide in a similar way as the hard interaction.

3 Experimental Setup

The experimental setup is located near Geneva, Switzerland, at the European organisation for nuclear research, CERN. The results described in this thesis are obtained by analysing data from the ATLAS[1] experiment, which is one of the four experiments that study the physics from the colliding beams delivered by the Large Hadron Collider (LHC). A concise description of the collider will be given in Section 3.1, and in Section 3.2 the important aspects of the detector will be presented.

3.1 The Large Hadron Collider

The Large Hadron Collider is a superconducting synchrotron collider able to accelerate protons to a centre-of-mass energy up to 7 TeV and is expected to reach its design energy of 14 TeV in the near future. Being the highest energy collider at the moment, the LHC can probe the standard model in an unchartered energy regime. Due to the higher energy it is expected that many questions in high energy physics can be resolved.

The LHC is not only pushing the current energy frontier for colliders. It is also designed to have the highest instantaneous luminosity in hadron collisions. Since the number of events for a certain process is given by the product of

[1] ATLAS is an acronym for **A** **T**oroidal **L**HC **A**pparatu**S**.

its cross section with the integrated luminosity over time, the rate of rare, interesting processes will be enhanced.

The high design luminosity of 10^{34} cm^{-2}s^{-1} could, with the current technology, not be achieved with $p\overline{p}$ collisions, because the production of large amounts of anti-protons is problematic, so pp collisions were taken. However, since both the clockwise and the anti-clockwise revolving particles are of the same charge, a pp collider needs two separate beam pipes. The superconducting dipole magnets, which are responsible for bending the beams, have two bores with magnetic fields anti-parallel to each other. In fact, the flux return of the dipole around one bore enhances the field strength in the other. Since the LHC is built in the tunnel that previously housed the LEP experiment [26], the most important feature of this twin-bore design [27] is that it was not needed to construct two separate proton rings. This would not have been feasible because of a lack of space.

The beam in the LHC is not a constant flow of protons. Instead, it is divided in bunches consisting of roughly 10^{11} protons. The maximum number of bunches that fit in the LHC is 2808, and this can only be achieved if the bunch spacing is 25 ns. At the interaction points the beam is squeezed and at design luminosity 22.3 interactions are expected on average in one bunch crossing. The luminosity in the 2010 data, however, is much lower and the average number of interactions per bunch crossing is 10 times lower.

The protons are accelerated in five stages before reaching their maximum energy (at 7 TeV centre-of-mass energy) of 3.5 TeV (see Figure 3.1). The protons start their journey to the LHC in the LINAC (linear accelerator) which they leave with an energy of 50 MeV. In the next step, the proton synchrotron booster injects them into the proton synchrotron at 1.4 GeV where they are accelerated to an energy of 25 GeV. The last stage, before injecting them in the LHC, takes place in the Super Proton Synchrotron which accelerates the protons to 450 GeV. In the LHC, the protons are accelerated in radio frequency (RF) cavities. With the increasing energy of the protons, the dipole fields are ramped from 0.535 T at 450 GeV to 4.17 T at 3.5 TeV.

As shown in Figure 3.2, the LHC is divided into eight sectors, each consisting of a straight section and an arc. At four points, in the straight sections, the two beams cross each other and these serve as the interaction points for the experiments. In octants three and seven collimators are installed that absorb particles with high betatron amplitudes, also reducing the momentum spread. The RF cavity, located in sector four, captures and accelerates the beam. The beam dump is installed in sector six and is able to eject the beam onto a carbon target at the end of a run or during an emergency stop.

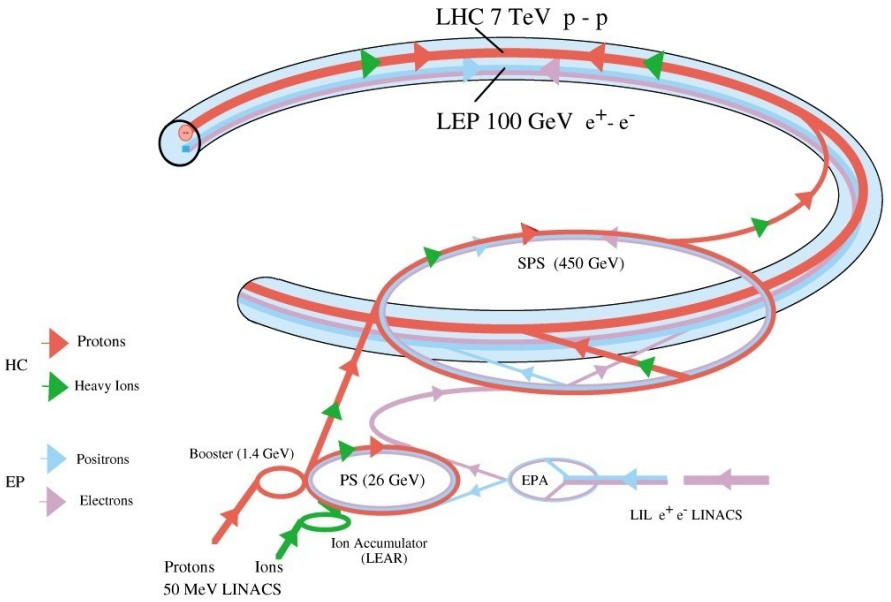

Figure 3.1: the layout of the LHC injection complex. The protons pass through the LINAC, proton booster, proton synchrotron and super proton synchrotron before they enter the LHC with an energy of 450 GeV. The layout depicted in the above picture does not resemble the true geometry (figure taken from [28]).

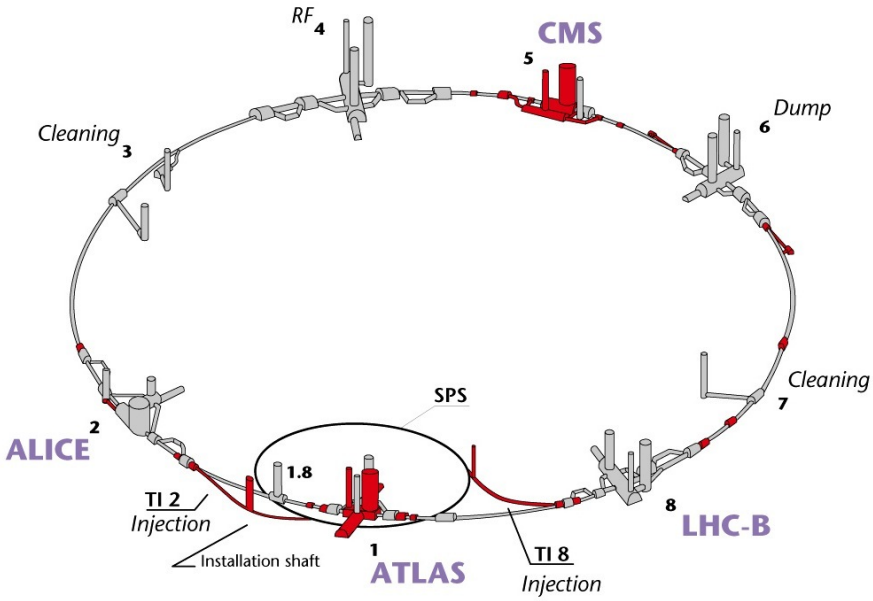

Figure 3.2: the layout of the LHC and the position of the experiments along the ring (figure taken from [29]).

There are four detectors at the LHC. Two of them are located at interaction points where the beams are squeezed maximally in order to obtain the highest luminosity. These are ATLAS and CMS [30] (compact muon solenoid). Both detectors have a similar hermetic, symmetrical, cylindrical structure and focus on discovering new particles. One detector, LHCb [31] (LHC beauty), is built specifically for precision measurement in the b-physics sector, studying CP violation in more detail. The LHC is also able to collide completely ionised lead atoms. The theory described in [32] predicts it will be possible to reach a short-lived, new phase in matter during these collisions. In this phase, called quark-gluon plasma, quarks and gluons are temporarily decoupled. The ALICE (A Large Ion Collider Experiment) detector [33] has been designed specifically for studying this type of collisions.

The tunnel for the LHC was excavated in 1983-1988 to house the Large Electron Positron (LEP) collider. Construction of the LHC and the experiments started in November 2001. In September 2008, the first proton beams were circulating in the LHC. The run in 2008 stopped after nine days since an electrical fault caused extensive damage to one of the sectors. On 20 November 2009, beams were circulated at injection energy again and first collisions followed three days later. At the 30^{th} of March 2010, the first collisions at a centre-of-mass energy of 7 TeV took place. The data used in this thesis were produced from the $\sqrt{s} = 7\,\text{TeV}$ collision data recorded by the ATLAS experiment in the year 2010.

A more extensive description of the LHC can be found in [34, 20].

3.2 The ATLAS Detector

3.2.1 Overview

The ATLAS detector is a multi-purpose detector located at one of the two high luminosity interaction points. Some of the aspects that have driven the design of the ATLAS detector are described below. More details can be found in [35].[2]

In order to make precision measurements and in order to obtain high sensitivity to new physics channels, the particle identification efficiency and the energy resolution should be, within reasonable costs, as good as technologically possible.

The high luminosity delivered by the LHC imposes design constraints as well. Due to the high particle density, the detector granularity should be very high

[2] Unless states otherwise, the figures in this section have also been taken from [35].

in order to resolve individual particles. Furthermore it is also required that the sensors and front-end electronics are able to withstand high doses of radiation. Since the minimal bunch spacing of the LHC is 25 ns, the detectors should react and recover very fast. When this cannot be achieved, the signals of subsequent collisions are superimposed. In addition, many sensitive elements need some time to recover. During this time, the detector elements are insensitive or the read-out is blocked. These effects are denoted by the term *out-of-time pile-up*.

Another design challenge has been to achieve an acceptance that covers as much of the solid angle as possible. Having a hermetic detector allows to measure all outgoing momenta, which is necessary for making an estimate of the sum of all transverse momenta. The latter is very important for reconstructing neutrinos — or yet undiscovered particles that also have a very weak interaction with the detector material — since these can only be observed from the breaking of the conservation of momentum in the transverse plane.

As it can be seen from the overview of the ATLAS detector shown in Figure 3.3, the detector is built in multiple layers, which can be divided into three categories: the inner detector (ID), the calorimeter and the muon system (MS).

The layer closest to the beam pipe, the inner detector, is able to measure the momentum of charged particles close to the interaction point. Being close to the interaction point also allows for precisely reconstructing vertices, which is vital for detecting secondary vertices. Another pile-up effect, called *in-time pile-up*, is caused by multiple interactions per bunch crossing. Being able to identify the individual vertices of these multiple interactions is a prerequisite in determining corrections for this type of pile-up (see for instance Section 4.3.1 or Section 6.2).

The calorimeter envelops the ID and can be divided into an electromagnetic calorimeter, which is built to identify photons and electrons, and a hadron calorimeter which is designed to absorb and measure the energy of hadrons.

Downstream of the calorimeter, most of the particles that interact with the detector material will have been absorbed, except muons. The muon system is built to identify these muons. Due to the precision tracking in the muon system, which enhances the muon momentum resolution for very energetic muons, the muon system sometimes is also referred to as the muon spectrometer.

Two magnet systems supply the magnetic field needed for momentum measurements of charged particles. The inner detector is surrounded by a superconducting central solenoid, which generates a homogenous field of 2 T. In the muon spectrometer the magnetic field is generated by three air-core toroid magnets having a peak field in the windings of 4 T.

Throughout this thesis the following conventions for coordinates are used.

The x-axis points to the LHC centre, the y-axis points upwards and the z-axis points anti-clockwise (eastwards) along the beam, forming a right-handed, orthogonal coordinate system. The origin of this coordinate system is located at the nominal interaction point in the centre of ATLAS. Cylindrical coordinates will be used more often because they are more convenient due to the cylindrical symmetry of ATLAS. For the azimuthal angle, $\phi = \arctan(y/x)$, the domain $[-\pi, \pi]$ is used. The polar angle is defined by $\theta = \arctan(z/r)$, with $r = \sqrt{x^2 + y^2}$. Instead of the polar angle, the pseudorapidity

$$\eta = -\log(\tan(\theta/2)) \tag{3.1}$$

is more commonly used. For relativistic particles the pseudorapidity is approximately equal to rapidity

$$y = \frac{1}{2}\log\left(\frac{E + p_z}{E - p_z}\right), \tag{3.2}$$

where E and p_z are the energy and longitudinal momentum of the particle. Since differences in y are invariant under boosts along the z-axis, y and η are preferred over θ.

3.2.2 The Inner Detector

The inner detector (ID) consists of three layers. An overview of the ID layout is shown in Figure 3.4. The innermost pixel subsystem and its surrounding semiconductor tracker (SCT) are based on semiconductor technology. They both cover the acceptance $|\eta| < 2.5$. The last layer is called the transition radiation tracker (TRT), which consists of tubes filled with a gas mixture interwoven with transition radiation foils. The acceptance of the TRT is limited to $|\eta| < 2.0$.

The Pixel Detector

Of the three layers, the pixel detector is located closest to the beam pipe. It is a highly granular detector providing three space-points for almost all trajectories of charged particles that are within an acceptance of $|\eta| < 2.5$. The high granularity is needed in order to have unambiguous hits in the events where pile-up leads to a high charged particle multiplicity.

The pixel detector itself has three cylindrical layers in the barrel, $|\eta| < 1.7$, and three disks perpendicular to the beam axis in order to extend the acceptance to $|\eta| < 2.5$. Each layer consists of modules/sensors, and there are 1744 of

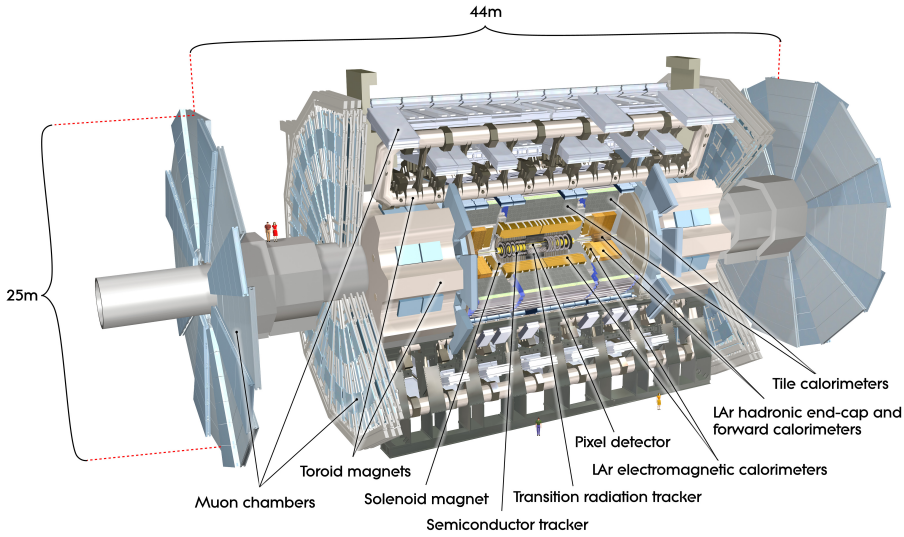

Figure 3.3: an overview of the ATLAS detector is shown.

them in total. Each module has 47232 pixels of size $50\,\mu\text{m} \times 400\,\mu\text{m}$, where the narrow side measures the ϕ-coordinate. Since the charged particles are deflected in this plane, this configuration allows for a better resolution of the transverse momentum. In total there are roughly 80.4 million read-out channels, recording for each pixel hit the time-over-threshold, which serves as a measure of the charge deposited in the material.

The working principle behind the pixel tracker is that a charged particle traversing the semiconducting material will create electron-hole pairs that then will drift in a pn-type silicon diode to small implants consisting of material with a higher doping (called n^+-type). An illustration is given in Figure 3.5. The implants are insulated from each other by a p-type coat. Every implant is connected to the read-out electronics via a small solder ball, called a 'bump bond'.

The resolution of the pixel detector is $12\,\mu\text{m}$ in the azimuthal coordinate and 60 μm along the beam axis. The first layer, which is closest to the beam pipe, is vital to finding secondary vertices from b hadron or τ decay. At the peak luminosity the pixel occupancy is expected to be of order 10^{-4}, which is low enough to reduce performance degradation due to hit ambiguities.

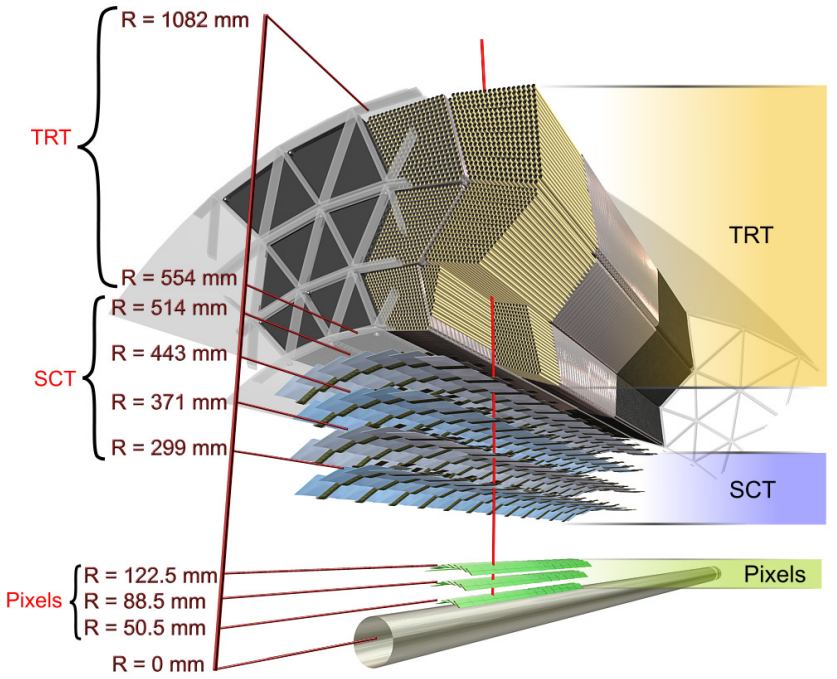

(a)

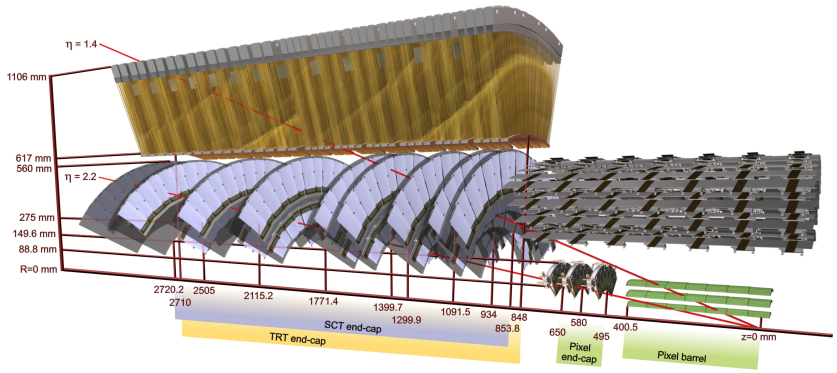

(b)

Figure 3.4: the layout of the inner detector with its three different technologies for the barrel (a) and in the end-caps (b).

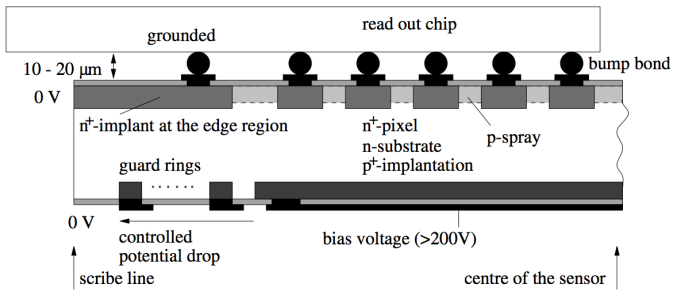

Figure 3.5: schematic view of a pixel sensor (figure taken from [36]).

Being located closest to the beam pipe, the pixel detector will endure the highest radiation dose of all subsystems. The high radiation dose will bring impurities in the semiconducting material, degrading the charge collection efficiency. Initially this can be counteracted by applying a higher bias voltage. The leakage currents are minimised by operating the pixel system at a temperature in the range of $-10°C$ to $-5°C$. However, it is expected that at LHC's peak luminosity the innermost pixel layer will have to be replaced within 3 years.

The Semi-Conductor Tracker

The semi-conductor tracker (SCT) surrounds the pixel tracker and can provide at least four space points in addition to the pixel tracker, allowing a better momentum measurement. Like the pixel detector it is a semiconductor tracker and its acceptance is limited to $|\eta| < 2.5$.

The SCT consists of modules. Each module houses 768 semi-conducting p-strips on n-type silicon that serve as the active material. In the barrel there are four cylindrical layers and in the end-caps there are nine layers arranged in disks. Each layer consists of a pair of strips. The strips are rotated in a small angle of 40 mrad between each other, making it possible to reconstruct the z-coordinate. Strips in the barrel modules have a short side of 80 μm and a length of 12 cm. Like the pixel detector, in order to obtain the best resolution in the bending plane, the long side of the strip is aligned with the beam axis. This small angle additionally helps solving hit ambiguities during track finding. Since in the end-caps the strips are aligned radially, the strips have a wedge-shaped design.

In the barrel, the spatial resolution of a strip pair is 17 μm in the bending

plane and 580 μm in the z-coordinate. Roughly the same accuracy is obtained in the end-caps, but the end-cap accuracy depends on the radius due to non-constant pitch. The resolution of the third coordinate is related to the sensor thickness, giving $300\,\mu\text{m}/\sqrt{12}$.

The Transition Radiation Tracker

The transition radiation tracker is built from small axial drift tubes, with a diameter of 4 mm. In the barrel these tubes are aligned along the beam axis, while in the endcap they are aligned radially. Each tube is filled with a gas mixture of 70% Xe, 27% CO_2 and 3% O_2 and contain a gold-plated tungsten anode wire with a diameter of 31 μm at a potential difference of 1530 V with the tube wall. Charged particles that traverse the gas will liberate electrons due to ionisation which allows tracking for any type of charged particle.

Drift circles can be reconstructed by measuring the time at which the signal reaches the wire, leading to a 130 μm resolution of the coordinate measurement in the bending plane. Although its resolution is much worse than the pixel and SCT detectors, it still plays a vital role in charge determination and reconstruction of high transverse-momentum tracks. This is due to the larger radial depth, or lever arm, which makes the bending angle more pronounced.

A track that traverses the full radial depth of the inner detector will pass through 36 tubes or straws in the barrel region. In the transition region, $0.8 < |\eta| < 1.0$, the number of straws traversed is reduced to a minimum of 22. Around $\eta \approx 0$, there is a small gap with no TRT acceptance.

Polypropylene fibers and foils are interleaved between the straws. Polypropylene has a high dielectric constant. Photons are emitted when a highly relativistic particle makes the transition between regions with a high and a low dielectric constant. This phenomenon is called transition radiation. These transition-radiation photons will, in addition to the particle itself, ionise the Xe gas atoms, yielding hits that are more likely to pass a higher threshold at the front-end electronics. The energy lost by transition radiation is proportional to the relativistic boost γ. Since electrons have a very small mass, the relativistic boost is much larger than for any other particle with the same momentum. Hence, the number of high-threshold hits can help to improve the electron identification. For electrons with an energy above 2 GeV, seven to ten high-threshold hits are typically expected.

The barrel of the TRT is built in three cylindrical layers with 32 modules each. In total there are 52544 straws arranged in a uniform axial array with an average spacing of 7 mm. The barrel module consists in two parts: one with

$z < 0$ and one with $z > 0$. The straw length is approximately 78 cm, yielding an axial straw coverage ranging between -78 cm and 78 cm with a small gap for electronics and mechanical support around $z = 0$. These tubes do not measure the position along z and so there will be hit ambiguities that can only be solved by the pattern recognition.

The end-cap geometries consist of two sets of wheels. The sets of wheels located closest to the interaction point consist of 12 wheels that are 8 mm apart. The outer sets have 8 wheels with 15 mm gaps. In total there are 122880 straws in the end-cap with a length of 37 cm.

3.2.3 The Calorimeter

There are two types of calorimeters, electromagnetic and hadronic, grouped according to their use in reconstruction. The electromagnetic calorimeter is designed for identification of photons and electrons. The hadronic calorimeters are vital to jet reconstruction and measurements of missing transverse energy. An important feature of the calorimeter system is that the particles are absorbed in the process, which ensures a clean environment for the muon system. At $\eta \approx 0$, where the material budget is smallest due to the shortest path length, the thickness of the material of the calorimeter provides 11 interaction lengths, which reduces the rate of particles punching through the calorimeter into the muon spectrometer to a very low level. Due to this important feature, very low backgrounds in muon reconstruction can be obtained.

As can be seen from Figure 3.6, five calorimeter subsystems can be discerned within ATLAS:

- the electromagnetic barrel (EMB). This is a highly granular sampling calorimeter with Liquid Argon (LAr) as the active medium and lead as the absorber. Its main goal is to identify and reconstruct electrons and photons in the range $|\eta| < 1.8$;

- the electromagnetic end-cap (EMEC, sometimes called EME). The technology is also based on lead-LAr and complements electron and photon reconstruction acceptance in the range $1.5 < |\eta| < 2.5$;

- the tile calorimeter. The tile calorimeter covers the barrel region $|\eta| < 1.7$. In this sampling calorimeter, steel is used as the absorber and scintillating tiles form the sampling material;

- the hadronic end-cap (HEC). This is a lead-LAr sampling calorimeter;

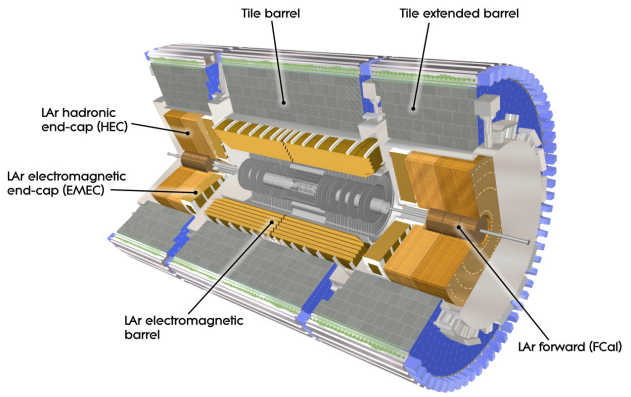

Figure 3.6: the five different calorimetric regions and their locations in ATLAS.

- the forward calorimeter (FCal). This device is also based on LAr as active material and has copper/tungsten absorber plates.

The Electromagnetic Calorimeter

The electromagnetic calorimeters are lead-LAr sampling calorimeters. A module is built from an accordion shaped absorber (see Figure 3.7) that is interleaved with kapton electrodes. The drift gap that is created this way is 2.1 mm and the potential difference is 2000 V, yielding a total drift time of 450 ns. The long drift time necessitates balanced analogue differentiation and integration steps of the signal in the front end boards in order to find a compromise between the electronics noise and pile-up noise.

The folds in the accordion structure are oriented along the ϕ-direction, thus providing a uniform coverage with no azimuthal cracks. The division of cells is obtained by etching the electrodes along η and grouping multiple electrodes along ϕ. For tracks originating from the origin of ATLAS, the etching has made it possible to make an approximately projective cell geometry.

The barrel electromagnetic calorimeter has a radius ranging from 1.5 m to 2 m and $z = -3.2$ m to $z = 3.2$ m ($|\eta| < 1.475$). Depending on η, the lead-LAr combination provides a thickness that ranges from 22 to 33 radiation lengths.

As can be seen from Figure 3.7, the readout is segmented in three radial layers, each having a distinct segmentation in η and ϕ. Except for the first

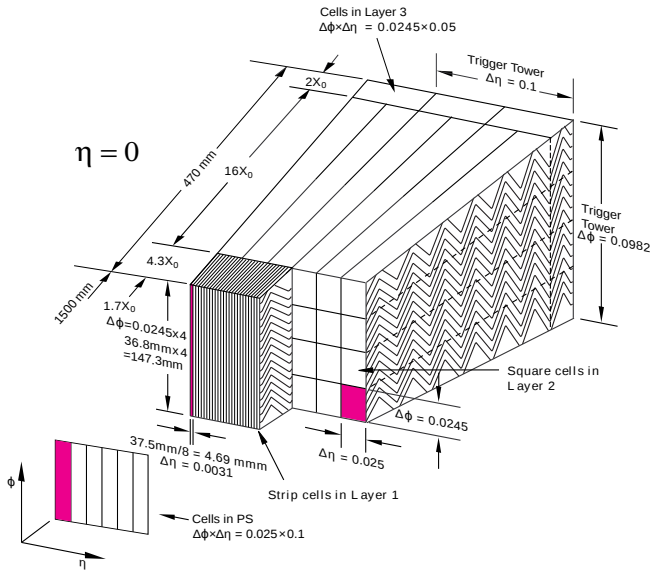

Figure 3.7: a detailed view of the segmentation of the barrel calorimeter.

layer, the end-cap devoted to precision physics, ranging from $1.475 < |\eta| < 2.5$, has the same segmentation as the barrel. In the front layer the segmentation along η is coarser in the very forward region since the copper strip has to be bigger than a few millimeter due to technical constraints.

The Tile Calorimeter

The Tile calorimeter is hadronic calorimeter located in the barrel, surrounding the electromagnetic calorimeter, and allows calorimetry up to $|\eta| < 1.7$. It consists of three parts: a central part having an acceptance for tracks with $|\eta| < 1$ and two extended parts (one for each side) covering $0.8 < |\eta| < 1.7$. Both subsystems range from $2.28\,\mathrm{m} < r < 4.25\,\mathrm{m}$. At $\eta \approx 0$ this corresponds to 7.4 interaction lengths.

The calorimeter consists of steel plates interleaved with polystyrene scintillating plates. The azimuthal coverage is maximised by staggering the tiles radially. Light produced in the scintillators will travel along wave-length shifting fibres to photo-multiplier tubes. The cell structure is obtained from grouping fibres together and the resulting η segmentation is shown in Figure 3.8. Radi-

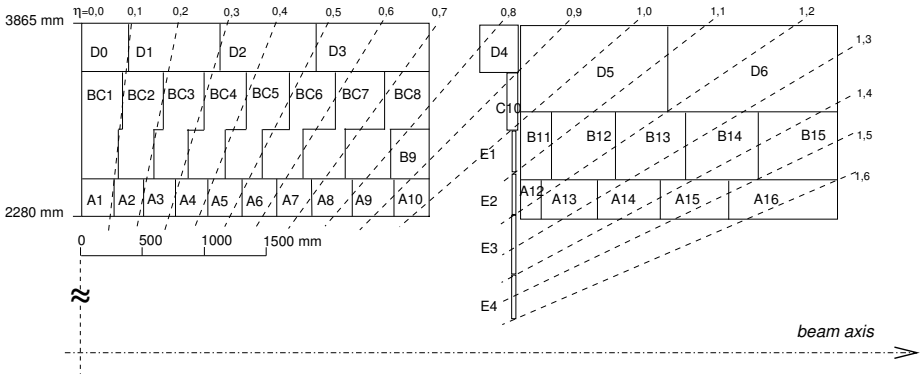

Figure 3.8: the segmentation in η and r of the Tile barrel and extension for $z > 0$.

ally it is divided into three layers. Along ϕ there are 64 modules, which yields a $\Delta\phi \approx 0.1$ cell width.

The Hadronic End-cap

The hadronic end-cap is a copper-LAr sampling calorimeter with copper as the absorber and LAr as the active material. It allows calorimetry for the pseudorapidity range $1.5 < |\eta| < 3.2$. Longitudinally the structure is divided in two wheels, consisting of 24 copper absorber plates of 25 mm in the first wheel and 16 copper absorber plates, twice as thick, in the second. The 8.5 mm wide gap between the copper plates, which are kept at ground potential, is divided into four smaller drift gaps by three electrodes at 1800 V. The advantage of splitting the gap into three smaller gaps is that the potential can be kept lower, hence reducing the risk of breakdown, while keeping the typical drift time for electrons at 430 ns. Etches in the middle electrode, which serves as the read-out electrode, make up the cell structure. For $1.5 < |\eta| < 2.5$, the cell structure is $\Delta\eta \times \Delta\phi = 0.1 \times 0.1$, while for $2.5 < |\eta| < 3.2$ it is twice as coarse in both directions.

The Forward Calorimeter

The forward calorimeter, usually abbreviated as FCAL, covers the region $3.1 < |\eta| < 4.9$. It consists of one electromagnetic and two hadronic layers providing roughly 200 radiation lengths and 10 interaction lengths. Located very close to

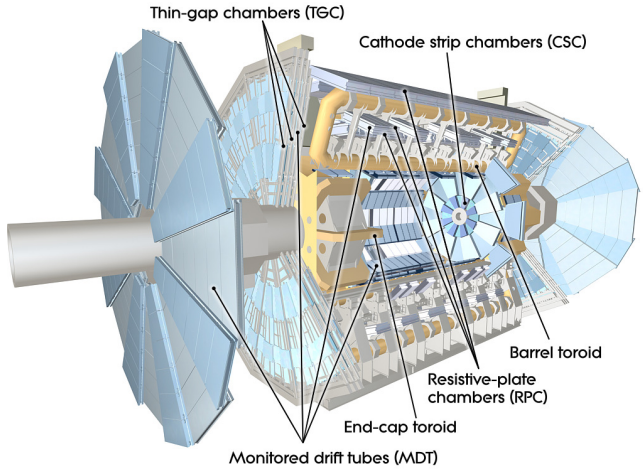

Figure 3.9: cut-away view of the muon system.

the beam pipe, the FCAL is exposed to high particle fluxes. This brings the need for smaller drift gaps in order to keep the drift time below 60 ns. In order to arrive at these small drift gaps a different geometry has been chosen than for the other LAr subsystems. The absorbers are plates of copper (in the electromagnetic layer) or tungsten (in the hadronic layer) and have regularly spaced holes through which cylindrical electrodes are fitted. These co-axial electrodes consist of copper rods surrounded by copper tubes with small spacings. This space is filled with LAr and serves as the drift region. The rods are coupled to the read-out system.

3.2.4 The Muon System

Relativistic muons with momenta below 100 GeV are minimum-ionising particles (see Chapter 5). This means that a muon will penetrate the calorimeter if its momentum is larger than 3 GeV. Since muons are the only type of particles that have this property and are involved in many interesting physics channels, a separate system has been built to identify these particles. In addition, the system is capable of redoing the tracking with a much larger lever arm than the inner detector, thereby increasing the momentum resolution for high momentum muons.

Technology	Acceptance	Usage
monitored drift tubes (MDT)	$\|\eta\| < 2.7$	Tracking
cathode strip chambers (CSC)	$2.0 < \|\eta\| < 2.7$	Tracking
resistive plate chambers (RPC)	$\|\eta\| < 1.05$	Trigger
thin gap chamber (TGC)	$1.05 < \|\eta\| < 2.4$	Trigger

Table 3.1: the different technologies in the muon spectrometer.

Figure 3.9 shows a cut-away view of the muon system. Two types of detectors can be distinguished: precision chambers, which are aimed to precisely measure the coordinate in the bending plane, and trigger chambers, which provide a coarse momentum measurement and a quick read-out for trigger purposes. Due to the higher rate in the forward region, two different technologies exist for both the precision and trigger systems, yielding a total of four different detector technologies listed in Table 3.1. The muon system is immersed in a toroidal magnetic field which provides the bending required for momentum measurements.

The magnetic field generates the bending power along the z-axis. It is generated by three toroidal magnets, one covering the region $|\eta| < 1.4$, and two covering $1.6 < |\eta| < 2.7$ on both sides. Each magnet consists of eight superconducting, air-core, coils. Multiple scattering is reduced due to the air-core design, but, on the other hand leads to a more complicated magnetic field. Depending on η, this provides a bending power, expressed by integrating the $\mathbf{B}$-field over the path the muon traverses, $\int \mathbf{B} \cdot \mathrm{d}\mathbf{l}$, of 1.5 Tm to 5.5 Tm in the barrel and 1 Tm to 7.5 Tm in the end-caps. The region $1.4 < |\eta| < 1.6$ is called the transition region of the muon spectrometer. This region has the lowest bending power and the most complicated field geometry.

A set of 1800 Hall sensors measure the magnetic field at various points in the muon system. These measurements are fed back to simulations in order to reconstruct precisely the toroid positioning and the effect of perturbation of other structures in the vicinity, such as the support structures and the calorimeter.

Precision Chambers

The goal of the precision chambers is to measure the z-coordinate with a resolution of 50 μm or less. This means that for 1 TeV muons a relative momentum resolution of 10 % can be achieved.

At least three precision chambers are hit by a muon in the range $|\eta| < 2.7$. In the range $|\eta| < 2.0$, these are all MDT chambers, but in the region $2.0 <$

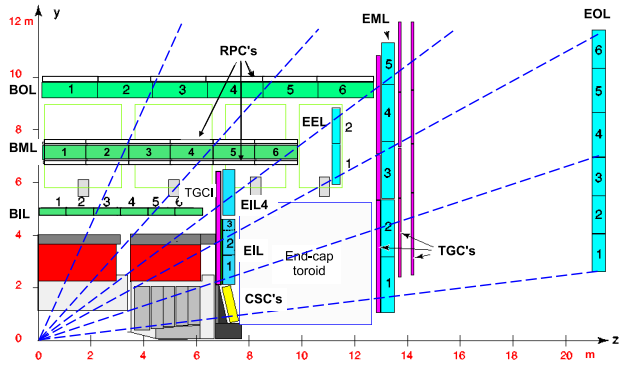

Figure 3.10: a cross-section in the yz-plane of one quarter of the muon system. In the barrel region the MDTs are drawn in green, while in the end-cap region they are drawn in blue and cyan. The CSCs are also shown in yellow.

$|\eta| < 2.7$, the muon also passes through a CSC. In Figure 3.10 the layout is shown in more detail. The chambers overlap in η and in ϕ in order to have no acceptance gaps, however for $\eta \approx 0$ there is a small gap that allows services to the inner detector and calorimeter to pass through. Along the azimuthal direction there are sixteen sectors covering the full range, except in the vicinity of the feet structure where that supports the detector.

An MDT chamber consists of 3-8 layers of aluminium drift tubes [37] of 29.970 mm radius. They are filled with a mixture of Ar/CO_2 (93/7) gas at approximately 3 bar which is continuously refreshed. In the middle, a 50 μm tungsten-rhenium wire collects the charge liberated by the muon and is kept at a potential of 3080 V. In the barrel, the long sides of the tubes are oriented along the ϕ-direction, while in the end-caps they are oriented along the r-direction.

Drift circles are reconstructed by recording the arrival time of the first pulse via the space-time ($r-t$) drift relation. In Ar/CO_2 the drift relation is non-linear and dependent on pressure and temperature. These parameters are monitored very accurately giving a single-tube resolution of 80 μm.

Muons entering the tube immediately ionise the gas, leaving a trail extending from one side of the tube to the other. The electrons freed near the boundary of the tube need to travel the largest distance to reach the central wire. Since there are nearly always electrons close to boundary this means that the maximal drift

time of 700 ns is almost always needed in order to restore the tube to a relaxed state. During this time the tube is not able to register a new hit, making the MDT a slow system with respect to the bunch-crossing rate.

Very important for the sagitta measurement is the relative alignment of the chambers. Measuring the sagitta very well is important, since the momentum reconstruction uses it directly. Using an optical alignment system and exploiting the chamber overlaps to perform calibration of straight muon tracks recorded in runs without magnetic field, the sagitta resolution eventually is meant to reach its design goal of $\sigma_S = 45\,\mu\text{m} = 30\,\mu\text{m}\,(\text{alignment}) \oplus 35\,\mu\text{m}\,(r-t)$.

The CSC chambers measure both coordinates by looking at the induced charge on strips which are segmented with a pitch of 5.6 mm along the bending coordinate. In the perpendicular coordinate the strip pitch is more coarse. The coordinate is determined by relative charge differences on adjacent strips. This makes the CSC largely independent of the conditions of the Ar/CO_2 gas. The 7 ns drift time is small enough to determine the bunch crossing. The resolution obtained is 40 μm in the azimuthal coordinate and 5 mm in the non-bending r-coordinate.

Trigger Chambers

The muon trigger chambers in ATLAS are fast detectors that are able to tag the bunch crossing in which a muon is created. They can also make a rough momentum estimate to allow for different trigger levels. In addition, they provide a measurement of the second coordinate which can help to solve ambiguities in MDT pattern recognition.

In Figure 3.10 the layout of the trigger chambers is shown. In the barrel, RPCs are used and are arranged in three concentric layers. Two layers are located at the bottom and the top of the middle MDT chamber, while the last layer is located at the top of the last MDT layer in the even ϕ-sectors and on the bottom in the odd ϕ-sectors.

Four layers of TGCs are present in each end-cap. The layout is shown in Figure 3.10. At least two chambers are stacked behind each other in each layer. The redundancy obtained can then be used to veto background hits in a single chamber.

Triggering is achieved by detecting coincident hits within a road. First a hit in the the so called pivot plane is required. In the barrel this is the middle RPC layer, while for the endcap this is the last TGC layer. For low-p_T tracks another hit in a window in the layer close to the pivot plane is required. For high-p_T tracks, the lever arm is extended by looking for coincident hits in a window in

the layer with a larger separation. Low-p_{T} muons will bend more heavily in the magnetic field and miss this window. In case tracks are penetrating the barrel this is the outer RPC layer while for forward tracks this is the inner TGC layer. The coincidence is required in both coordinates in order to make the muon trigger robust to potentially high background rate caused by the abundance of low-energy neutrons and photons (cavern background).

The RPC is built from gaseous parallel electrode-plate detectors. One such detector consists of two resistive plates, which are separated by 2 mm. An electric field of 4.9 kV is applied. When a charged particle traverses the plates, a short signal due to avalanche formation in the gas, consisting mainly ($> 94\%$) of $C_2H_2F_4$, is induced on the metallic strips, which are segmented along η on one side and along ϕ on the other. The time resolution obtained is slightly more than 5 ns, which is small enough to allow tagging of the bunch-crossing. One chamber is formed by stacking two layers on top of each other with a small space in between. This means that one chamber provides two measurements, or four hits (two for each coordinate).

A TGC consists of at least two layers of multi-wire proportional chambers. One such chamber consists of many wires, spaced at 1.8 mm with respect to each other. The wires are kept at a potential of 2900 V with respect to the grounded graphite layer. The gap between the graphite layer and the wires is 1.4 mm and it is filled with a gas mixture of CO_2 and n-pentane. Located behind the graphite layers and oriented perpendicular to the wires, are the pick-up strips. The signal is obtained by avalanche formation in the strong electric field close to the wires. Liberated electrons will only need to drift to the closest wire and the small wire-to-wire distance thereby helps to ensure a time resolution good enough to tag the bunch-crossing.

The wires are arranged along the azimuthal direction in order to measure the bending direction and are grouped together in groups of 6 to 31, depending on η. This corresponds to a width in the r-direction between 10.8 mm and 55.8 mm. The strips, oriented radially, provide a measurement of the ϕ-coordinate and the granularity is $2 - 3$ mrad.

3.2.5 Trigger

It is impossible to stream the data of the ATLAS detector for every bunch-crossing provided by the LHC. The trigger systems in ATLAS are designed to maximally exploit the high luminosity by only selecting events that are candidates for interesting physics. An event is then only written to tape when there are for instance high p_{T} muons, jets, photons, electrons, τ leptons, large missing

transverse energy or sum of transverse energy.

Three sequential trigger levels aim to reduce the rate of data acquisition below 200 Hz.

The first level trigger, L1, runs on hardware electronics installed close to the subdetectors in order to cope with the high bunch-crossing rate. The Level 1 trigger reduces the rate to 75 kHz and a decision has to be reached in 2.5 μs. There are L1 triggers for the calorimeter and the muon system, but not for the inner detector. At this stage, when an event fulfils certain criteria, the data is streamed from the detector and put in buffers.

The Level 1 algorithms identify regions of interest (RoIs). In the second level, reconstruction is run on the data from these regions of interest at full granularity. This trigger level reaches a decision in 40 ms and reduces the rate to 3.5 kHz.

When the Level 2 trigger does not veto an event, parts of the reconstruction based on the offline software is ran on the full event data. This third and last trigger level, which is called the Event Filter (EF), has to provide a decision within four seconds, and is completely run on a 'farm' of approximately 1800 computing nodes. The final event rate will stay below 200 Hz, keeping the data acquisition rate below 300 Mb/s of raw data.

There are several trigger types: the minimum-bias trigger fires whenever there is activity in the forward region of the detector, the muon trigger fires whenever a high-p_{T} muon is likely to be produced, the electron trigger fires whenever a signal compatible to an electron is detected in the electromagnetic calorimeter and the missing transverse energy trigger fires whenever a substantial amount of missing E_{T} is likely. Depending on the precise configuration of the data acquisition, the event is only written to tape if it passes the L1, L2, or EF levels. Depending on the luminosity, the accept rates of the triggers can be scaled down by a certain factor, called prescale. A prescale of 100 means that only one in 100 events passing the trigger is accepted.

Only the muon trigger is used for the analyses in this thesis. Coincident hits in subsequent trigger chambers of the RPC and TGC are required. The roads along which these coincidences are sought become more narrow with increasing transverse momentum threshold. If coincident hits are found, the muon chambers along the road are marked as the RoI. In the level two algorithm, the very crude momentum estimate from the level one threshold is refined through a local fit, using only the data of the RoI. This provides the necessary reduction for the event filter. Here, muon tracks are fitted and these tracks can even be matched to inner detector tracks using similar methodology as in the ordinary muon reconstruction (see Chapter 4).

3.2.6 Detector Simulation

The detector response of particles produced by the event generation, as described in Section 2.2, is essential for the understanding of the data that is collected by ATLAS. It used for the estimation of the number of background events that survive event selection for a specific process. In addition, many of the reconstruction algorithms described in the next chapter could not have been commissioned without this tool.

The detector simulation propagates the final-state particles that are produced in the event generation step through a virtual representation of the ATLAS detector geometry. The `GEANT4` software package [38] is used for modelling all the interactions of the particles with the detector material. This package is a huge library containing models for particle interactions when they traverse a certain material (e.g. showering in the calorimeters), propagate through magnetic fields, etc. Since the begin of the `GEANT4` project, the physics models in the package are continuously refined using the latest measurements. The detector response is modelled by simulating the charge collection (or photon collection) at the sensitive elements. The signals are then digitised. In this step electronics noise is added and an output file is created that mimics the output of the real ATLAS detector in operation.

The `GEANT4` modelling, called full simulation, is a very CPU-intensive task. For this reason, also fast simulations have been implemented. The `ATLFAST` library [39] takes the particles from the event generation and converts them directly to reconstructed objects. In order to have a decent representation of the full simulation, the measured quantities (such as energies and momenta) are smeared by the known resolutions. The `ATLFAST` II library offers a hybrid method. Here the calorimeter response is modelled by approximate models and full simulation is run for all other subsystems. All simulated samples that have been used for the analyses in this thesis were constructed using full simulation.

4 Object Identification

The raw output of the detector consists of hit and timing information and needs to be processed in order to study the physics of the events. In this section, the algorithms for particle identification, jet reconstruction and the calculation of missing transverse energy will be described. All reconstruction algorithms are implemented in the `Athena` software framework [40].

Tracking, muon identification, jet reconstruction and missing transverse energy determination are discussed in Sections 4.1, 4.2, 4.3, 4.4 respectively. These sections start with an outline of the reconstruction algorithms and are followed by performance results on the data taken in 2010. Electrons, photons, taus and b-taggers are not explicitly used in this thesis and therefore are described in less detail in Section 4.5. This chapter ends with an analysis of production sources of low-momentum muons in early data in Section 4.6.

4.1 Tracking

A track, or trajectory, is a curve in three dimensions usually given by five parameters: three momentum components and two position coordinates. In the inner detector charged particles follow approximately helical trajectories due to the homogenous magnetic field, while in the muon spectrometer tracks are more complicated due to the inhomogenous magnetic field.

In most physics analysis cases, the track parameters at the particle's produc-

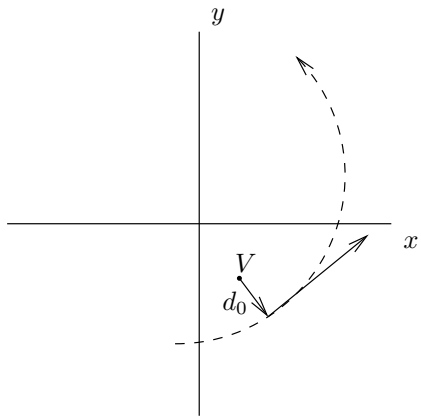

Figure 4.1: the perigee representation of a track with respect to a vertex in the xy-plane. The impact parameter, d_0, is measured with respect to the primary vertex V. The longitudinal impact parameter z_0 is the length of the vector pointing from the primary vertex to the distance of closest approach projected on the z-axis.

tion point are of interest. The most commonly used representation is therefore the representation of the track parameters at the point closest to the production vertex (see Figure 4.1):

$$\mathbf{P} = \begin{pmatrix} q/p \\ \theta \\ \phi \\ d_0 \\ z_0 \end{pmatrix}, \tag{4.1}$$

where q/p is the charge of the particle divided by its momentum, and θ and ϕ indicate the polar angle and the azimuthal angle of the momentum vector. The position coordinate d_0 is the distance of closest approach of the track to the vertex in the transverse plane. The position in z where this transverse plane intersects the beam line is called z_0.

Track reconstruction in the inner detector starts with a preprocessing stage, interpreting the hits in the raw detector data. In the pixel detector, 3D space points are found directly by converting the 2D local coordinate on the module to a global coordinate. In the SCT, 3D space points are formed by combining

the two hits on both sides of a strip pair. The TRT data preprocessing converts the measured timing information into 2D drift circles.

After having converted the raw detector output into hit positions, the track finding stage starts searching for track candidates. This search starts by generating track seeds from the three pixel layers and the first layer in the SCT. At the seed-searching stage, the trajectories are approximated by helices.

Every track seed is extrapolated downstream in the SCT, looking for additional hits. The extrapolation starts from the outermost surface of the pixel detector and terminates when it traverses a sensitive detector surface. There are now three cases: a hit is found; a hit is found, but has a negative effect on the fit quality, called an outlier; no hit was found, which is called a hole. After this procedure, the number of track candidates are reduced by a factor of ten by imposing quality cuts on the number of holes and outliers.

At this stage many track candidates will be sharing the same hits. A scoring procedure ranks all track candidates in order to resolve these ambiguities. For example, holes are penalised, while overlapping modules improve the score.

In the next stage the track is more carefully fitted by two methods: the Kalman filter [41] and the global-χ^2 fitter [42].

The global-χ^2 fitter extrapolates the track to every detector element that has a hit and calculates the χ^2 from the residuals divided by the total uncertainty from the measurements and extrapolation. The extrapolation uses detailed magnetic field maps and geometry of the detector in order to account for energy loss in the material.

Kalman filters are widely used in many fields for obtaining the state vector in the presence of process noise and measurement uncertainty of a linear dynamical system. For the purpose of track fitting, the state vector represents the track parameters, the process noise represents multiple scattering and the measurement uncertainty represents the finite resolution of the detector hardware. Due to the bending in the magnetic field, an approximation needs to be made by linearising (Taylor expanding) the system equations.

After a local χ^2 fit, an initial guess of the track parameters can be made. This is used to predict the state vector on a detector surface downstream. By comparing the prediction with the measurement on that surface, taking into account the limited resolution and multiple scattering, the state vectors on the surfaces upstream are updated. The next prediction can be made using the updated state vectors. The process continues until all hits are assigned. The track parameters are then estimated at every detector surface.

In the final stage it is attempted to extend the track with TRT hits. This increases the momentum resolution especially for high momentum tracks. Al-

though TRT outliers are not included in the fit, they are still associated to the tracks and can be used for quality cuts in the physics analysis stage.

In addition to the procedure described above which works inside-out, there is a complementary track seed approach starting outside-in from the TRT. The track seeds in the TRT are found by applying a Hough transform [43, 44] and the procedure followed is similar to the one described above. Outside-in tracking is very important for reconstruction of photon conversions and decays of long-lived particles. The inside-out tracking will not be able to find correct track seeds for the decay products if the conversion or decay takes place beyond the SCT.

The adaptive vertex-finding algorithm [45] is run in the last step. The first vertex seed is formed from the maximum of the z-position distribution generated from all tracks extrapolated to the beam spot. The vertex fit [46] is then carried out as a χ^2 fit, where the χ^2 contribution for each track is calculated from distance of closest approach to the vertex and the uncertainty on the distance. The usual definition of a χ^2 is modified by applying lower weights to large contributions:

$$\begin{aligned} \chi^2 &= \sum_{\text{tracks},i} w(\chi_i^2) \cdot \chi_i^2, \\ w(\chi_i^2) &= \frac{\exp(-\chi_i^2/T)}{\exp(-\chi_i^2/T) + \exp(-\chi_c^2/T)}. \end{aligned} \tag{4.2}$$

The quantity T, called temperature, is decreased after each iteration. For very small temperatures, the weights behave like step functions $\theta(-\chi_i + \chi_c)$. In this view, the quantity χ_c operates as a threshold. Decreasing the temperature then 'freezes' the system, and effectively removes incompatible tracks from the fit. All tracks not within 7σ are incompatible with the vertex and used to seed new vertices.

The primary vertex is defined to have the highest sum of p_{T}^2 of its associated tracks.

4.1.1 Performance

Alignment

The inner detector modules are not exactly located on their nominal positions after installation. These misalignments increase the uncertainty of the position assigned to a hit, which directly has an impact on the momentum resolution. However, these imperfections can be corrected for. Here the method used for alignment is briefly described. More details can be found in [47].

The alignment is done on a sample of isolated high-p_{T} tracks from collisions and cosmic muons. High-p_{T} tracks do not suffer as much from multiple scattering as low-p_{T} tracks and isolated tracks do not suffer from possibly ambiguous hit associations. For every hit, the residual $\mathbf{r}$ is calculated from the distance of the extrapolated track to the hit. The χ^2 is built from the covariance matrix, V, which contains the errors induced by the extrapolation and the intrinsic resolutions of each sensor element, in the following way:

$$\chi^2 \quad = \quad \mathbf{r}^{\mathrm{T}} V^{-1} \mathbf{r}. \tag{4.3}$$

The χ^2 is minimised with respect to the alignment parameters. This is done by taking the first derivatives of the residuals with respect to the alignment parameters, yielding a matrix equation that can be solved for the updated alignment parameters. Since only the first order derivatives are considered several iterations are needed in order to find convergence. After every iteration the track is refitted using the updated hits.

The alignment proceeds in steps. First the relative alignment between the pixel, SCT and TRT sub-detectors is done. This is then followed by a more detailed alignment. In this stage the positions of the individual TRT straws and pixel and SCT modules are allowed to float in the fit minimising the residuals. Parameterised module distortions are also taken into account in the final step. In the first step there are 41 degrees of freedom, whereas for the last step there are 722104 degrees of freedom.

In Figure 4.2, the residuals in the azimuthal coordinate, called x, before and after the alignment are compared. The tracks are selected to have $p_{\mathrm{T}} > 15\,\mathrm{GeV}$ and were obtained from jet-triggered data. The *Autumn 2010 Alignment* is used for the data of Chapter 6 in this thesis, while the *Spring 2010 Alignment* is used for the analysis in Section 4.6. The widths of the residual distributions shown from the Autumn Alignment are slightly bigger than the ones obtained from a simulated sample with ideal alignment. The difference is $1\,\mu$m for the SCT and pixel. The width of the TRT end-cap distribution deviates $14\,\mu$m from the ideal case.

4.2 Muon Reconstruction

Muon reconstruction is done in multiple ways in the ATLAS reconstruction software. Muons can be reconstructed in the muon spectrometer only; these muons are called *standalone muons*. Standalone muons can also be associated to an inner detector track, yielding *combined muons*. In addition, the muon

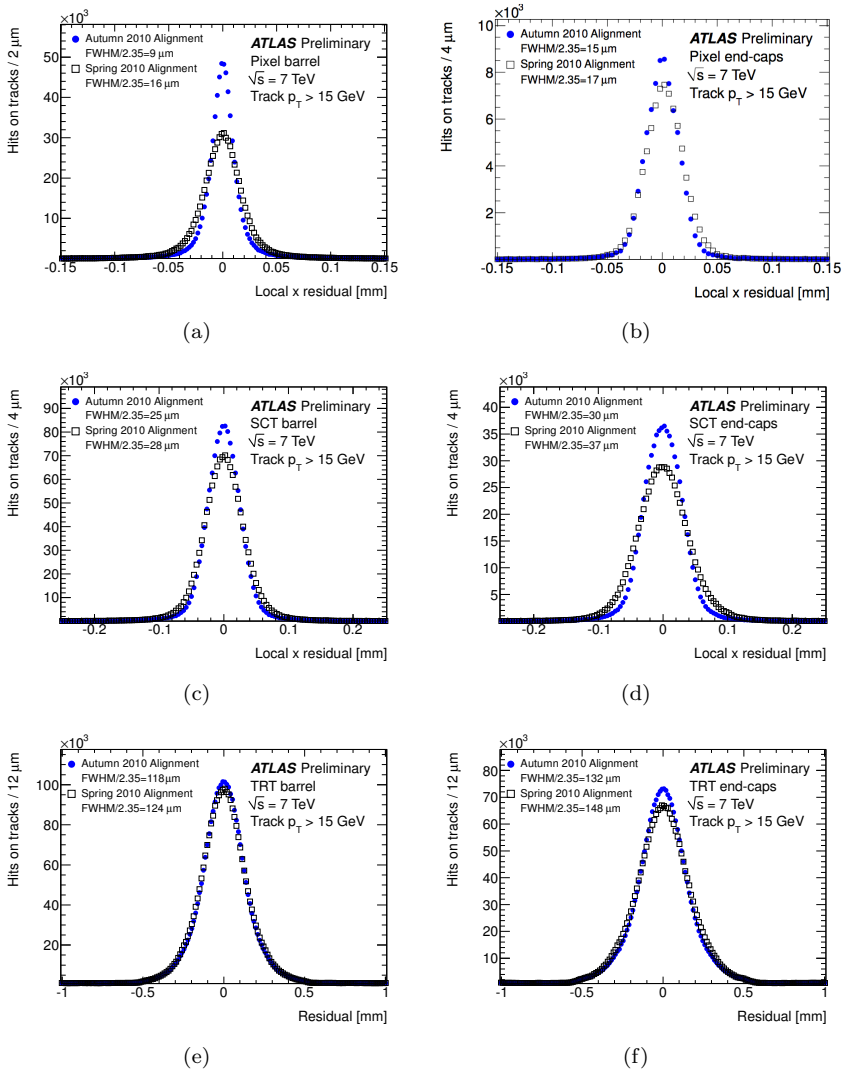

Figure 4.2: Residual distributions before and after alignment of the coordinate in the bending plane. The standard deviation is also indicated in each plot (figures taken from [47]).

spectrometer can also be used as a device for particle identification only by matching an inner detector track to a straight line segment reconstructed in one of the precision chambers. Such muons are called *segment-tagged muons*. Finally there is another method that uses the minimum-ionising property of the muon to identify muons in the calorimeter. That method is described in Chapter 5.

In the ATLAS software there are two separate algorithm chains (not including the muons identified in the calorimeter) for muon reconstruction. Although both use the same data, they have a slightly different approach. Whenever chain 1, or `Staco` (indicating *statistical combination*), and chain 2, or `Muid`, are different in approach, it will be mentioned. Both chains, however, have the same global structure.

Standalone muon reconstruction starts by converting raw detector data from the MDTs to drift circles and the CSCs and trigger chambers into clusters. Pattern recognition is run in order to create straight-line segments in the precision chambers, either from drift circles in MDT or clusters in the CSC. Here chain 1 and chain 2 are different.

- Chain 1 starts by first defining a region of activity of size 0.4×0.4 in $\eta \times \phi$, centred around a trigger hit. From here, straight lines that are loosely pointing towards the interaction point are connected between the drift circles. In order to solve ambiguities and to reduce fakes, segments crossing a tube with no hit are penalised with respect to other candidates.

- Segment finding in chain 2 is done by two modes of pattern recognition run in parallel: a global Hough transform in η, ϕ-space of MDT, and trigger hits and segment construction seeded by inner-detector tracks that are extrapolated to the muon spectrometer. Ambiguities are resolved by keeping only the segments that have most hits. If segment candidates have the same number of hits, the segment having the lowest χ^2 is kept.

If there is a segment in the outer or middle chamber, extrapolation is run outside-in to associate segments in chambers upstream. If a match was found, the sagitta is calculated and is used for the initial momentum estimate. This is followed by a full fit using detailed magnetic field maps.

After the fit, the track found in the muon spectrometer is back-extrapolated to the inner detector. The energy loss in the calorimeters is determined by the well-known parameterisation for a minimum ionising particle [4]. The distribution of energy loss per unit path-length in the traversed material, $\mathrm{d}E/\mathrm{d}x$, is described by a Landau distribution, which has a long tail for large $\mathrm{d}E/\mathrm{d}x$.

For isolated muons the parameterised energy loss is replaced by the measured energy loss in the calorimeters if the measured energy loss exceeds the most probable value of the parameterisation.

If the extrapolation to the perigee succeeds, the standalone muon reconstruction is complete. Standalone muons can be reconstructed in the region $|\eta| < 2.7$, which is the acceptance of the precision chambers. Note that this is larger than the trigger acceptance, and therefore they are mostly used in physics analyses with multiple muons in the final state or analyses which do not require a muon trigger.

The muon spectrometer has a much larger lever arm than the inner detector and therefore is able to determine the muon's momentum with better accuracy if the transverse momentum is larger than 30 GeV. If its p_{T} is lower than that, the uncertainty from multiple scattering in the calorimeter dominates the resolution. In the latter region the inner detector has a better performance. Combined muons are formed by matching an inner detector track to a muon spectrometer track. Other than the improvements to momentum resolution it has the advantage of being less susceptible to fake muons induced from, e.g., punch-through. Reconstruction of combined muons is done differently in chain 1 and chain 2.

- Chain 1 makes a statistical combination of the track parameters fitted at the perigee for the muon spectrometer, $\mathbf{P}_{\mathrm{MS}}$, and the inner detector, $\mathbf{P}_{\mathrm{ID}}$, weighted with the covariance matrix:

$$\chi^2_{\mathrm{match}} = (\mathbf{P}_{\mathrm{MS}} - \mathbf{P}_{\mathrm{ID}})^T \cdot W^{-1}_{\mathrm{comb}} \cdot (\mathbf{P}_{\mathrm{MS}} - \mathbf{P}_{\mathrm{ID}}), \tag{4.4}$$

  where the combined covariance matrix W_{comb} is constructed from the covariance matrices found in the ID and MS track fits, W_{ID} and W_{MS}, through addition:

$$W_{\mathrm{comb}} = W_{\mathrm{ID}} + W_{\mathrm{MS}}. \tag{4.5}$$

  The inner detector track that has the lowest χ^2_{match} is combined with the muon spectrometer track and the new momentum is found by minimising the global χ^2, which is a sum of χ^2_{match} and the χ^2 of the inner detector and the muon spectrometer fits.

- Chain 2 first selects inner detector track candidates that could match with the muon spectrometer track. After this procedure, the hits of the inner detector and muon spectrometer are combined and a complete refit of the track is done. If the fit converges, the track combination that has the lowest χ^2 is kept in case there are ambiguities.

Segment-tagged muons extrapolate the inner-detector track through the calorimeter to the precision chambers of the muon spectrometer. If this extrapolation is very close to a reconstructed segment, a muon candidate is formed.

The great benefit from segment tagging is that it is close to 100% efficient in the region $0.05 < |\eta| < 2.5$ and that it is possible to tag low-momentum muons that are bent back into the detector before reaching the second precision station. A tough problem in segment tagging is controlling the background, or fake rate, originating from punch-through of hadronic particles into the muon system. These backgrounds are suppressed by imposing quality cuts on the segment match and track quality.

In the ATLAS collaboration, the combined muons are mostly favoured in physics analyses, since they are robust against backgrounds such as punch-through and have the best momentum resolution over the full range. However, stand-alone, segment-tagged calorimeter muons are sometimes used in physics analyses that are studying processes with multiple muons. Since the event selection efficiency is the muon-reconstruction efficiency to the power of the number of muons, a slight increase in reconstruction efficiency can have a large effect on the event selection efficiency

4.2.1 Performance

Reconstruction Efficiency

The reconstruction efficiency is determined using the *tag-and-probe* method. The procedure outlined here is described in more detail in [48]. The tag-and-probe method relies on the decay of a boson into a state with two muons. In this analysis the Z is used. First, a muon is selected that satisfies very tight criteria in order to have a low rate of background muons; such a muon is called the tag muon. Then, in the same event, a track, called probe, is sought for which the charge is opposite to charge of the tag muon. If the invariant mass of this tag-and-probe pair is close to the well-known mass of the Z boson and is separated by $\Delta\phi > 2.0$, the probe track can be assumed to be a muon. This assumption is valid since Monte Carlo studies show that after these criteria very little background is present. This means that the efficiency, ϵ, can be calculated by

$$\epsilon = \frac{N_{\text{matched probes}}}{N_{\text{tag-and-probe pairs}}}, \tag{4.6}$$

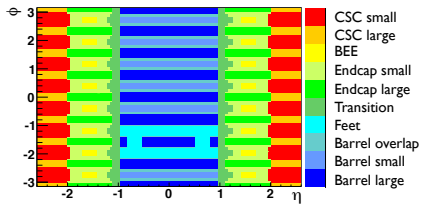

Figure 4.3: the subdivision of regions in the muon system with the same structure (figure taken from [48]).

where the number of matched probes is established by counting the tracks that can be matched to a reconstructed muon.

Only tracks with $p_{\mathrm{T}} > 20\,\mathrm{GeV}$ are considered and all tracks are subjected to stringent track selection, requiring at least one hit in the pixel detector and at least six hits in the SCT. Furthermore, a TRT extension is required if $|\eta_\mu| < 1.9$. The probe track has to be associated with the same vertex as the track of the tag muon and both tracks are required to be isolated[1]. Finally, a single-muon trigger is required. That can bias the probe if the probe actually fires the trigger, while the tag does not. In order to remove this bias, the tag muon should be associated with a trigger region in η, ϕ that matches the muon-trigger threshold.

As described in Section 3.2.4, the muon system is not uniform over its full acceptance. This has an effect on the efficiency. The muon system has therefore been divided in regions that have the same type of chambers as shown in Figure 4.3. For each such region the efficiency is determined. In Figure 4.4 the results for the combined muons for both chains are shown.

Momentum Reconstruction

The momentum resolution and momentum scale for muons are also obtained by studying $Z \to \mu^+\mu^-$ events, which are selected in the same way as described in the previous paragraph. The Z mass peak can be reconstructed from the invariant mass in data and Monte Carlo. The Monte Carlo distribution of the invariant mass is convoluted with a Gaussian with mean δ, the deviation of the momentum scale from unity, and width $\sigma = \sqrt{\sigma^2_{\mathrm{data}} - \sigma^2_{\mathrm{sim}}}$, the quadratic difference in momentum resolution between data and simulation.

The momentum resolution as function of the momentum, $\sigma(p)$, for the inner

[1] The concept of isolation will be discussed more thoroughly in Section 5.1.1.

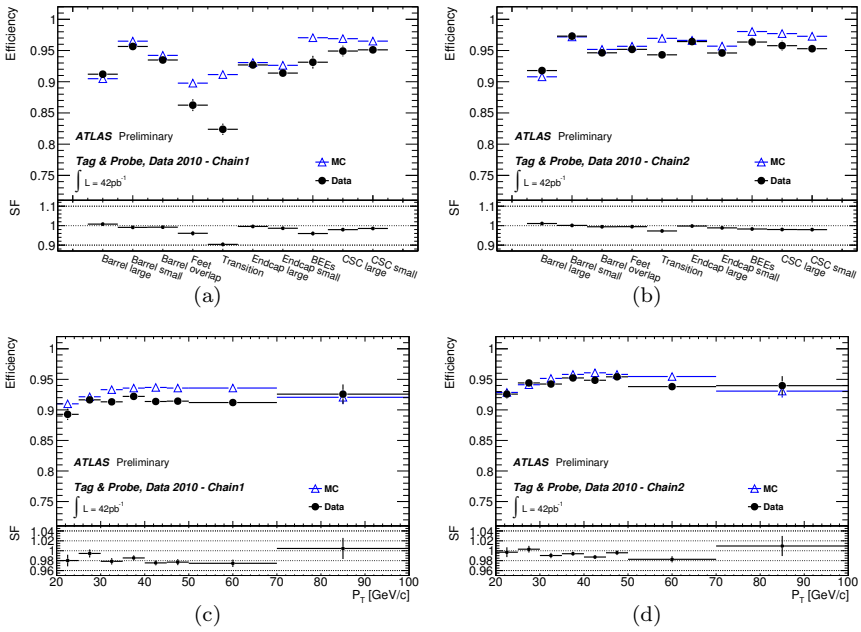

Figure 4.4: efficiency results determined using the tag-and-probe method for the two chains. The top plots show the results for the different regions shown in Figure 4.3. The bottom plots show the results integrated over the full detector acceptance as a function of the transverse momentum. The ratio, denoted SF (Scale Factor), between data and Monte Carlo is also shown in every plot (figures taken from [48]).

detector is parameterised as function of p_{T} as:

$$\frac{\sigma(p)}{p} = p_1^{\mathrm{ID}} \oplus p_2^{\mathrm{ID}} p_{\mathrm{T}}, \tag{4.7}$$

where the constant term p_1^{ID} is related to multiple scattering and the term proportional to p_2^{ID} is related to the intrinsic sub-detector resolutions and alignment. For forward muons with $|\eta| > 1.9$, it depends on the polar angle of the muon track, θ:

$$\frac{\sigma(p)}{p} = p_1^{\mathrm{ID}} \oplus p_2^{\mathrm{ID}} p_{\mathrm{T}} \frac{1}{\tan^2\theta}. \tag{4.8}$$

In the muon spectrometer an additional term $\frac{p_0^{\mathrm{MS}}}{p_{\mathrm{T}}}$ is added to account for the uncertainty of the energy loss in the calorimeters:

$$\frac{\sigma(p)}{p} = \frac{p_0^{\mathrm{MS}}}{p_{\mathrm{T}}} \oplus p_1^{\mathrm{MS}} \oplus p_2^{\mathrm{MS}} p_{\mathrm{T}}. \tag{4.9}$$

The parameters p_0, p_1 and p_2 are determined from a combined fit of the Z lineshape in four regions:

- Barrel region: $|\eta| < 1.05$,
- Transition region: $1.05 < |\eta| < 1.7$,
- End-cap region: $1.7 < |\eta| < 2.0$,
- CSC/no-TRT region: $2.0 < |\eta| < 2.5$.

The results are shown in Figure 4.5. Note that the simulation performs much better than the data. This is expected since the positions of the detector elements are precisely known in the simulation. More details about the fitting procedure can be found in [49].

4.3 Jet Reconstruction

Jet reconstruction is initiated by the formation of jet constituents, which are obtained from grouping calorimeter cells together. In the ATLAS software there are two types of constituents: *calorimetric towers* and *topological clusters*, or *topoclusters*. Both are represented by momentum four-vectors, where the energy

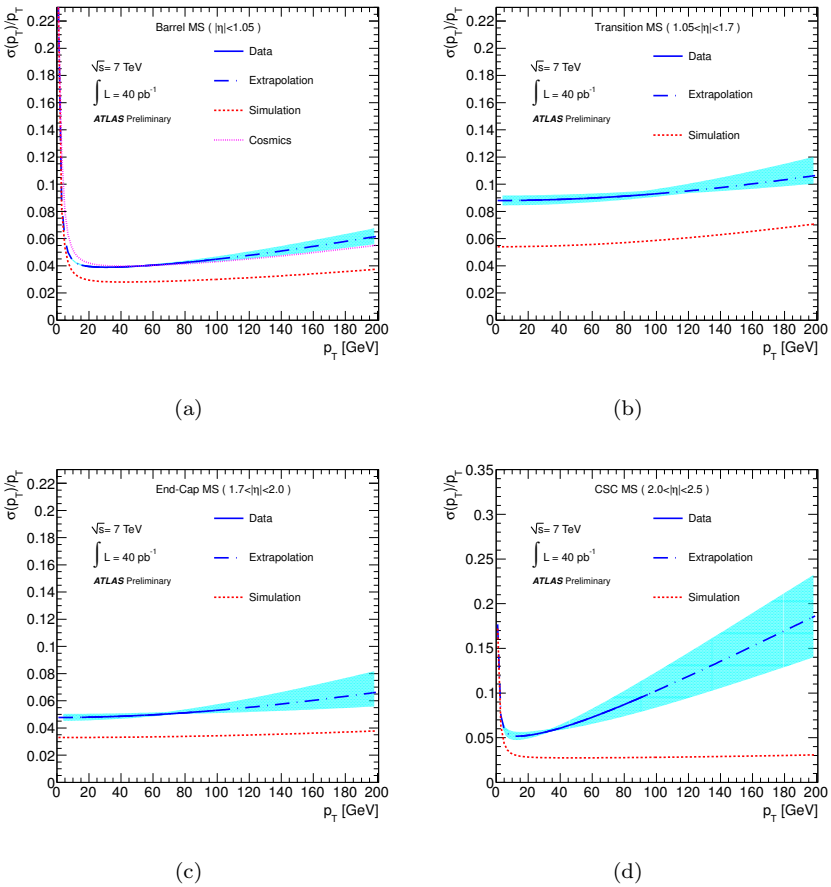

Figure 4.5: the momentum resolution for muons for the barrel region (a), transition region (b), end-cap region (c) and the CSC/no-TRT region (d) (figures taken from [49]).

is obtained from the sum of the measured energies in the calorimeter cells that are grouped together and the direction is calculated from the addition of the vectors pointing to the centres of the cells, weighted by the cell energy.

Calorimetric towers are defined by groups of cells that are contained in a projective grid of 0.1×0.1 in $\eta \times \phi$. When a cell is associated to more than one tower, the fraction of energy added to each tower is proportional to the overlapping surface. This happens especially when the calorimetric cell structure is not projective, e.g. in the tile calorimeter. The measured energy can be negative due to calorimetric noise suppression. Calorimetric towers have a very basic noise subtraction by merging towers with a negative net energy with adjacent towers until the energy becomes positive.

The construction of topological clusters starts with seed cells for which the measured energy in the cell exceeds four times the RMS of the noise for that cell[2]. The initial cluster is built around this seed by adding all the neighbouring cells. If one of the neighbours has a cell with a measured energy that exceeds twice the RMS of the noise, it will form a secondary seed and the neighbouring cells of the secondary seed are added. The procedure stops when no secondary seeds are found while expanding the cluster around its secondary seeds. When a cluster has local maxima, it will be split up in multiple clusters. Noise reduction is provided by the signal over noise requirements of the seeds.

Jets are formed from the reconstructed constituents. There are two classes of algorithms used in ATLAS: the *cone algorithm* and the *anti-k_{T} algorithm*. Since the cone jets are not used in this thesis only the *anti-k_{T} algorihtm* will be described.

The generalised-k_{T}-algorithm[3] has a modified distance measure, d_{ij}, between constituents i and j:

$$\begin{aligned} d_{ij} &= \min\left(p_{\mathrm{T},i}^{2p}, p_{\mathrm{T},j}^{2p}\right)\frac{\Delta R_{ij}^2}{R^2}, \\ d_i &= p_{\mathrm{T},i}^{2p}. \end{aligned} \tag{4.10}$$

Here R is the distance parameter and d_i is a measure of the distance with respect to the beam. When the parameter $p = 1$ the k_{T} or Cambride/Aachen algorithm is obtained, while for $p = -1$ it is called the anti-k_{T}-algorithm. The clustering starts by looking at the smallest of all obtained values above:

[2]The RMS of a cell is determined in calibration runs when no collisions are delivered by the LHC.

[3]The term k_{T} indicates the transverse momentum and has been replaced here by p_{T} for consistency.

- if the smallest value is a distance d_{ij}, both constituents are merged into a new one by adding the four-momenta. After removing constituent i and j and replacing it by the merged constituent all the values are recalculated;

- if the smallest value is d_i, the (possibly merged) constituent is identified as a jet and is removed.

Eventually all constituents are merged into jets or have become jets and the algorithm stops.

The anti-k_{T} algorithm deals very well with soft particles that are radiated in the hadron shower. The distance d_{ij} between two soft constituents is weighted by the inverse of the transverse momentum squared and is much larger than the distance between a hard and a soft constituent, due to the min-function. Most of the soft particles emitted in the parton shower are therefore associated to the nearest hard constituent instead of forming a jet on their own, even when they are clustered together.

4.3.1 Jet Calibration

The ATLAS calorimeters are non-compensating, which means that the signal response for hadronic showers is lower than that for electromagnetic (EM) showers. In fact, only a part of the hadronic shower is measured and the EM energy estimate for hadronic particles is usually too low.

There are more factors that have an influence on the jet energy measurement:

- energy lost in material with no read-out (dead material);

- particles that are punching through the calorimeter (leakage);

- reconstruction effects (e.g. noise, constituent reconstruction).

The first correction is at calorimeter or constituent level. For the jets used in this thesis, the cells are calibrated at the electromagnetic scale. This means that the obtained energies are correct for electromagnetic showers but are too low for hadronic showers. This will be corrected by the jet energy scale at a later stage. In addition to this scheme there are two other schemes, *Global Cell Weighting* (GCW) and *Local Cluster Weighting* (LCW) [35]. Both schemes correct for the effects mentioned above, by reweighting the measured cell energies. In the GCW scheme, the weights are applied at the cell level and depend on the type of cell and the energy density. The cell weights are extracted from simulated data.

In the LCW scheme, a correction is determined for each constituent. These correction factors depend on the shape, location and energy density.

After cell calibration follows the calibration of the jet energies. The scale factors needed to derive the calibrated jet energies from the calibrated energies of the jet constituents are called the *jet energy scales* (JES). The calibration scheme used in this thesis is called the *EM+JES* calibration scheme. The jet energies obtained from the cells, calibrated at the EM scale, are multiplied by a constant, depending on η and jet energy. Alternatively, the GCW and LCW schemes have different jet energy scales: *GCW+JES* and *LCW+JES*. The *EM+JES* scheme is preferred for the data used in this thesis, since it was better understood than the *GCW+JES* and *LCW+JES* schemes.

The procedure of obtaining these jet energy scale corrections is described below. These correction factors are derived for anti-k_{T} jets with topocluster constituents in the *EM+JES* scheme. More details can be found in [50].

The calibration scheme entails three steps. First the average contribution of in-time pile-up (multiple interactions per bunch crossing) is subtracted from the topological clusters. This term only depends on the number of vertices in the event and not on the exact topology of the additional collisions. This slightly decreases the jet energy resolution. In the second step, the topoclusters in the jet are forced to point towards the primary vertex instead of the ATLAS origin and their momenta and directions are recalculated. Finally the calorimeter electromagnetic energy, calculated from an EM shower hypothesis, is corrected by the jet energy scale (JES), which is derived from simulations for the jets in used in this thesis.

The Monte Carlo JES correction is derived from reconstructed jets in a simulated sample of di-jet events. The jets are required to be isolated (no other reconstructed jet within $\Delta R = \sqrt{\Delta\phi^2 + \Delta\eta^2} < 2.5$ with $p_{\mathrm{T}} > 7\,\mathrm{GeV}$) and matched to a truth jet within $\Delta R < 3.0$. Truth jets are constructed by the same anti-k_{T} algorithm, but instead of using the four-momenta of the topoclusters, as in reconstruction, the four-momenta of all stable particles, except neutrinos and muons, is used. For each match the ratio of the electromagnetic jet energy E_{EM} with the truth-jet energy E_{truth} is calculated. As expected and shown in Figure 4.6 this ratio is always larger than one and decreases with higher jet energies.

Since the JES is determined from simulation, the following sources of systematical uncertainties are included.

- Method/fit quality. Instead of deriving corrections for jet energies, corrections for jet transverse momenta are determined. The non-closure is

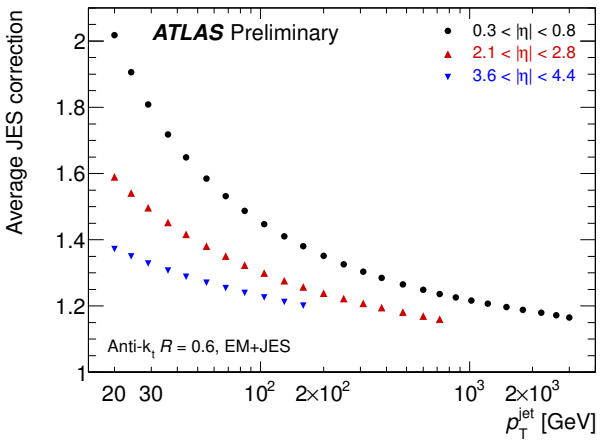

Figure 4.6: the closure of the JES (figure taken from [50]).

added as a systematic uncertainty.

- Uncertainty on the simulation of the calorimeter response. This uncertainty is estimated from pion test-beam results [51] and isolated hadron tracks [52]. Since the calorimeter response is well known in the barrel region, an extra term is added in the forward region. This extra term is derived from the transverse momentum balance in di-jet events, where one of the two jets is central.

- Modelling of electronics noise in simulation. Noise conditions in data are not constant and have an effect on the formation of topoclusters. The 4σ and 2σ noise thresholds in simulation are raised by 7 %, resembling the noise thresholds in data.

- Uncertainty of the ATLAS detector geometry description used in simulation. This is derived from simulated samples with extra dead material in front of the calorimeters.

- Theory uncertainties. Different Monte Carlo event generators are used. The results obtained with the `Pythia` generator are compared to the results obtained with the `AlpGen` generator. The `Pythia` sample only uses $2 \to 2$ matrix elements, while the `AlpGen` generator is able to produce up

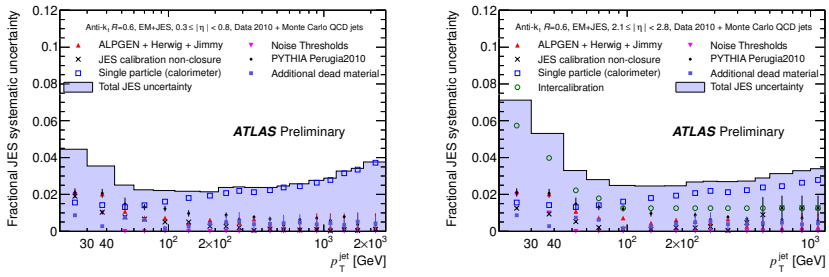

(a) (b)

Figure 4.7: jet energy scale uncertainty and its different components for the central region (a) and the forward region (b) (figures taken from [50]).

to 5 partons in the final state. The hadronisation in the `AlpGen` sample is done by `HERWIG`. In order to prevent double-counting, the MLM-matching scheme is used [23, 24, 25]. The hadronisation in the `Pythia` sample, using the string model, differs from the cluster model in the `HERWIG` sample.

In Figure 4.7, the JES uncertainties are shown for the central and forward regions. The contributions of the different sources mentioned above are shown separately. The total jet energy scale uncertainty is obtained by adding these contributions in quadrature.

In Figure 4.8, the results of four different validation analyses are shown. The photon-jet analysis [53] selects events with one photon and at least one jet. The transverse momentum of the jet and photon should balance. Also the balance is shown for missing transverse energy and a photon. The same can be done for multi-jet events [54]. For the track-jet comparison, the sum of track momenta, corrected for the fraction of charged particles in a jet, within the jet cone is compared to the jet energy.

4.3.2 Jet Energy Resolution

The jet energy resolution is determined using the transverse momentum balance in di-jet events. In ATLAS there are two methods for determining the resolution: the di-jet balance method and the bi-section method. Both are detailed in [55], but the treatment here is only confined to the di-jet balance method.

Di-jet events are selected by requiring two reconstructed jets with at least

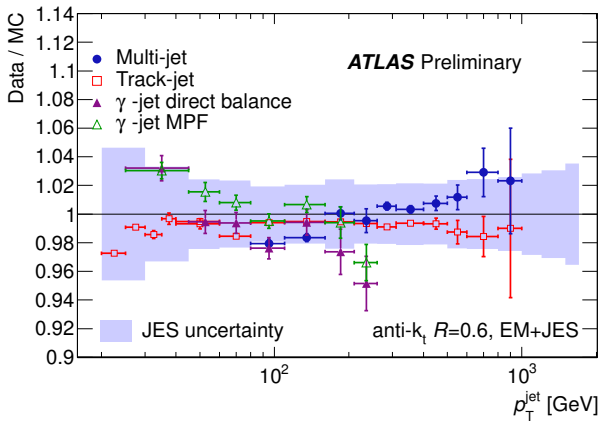

Figure 4.8: the results of jet-energy-scale validation studies as described in the text (figures taken from [50]).

$p_T > 20\,\text{GeV}$, separated by an angle $\Delta\phi \geq 2.8$ in the transverse plane. Assuming that $\sigma_{p_{T,1}} = \sigma_{p_{T,2}}$, i.e. the energy resolution of both jets is similar, the width of the Gaussian distribution of the asymmetry,

$$A = \frac{p_{T,1} - p_{T,2}}{p_{T,1} + p_{T,2}}, \tag{4.11}$$

is related to the fractional resolution:

$$\frac{\sigma_{p_T}}{p_T} = \sqrt{2}\sigma_A. \tag{4.12}$$

In order for the assumption $\sigma_{p_{T,1}} = \sigma_{p_{T,2}}$ to hold, both jets have to be in the same detector region. This effectively means $|\eta_1| \approx |\eta_2|$.

The presence of soft radiation in the form of a third jet spoils the energy balance in the transverse plane. A cut of $p_{T,3} < 10\,\text{GeV}$ is applied to minimise that effect. In order to estimate the possible bias induced by a third jet, the resolution has been fitted with decreasing cut values on the transverse momentum of the third jet. The results are then extrapolated to $p_{T,3} \to 0\,\text{GeV}$ by fitting the dependence on the third jet cut value.

The systematic uncertainties are evaluated by varying the cut value of $\Delta\phi$ between $[2.75, 3]$, which accounts for a 1% effect. Additionally a 10% uncertainty was assigned to the correction factor for soft radiation. The results of both the

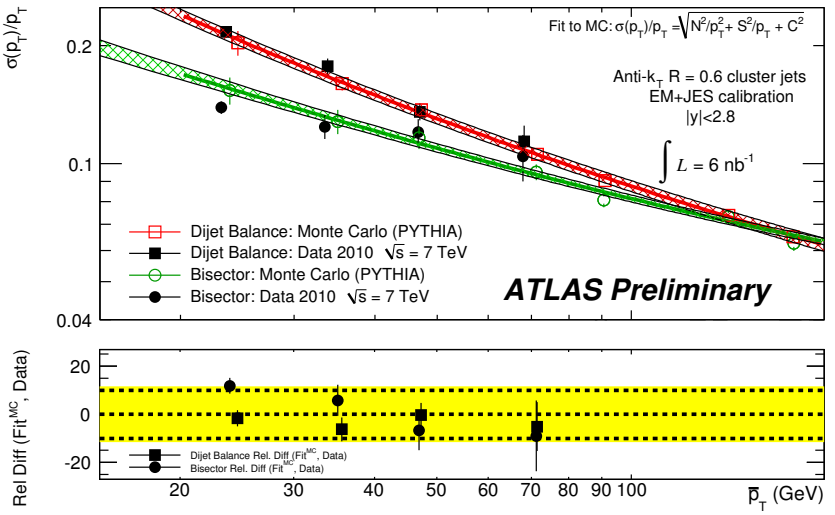

Figure 4.9: the jet energy resolution as function of the jet transverse momentum for both the bi-section and di-jet balance methods in ATLAS. The lines indicate the fit to the function from equation Eq. 4.13. In the bottom plot, the relative difference between the value obtained from simulation and the value on data is shown (figure taken from [55]).

di-jet balance and the bi-section technique are shown in Figure 4.9. Here, the p_{T} dependence of the fractional jet energy resolution has been fitted with the following function:

$$\frac{\sigma_{p_{\mathrm{T}}}}{p_{\mathrm{T}}} = \frac{N}{p_{\mathrm{T}}} \oplus \frac{S}{\sqrt{p_{\mathrm{T}}}} \oplus C, \tag{4.13}$$

where N, S and C are the free parameters. These parameters have however a physical interpretation: N reflects the dependency of the resolution on calorimeter noise, S reflects the dependency on stochastic fluctuations in the amount of hadronic energy sampled. Finally an additional term not dependent on p_{T}, called C, is added that reflects calibration uncertainties. In the top plot of Figure 4.9, the bias due to multiple jets in the di-jet balance method explains the difference at low p_{T} values.

4.4 Missing Transverse Energy

Missing transverse energy is the only handle on particles that do not interact with the sensitive detector material, such as the neutrino. Also, supersymmetric models predict stable particles that do not interact with ordinary matter.

Reconstruction of missing transverse energy starts by a vector sum of all the calibrated calorimeter cell energies: $E_{x,y}^{\text{calo}}$. Noise suppression is achieved by only taking into account the cells that belong to topological clusters. The transverse energy of a calorimeter cell is obtained by projecting the energy of the cell using the polar angle of the vector pointing from the origin of ATLAS to the centre of the cell.

Energy lost inside the cryostat inactive material that surrounds the LAr electromagnetic calorimeter, $E_{x,y}^{\text{cryo}}$, is calculated from the last layer of the EM calorimeter and the first layer of the Tile calorimeter.

Muons are not absorbed in the calorimeter. For non-isolated muons, the $E_{x,y}^{\mu}$ term is constructed by adding the momentum of the muon spectrometer tracks. In order to reduce fakes from cosmic muons and punch-through, the muons are required to be combined with an inner detector track. If the muon is isolated and combined, the p_{T} is given by the combined fit. In this case, the topological cluster containing the muon deposits can be identified and removed from calculation, preventing double counting. Outside the inner-detector acceptance region, only the spectrometer track information can be used.

The calculation of missing transverse energy is done as follows:

$$E_{x,y}^{\text{miss}} = -\left(E_{x,y}^{\text{calo}} + E_{x,y}^{\text{cryo}} + E_{x,y}^{\mu}\right), \tag{4.14}$$

$$E_{\text{T}}^{\text{miss}} = \sqrt{(E_x^{\text{miss}})^2 + (E_y^{\text{miss}})^2}. \tag{4.15}$$

An improved method for calculating missing transverse energy exists, which is called refined missing transverse energy. The calorimeter cells that are matched to identified high p_{T} objects, such as electrons, photons, taus and jets, are replaced by the p_{T} of the identified object. The missing transverse energy components are then calculated as:

$$\begin{aligned} E_{x,y}^{\text{miss}} = & -\sum_i E_{x,y}^{e_i} - \sum_i E_{x,y}^{\gamma_i} - \sum_i E_{x,y}^{\tau_i} \\ & - \sum_i E_{x,y}^{\text{jet}_i} - \sum_i E_{x,y}^{\mu_i} - E_{x,y}^{\text{CellOut}}, \end{aligned} \tag{4.16}$$

where the CellOut term is the sum of all the calorimeter cell energies in topoclusters that were not associated to any reconstructed physics object. In Chapter 6, the refined missing transverse energy is used.

4.4.1 Performance

Missing Transverse Energy Cleaning

Noise bursts in the calorimeter can produce fake jets or fake missing transverse energy. This happens most often in the forward region or HEC calorimeter and produces tails in the missing transverse energy distribution. In early studies on minimum-bias data[4], tails with high missing transverse energy are observed that are not predicted in simulation, since the simulation does not model these noise bursts. The following set of cleaning cuts have been developed [56]:

HEC cleaning: in order to reduce fake jets originating from noise bursts in the HEC, the fraction of energy originating from cells located in the HEC should be less than 80 % if the number of cells accounting for at least 90 % of the energy is fewer than six;

EM cleaning: coherent noise in the electromagnetic calorimeter is detected by comparing the measured pulse shape with the reference pulse shape. Jets are flagged as bad if more than 80 % of the cells do not compare well to the reference shape and more than 95 % of the jet energy is located in the electromagnetic calorimeter.

The missing transverse energy is considered unreliable for events having jets that are flagged as bad. In Figure 4.10, a comparison is shown on minimum-bias events with Monte Carlo. The "DQ + collisions" histogram is obtained from all minimum-bias-triggered collision data and shows a longer tail than expected from simulation. The long tail, induced by HEC noise bursts, is successfully removed[5]. The data points are indicating the resulting distribution when also the EM cleaning cuts are applied.

[4] More details about minimum-bias can be found in Section 4.6.1. For now it is only relevant that it is not very likely for minimum-bias events to have high missing transverse energy.

[5] Since the rate of neutrino production is very low in minimum-bias events, they are not expected to have missing transverse energy.

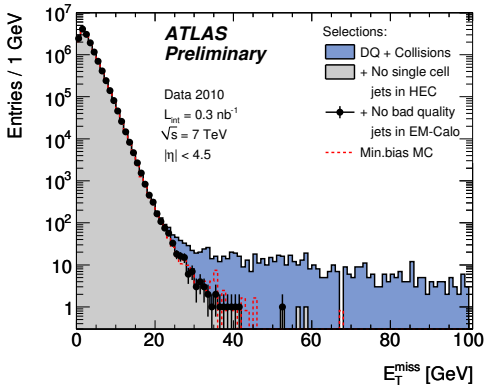

Figure 4.10: resulting missing transverse energy distribution before and after jet cleaning (figure taken from [56]).

Missing Transverse Energy Resolution

The missing transverse energy resolution is parameterised as:

$$\sigma(E_{\mathrm{T}}^{\mathrm{miss}}) \quad = \quad \alpha\sqrt{\sum E_{\mathrm{T}}}, \tag{4.17}$$

where $\sum E_{\mathrm{T}}$ is the sum of all transverse energies from all the topoclusters. The parameter α is determined from a fit of the width of the missing transverse energy distribution as a function of $\sqrt{\sum E_{\mathrm{T}}}$. The results for minimum-bias collisions are shown in Figure 4.11. More details on the measurement and fit of the missing transverse energy resolution can be found in [57].

4.5 Other Physics Objects

4.5.1 Electrons and Photons

Electrons and photons are identified in the EM calorimeter, where they deposit their energy in a calorimeter cluster which can consist of up to 50 cells. Electromagnetic clusters, coming either from photons or electrons, are then distinguished from hadronic cluster by cuts on shower-shape variables such as the longitudinal and lateral profile.

If an electromagnetic cluster is found, it is attempted to match it to an inner-detector track. Electrons are identified by a track match. For electrons

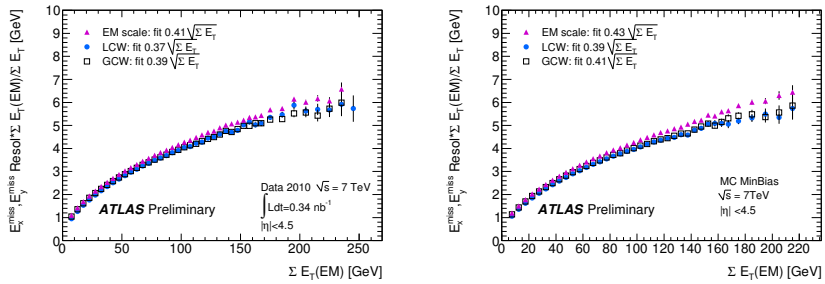

Figure 4.11: missing transverse energy resolution as a function of $\sqrt{\sum E_{\mathrm{T}}}$ in minimum-bias data (a) and Monte Carlo (b) (figures taken from [57]).

with $p_{\mathrm{T}} > 20\,\mathrm{GeV}$, the energy is determined from the deposited energy in the calorimeter, and not from the track. Electron backgrounds, or fakes, are reduced by tighter cuts on the shower shapes, a cut on the $E_{\mathrm{calo}}/E_{\mathrm{track}}$ ratio and requiring a high ratio of high-threshold TRT hits.

Photons are identified by electromagnetic clusters with no matching track, or match with two tracks that are compatible with a photon conversion.

4.5.2 Tau leptons

The leptonic decay of a tau into a muon or electron is very hard to identify in general. The tau identification procedure is based on the hadronic decay modes of taus, that have a combined branching ratio of 65 %.

Hadronically decaying tau leptons are identified by matching a narrow calorimeter cluster with a small number of tracks located in a narrow cone. Several variables are identified to separate taus from jets. These include the shower profile in the electromagnetic calorimeter, the calorimeter isolation of the tau-candidate cluster, the ratio of the cluster energy with respect to the matched track that has the highest p_{T}, the sum of the charges, the number of tracks and the invariant mass of the tracks. Three methods are used to identify taus: a cut-based method, a likelihood method and a neural network.

4.5.3 B-Tagging

Since b hadron decay via the emission of a W boson is suppressed by the small CKM-matrix elements, they decay at detectable distances from the primary vertex. Separating b hadron decays from decays of hadrons found in light jets is done using multivariate techniques. There exist likelihood and neural network methods. Distributions that are used as inputs are the invariant mass of the tracks forming the secondary vertex, the energy fraction of the tracks originating from the secondary vertex with respect to the sum of all the tracks and the number of secondary vertices from at least two tracks.

4.6 Inclusive Muon Production

In this section a measurement is presented of the production sources of muons in early $\sqrt{s} = 7\,\text{TeV}$ pp-collision data taken in 2010. In the early periods of data taking, trigger thresholds could be very low due to the low instantaneous luminosity. In this study low transverse-momentum muons are studied. Muon production is dominated by QCD processes in which hadrons that decay into muons are produced.

We have made a distinction of two types of muons depending on the decay time of their hadron ancestors. The first category, called the prompt category, consists of hadrons that have a proper decay time of less than one nanosecond. These unstable hadrons usually decay before reaching the sensitive detector elements.[6] The second, or non-prompt, category, are hadrons that do interact with the detector material. Although these hadrons are usually absorbed in the calorimeter, they have a non-zero probability of decaying in flight. These decays-in-flight are dominated by pions and kaons. Since these hadrons are copiously produced, they form the dominant production mechanism for low momentum muons. For higher momenta, the relativistic boost suppresses the decay probability.

Although muons can also be produced by the decay of weak vector bosons and taus, they can be safely neglected in the data set used for this study. The study presented here is therefore aimed at measuring the heavy-flavour fraction, i.e. the fraction of muons originating from the decay of a hadron containing a b or a c quark.

In Section 4.6.1 the selection procedure and data set is described, followed by the method description in Section 4.6.2. The sources of systematic uncertainties are detailed in Section 4.6.4, the closure test of the method in Section 4.6.5 and the results are given in Section 4.6.6. The results of this study were presented at the ICHEP conference of 2010 [58] and also in the associated public ATLAS conference note [59]. The method was later applied for revealing the production sources of the di-muon spectrum as well [60].

4.6.1 Data Sets and Event Selection

This analysis is based on an integrated luminosity of approximately 17 pb^{-1} taken by the ATLAS detector obtained during stable LHC beams. Only data for which the subsystems relevant for the reconstruction of muons and tracks

[6] Note that this definition of prompt-muons also includes muons from heavy-flavoured hadron decays.

Trigger	Muon trigger with no momentum threshold
Event	At least one vertex with three tracks
	A track is counted when $n_{\text{pixel}} \geq 1$ and $n_{\text{SCT}} \geq 6$
Muon	Combined with ID track
	$p_{\text{T}} > 4\,\text{GeV}$
	$\lvert\eta\rvert < 2.5$
	$n_{\text{pixel}} \geq 1$ and $n_{\text{SCT}} \geq 6$ required for ID track

Table 4.1: selection cuts for the inclusive-muon analysis.

are operating at nominal conditions are considered. Also the solenoid and toroid magnetic fields are required to be at full field strength.

The first step of the event selection is requiring a muon to be seen at the first level trigger with no momentum threshold. In order to reduce possible background from cosmic muons, the timing of the event should coincide with paired or colliding proton bunches. This background is further suppressed by requiring a reconstructed vertex with at least three good tracks. A track is considered good if it has at least one pixel hit and six SCT hits.

The muon is selected by requiring at least one combined muon (reconstructed with Chain 2; see Section 4.2) with $p_{\text{T}} > 4\,\text{GeV}$ within $|\eta| < 2.5$. The $p_{\text{T}} > 4\,\text{GeV}$ cut is motivated by the energy loss in the calorimeters, which for muons is 3 GeV on average. The associated inner detector track must have at least one hit in the pixel detector and at least six hits in the SCT. A sample of 157466 muons is obtained after this selection. The selection cuts are summarised in Table 4.1.

Monte Carlo data samples have also been generated in order to compare the measurement to Standard Model predictions. The `Pythia` 6.4 generator [16] is used for this task and is configured to produce minimum-bias events. There are three types of minimum-bias collisions: single diffractive, double diffractive and non diffractive. In double-diffractive events, both colliding protons survive and usually this is not seen in the detector at all. In single-diffractive events only one proton breaks up and ends up as a (usually very forward) jet in one side of the detector. However, the more energetic or interesting events are the non-diffractive events where both protons break up.

For the non-diffractive minimum-bias samples generated by `Pythia`, all possible processes that could occur in $\sqrt{s} = 7\,\text{TeV}$ pp-collisions are switched on. After generating the event, the detector response for the generated Monte Carlo samples is simulated using `GEANT4` and reconstructed (see Section 3.2.6). Five

data sets are simulated using Monte Carlo techniques and are listed below.

- A sample of 20 million non-diffractive minimum-bias events produced with the MC09 tune [61].
- A sample of 40 million non-diffractive minimum-bias events (MC09 tune) filtered at generation level to have at least one region of size $\Delta\eta \times \Delta\phi = 0.2 \times 0.2$ containing a total transverse momentum larger than 6 GeV.
- A sample of 10 million non-diffractive minimum-bias events (MC09 tune) filtered at generation level to have at least one region of size $\Delta\eta \times \Delta\phi = 0.2 \times 0.2$ containing a total transverse momentum larger than 17 GeV.
- A sample of 5 million events produced with the Perugia0 [62] tune.
- A sample of 5 million events produced with the DW tune [63].

Throughout this section, the term "minimum-bias simulation" refers to the MC09 tune. The term "di-jet sample" refers to the 17 GeV filtered sample.

The rate of muon production in these minimum-bias generated samples is very low. Unfortunately, for this study it is impossible to filter events that have muons at the generation stage. This is because the pion and kaon decays are located somewhere in the detector and the energy loss of these hadrons with the detector material has to be taken into account.

Despite the high initial statistics of the standard minimum-bias sample, the number of high-p_{T} muons is limited. The filtered samples, however, provide a solution, since the muons in those samples have a higher p_{T} on average. Reweighting techniques have been applied in order to reproduce the kinematic distributions of the muons measured in data for these samples.

4.6.2 Analysis Method

Description

Pions and kaons may cross a large part of the detector before decaying, because of their long lifetime. Although the muon is emitted isotropically in the rest frame of the pion (kaon), the angles between the decaying particle and the muon in the lab system are usually small due to the Lorentz boost and the small mass difference. Because of this, the tracker hits from the two particles are often associated to the same track.

In general, the momentum measurement in the muon spectrometer will correspond to the muon trajectory. The measurement in the inner detector is instead

Muon origin	Percentage
Heavy-flavour decay	43 %
Pion decay within ID volume $r < 400$mm	6 %
Pion decay within ID volume $r > 400$mm	13 %
Pion decay in calorimeter	12 %
Kaon decay within ID volume $r < 400$mm	4 %
Kaon decay within ID volume $r > 400$mm	12 %
Kaon decay in calorimeter	10 %
Fake	$< 1\%$
Other prompt muons	$< 1\%$

Table 4.2: sources of muon production in the minimum-bias simulation.

dominated either by the pion (kaon) momentum or by the muon momentum, depending on the decay distance. For muons produced close to the interaction point this discrepancy between inner-detector and muon-spectrometer measurement does not occur. These muons are called prompt muons and are usually produced from the decay of heavy-flavoured hadrons or W and Z bosons.

Using these considerations, we can define

$$\frac{\Delta p_{\text{loss}}}{p_{\text{ID}}} = \frac{p_{\text{ID}} - p_{\text{MS}} - p_{\text{param}}}{p_{\text{ID}}}, \tag{4.18}$$

where p_{ID} and p_{MS} are the momenta as measured in the inner detector and in the muon spectrometer respectively, while p_{param} is the parameterised estimate of the energy lost by a muon crossing the material between the two devices. For prompt muons this distribution will peak around zero. However, in the case of a pion or kaon decay, momentum will be lost to the neutrino. The distribution of this variable for the different components, as predicted by the minimum-bias simulation, is shown in Figure 4.12(a) and confirms our previous observations. The expected muon transverse momentum spectra are plotted in Figure 4.12(b) and are overlaid with the observed data. In Table 4.2 the sources of muon production in the minimum-bias simulation are broken up into different categories.

The method that we present is based on a likelihood fit of the yields of the prompt and the pion/kaon components. The inputs for the fit are the distributions, called templates, of $\Delta p_{\text{loss}}/p_{\text{ID}}$ for the prompt and non-prompt components. In the present work, they are derived from simulated events. Alternatively, the models can be constructed from data by selecting muons from

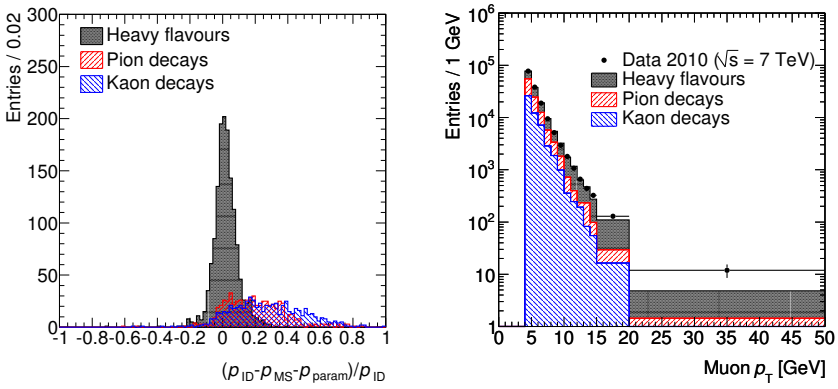

(a) (b)

Figure 4.12: the distribution of $\Delta p_{\text{loss}}/p_{\text{ID}}$ for different components, as predicted by the minimum-bias simulation and for reconstructed muons with $p_{\text{T}} > 6\,\text{GeV}$ (a) and the expected transverse momentum spectra of the different components, overlapped by the observed data (b).

J/ψ and Υ decays and pions from K_s and Λ resonances. When this analysis was performed, this was not possible due to the low number of recorded J/ψ and Υ decays at $17\,\text{pb}^{-1}$. In Section 4.6.3 we use such resonances to validate the simulation-based templates.

The templates are built from a sample of muons extracted from simulated events in the di-jet sample. The topology of the events in the di-jet sample differs from the minimum-bias data. The 17 GeV filter introduces a slight bias to higher jet p_{T}. As a consequence, the muon energy isolation distribution from the di-jet sample is different from the minimum-bias sample. However, from Figure 4.13 we can safely assume that this will have a negligible impact on the template shapes.

The templates are built in a non-parametric way and the shape of each component is represented by a probability density function derived using the kernel estimation technique [64]. Every value of $\Delta p_{\text{loss}}/p_{\text{ID}}$ yields a Gaussian with a width that depends on the local density: the higher the density the smaller the width. By adding the Gaussians for all the values, a continuous probability density function is obtained.

Figure 4.14 shows the templates for heavy-flavour and pion/kaon compo-

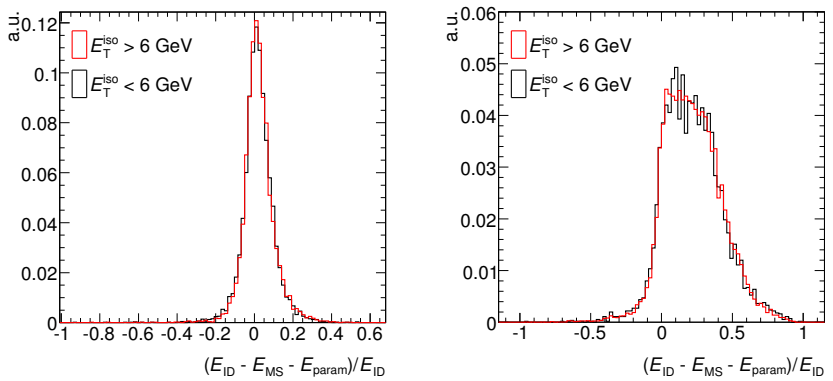

(a) (b)

Figure 4.13: the dependence of the $\Delta p_{\text{loss}}/p_{\text{ID}}$ distribution on muon transverse energy isolation collected in a cone of radius $R = \sqrt{\Delta\eta^2 + \Delta\phi^2} = 0.4$. It is shown that a cut on transverse energy isolation has a negligible effect on the signal component (a) or pion and kaon component (b).

nents respectively for muons with transverse momentum between 6 and 8 GeV, as obtained from simulated di-jet events. For the sake of comparison, also the minimum-bias simulated data are shown, represented by full and open points. The minimum-bias and the di-jet templates agree within the statistical uncertainty.

4.6.3 Template Validation on Data

In this section we discuss the validation of the simulation-based templates with data.

To validate the prompt-muon component we select muons coming from decays of J/ψ. We select opposite-sign di-muon events, where one muon has to pass the selection criteria listed in Table 4.1, while for the second muon we relax the kinematic cuts to $p_{\text{T}} > 2$ GeV. Finally, we select an almost pure J/ψ sample by requiring that for the invariant mass $M_{\mu\mu}$ of the di-muon we have $2.5\,\text{GeV} < M_{\mu\mu} < 3.5\,\text{GeV}$. Figure 4.15(a) shows the $\Delta p_{\text{loss}}/p_{\text{ID}}$ distribution for the surviving events as well as the prompt-muon template from simulated di-jet events. The template describes the prompt muons from J/ψ accurately.

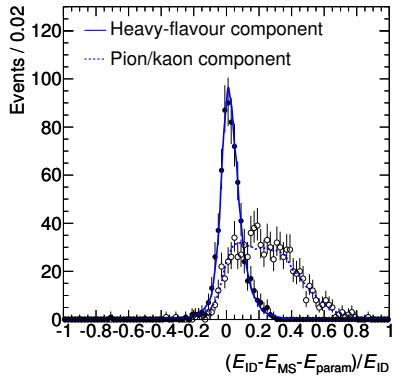

Figure 4.14: templates for heavy-flavour and pion/kaon components for muons with transverse momentum between 6 and 8 GeV, as obtained from simulated QCD events. For the sake of comparison, also the minimum-bias simulated data are shown, represented by full and open points for the prompt and non-prompt components respectively.

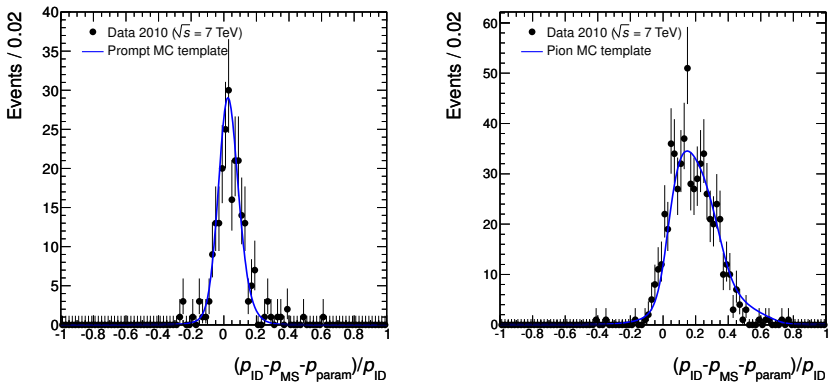

(a) (b)

Figure 4.15: template for prompt-muon component (a) superimposed on top of muons from J/ψ decays. Template for pion component (b) superimposed on top of muons from $K_s \to \pi^+\pi^-$ decays.

Similarly we validate the pion template by selecting $K_s \to \pi^+\pi^-$ decays. A muon, again identified via the cuts listed in Table 4.1, is paired with an inner detector track. This track is required to share a secondary vertex with another oppositely charged muon. The K_s decays are selected by requiring the invariant mass $M_{\pi\pi}$ of the two-track system to be inside the window $475\,\text{MeV} < M_{\pi\pi} < 520\,\text{MeV}$. Figure 4.15(b) shows the $\Delta p_{\text{loss}}/p_{\text{ID}}$ distribution for the selected K_s events. The pion template built from simulated di-jet events is superimposed on top of the data-driven template from K_s decays and shows a good agreement with data.

4.6.4 Systematic Uncertainties

In order to account for differences in shape between data and simulation, the templates are extended with three parameters that model several detector effects. A translation in $\Delta p_{\text{loss}}/p_{\text{ID}}$ accounts for uncertainty in the momentum scale (shift parameter), while a Gaussian smearing describes the effect of a momentum resolution that is worse in data than in simulation (smear parameter). In addition, the distribution can be dilated with respect to its mean along the abscissa (stretch parameter). This parameter is not directly motivated by detector effects, but it has been included in order to allow more general distortions of the template shape.

To estimate the pion and kaon contamination in data, we construct an unbinned profile likelihood [65] as a function of the prompt-muon fraction where the three distortion parameters are left free to float and are treated as nuisance parameters. Figure 4.16 shows the template distributions for different values of the three nuisance parameters, as well as for different pion and kaon contents.

Any additional systematic uncertainties are estimated as the variation of the best fit value after each of the following changes:

template shape uncertainty: the templates are derived from minimum-bias simulated events;

template uncertainty on relative pion/kaon content: the pion (kaon) content in the non-prompt muon template is increased by a factor two.

Figure 4.17 shows the variations of the best fit value of the prompt-muon fraction for each systematic uncertainty mentioned above. The variation of the best fit value after replacing the di-jet templates by minimum-bias templates are shown in Figure 4.18. Due to the low statistics in the minimum-bias sample,

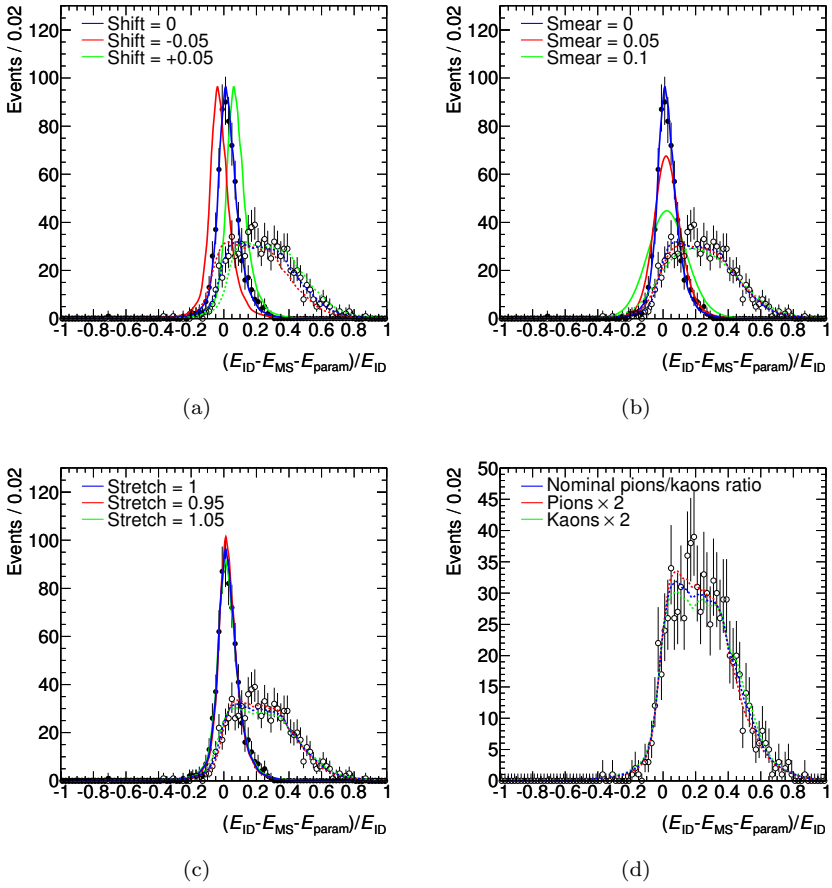

Figure 4.16: template distributions for the nuisance parameters shift (a), smear (b), stretch (c), and for different values of the pion and kaon content (d). All the distributions are shown for reconstructed muons with $6\,\text{GeV} < p_{\text{T}} < 8\,\text{GeV}$.

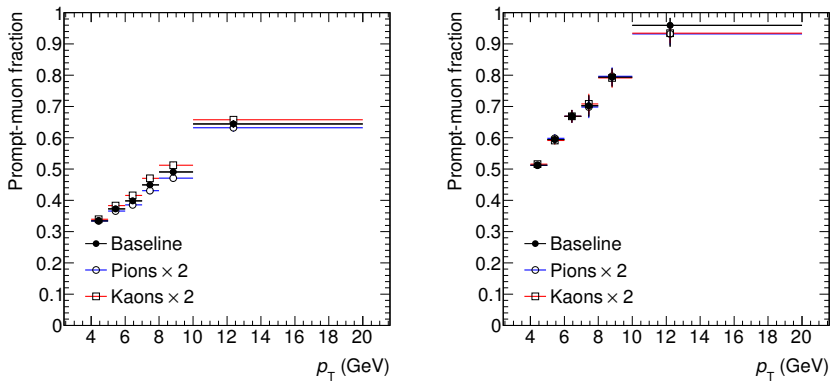

(a) (b)

Figure 4.17: variations of the best fit value of the prompt-muon fraction after multiplying the pion/kaon content by a factor of two for the barrel (a) and for the end-cap (b).

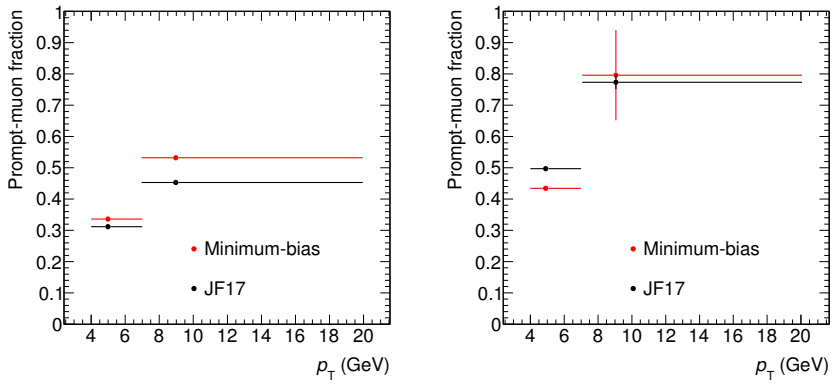

(a) (b)

Figure 4.18: variations of the best fit value of the prompt-muon fraction after replacing the di-jet templates with minimum-bias templates are shown for the barrel (a) and the end-cap (b).

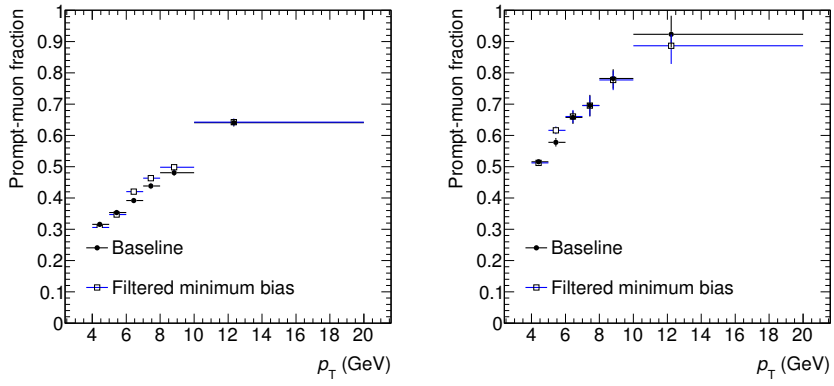

(a) (b)

Figure 4.19: comparison of the best fit values of the prompt-muon fraction based on the di-jet templates (baseline, full circles) and on the p_T-filtered minimum-bias templates (empty squares). Barrel and end-cap are respectively shown in (a) and (b).

the binning is chosen differently from the baseline and the relative difference is propagated to the corresponding bins.

Since the p_T threshold in the di-jet sample, which is set to 17 GeV, is higher than the typical muon transverse momenta considered in this analysis, a test is needed in order to ensure that no biases are introduced in the template building. Thus, the template shapes obtained with the di-jet sample, together with the fit results derived from them, have been cross-checked with the p_T-filtered minimum-bias events described in Section 4.6.1. Figure 4.19 shows the fit results based on the p_T-filtered minimum-bias templates compared with the di-jet templates. The two sets of results are compatible. The di-jet sample is then kept as baseline for template building, as it provides the best muon statistics especially at high transverse momenta.

4.6.5 Closure Test

The method is applied to three different simulated samples of minimum-bias events. The templates derived from the di-jet simulation are used to fit the known prompt-muon fractions in these samples. If the method is correct, it

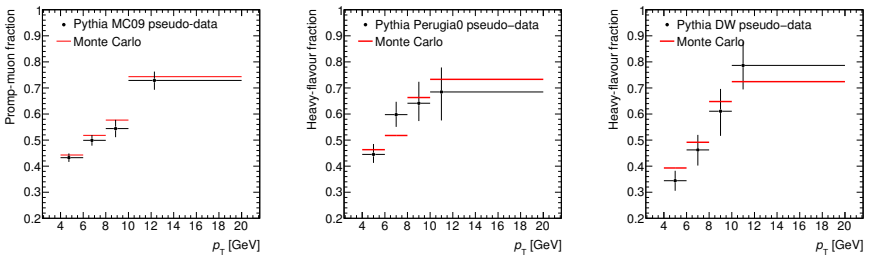

(a) (b) (c)

Figure 4.20: estimated prompt-muon component as a function of p_{T}, for three different simulated samples as described in the text. The error bars are derived from the 68 % confidence level of the profile likelihood. The lines without markers represent the predictions obtained from the minimum-bias simulated model. Note that for all fits the templates are obtained from the QCD sample.

will estimate the correct, known yields. This procedure is called a closure test. Since the templates are derived from the di-jet simulation they are statistically independent of the minimum-bias samples used for the closure.

The fit is repeated on the three minimum-bias models listed in Section 4.6.1 and in different p_{T} bins. The templates used for all the fits are obtained from the QCD sample using the kernel-estimation technique. The results are summarised in Figure 4.20. As can be noticed, the estimates are in good agreement with the simulated yields. All the best-fit values of the nuisance parameters are checked to be compatible with the ideal-case values.

4.6.6 Results

The measurement is done in p_{T} bins, ranging from 4 to 20 GeV. Two rapidity regions are fitted separately because of the different detector instrumentation: a central region bounded by $|\eta| = 1.8$, where the inner-detector transition between barrel and end-cap takes place, and a forward region covering up to $|\eta| = 2.5$. For each bin in data, the template distributions are derived from the corresponding bin in the simulated data.

The data rapidity bins are divided in positive and negative rapidity values,

due to slight alignment differences between both sides of the detector.[7] For the final result, the two end-cap and two barrel bins are merged. Four examples of best-fit distributions obtained are reported in Figure 4.21.

The fit results as function of the muon p_{T} are summarised in Figure 4.22(a) for muons within the pseudo-rapidity region $|\eta| < 1.8$. Similarly, Figure 4.22(b) reports the fit results for $|\eta| > 1.8$. The error bars are derived from the 68 % confidence level of the profile likelihood. The bands are instead calculated by summing in quadrature the fit and the systematics uncertainties on the templates, as described in Section 4.6.4. The lines without markers represent the predictions obtained from the minimum-bias simulation, with their statistical uncertainties.

The muon sample considered here contains a large contamination from pion and kaon decays, although the fraction of prompt muons becomes larger than 50 % above 10 GeV in the central region and above 5 GeV in the forward region.

The prompt-muon fraction in the data agrees within systematic uncertainties with the prediction of the minimum-bias simulation, although the measured central value is mostly below the expected value. A disagreement is not unexpected as the simulation is not tuned specifically to reproduce the heavy-flavour content. Moreover, the simulation is based on a leading-order generator which might imply a variation with respect to bottom and charm production as compared to the data. The overall evolution as function of p_{T} of the prompt-muon fraction in data is comparable to the Monte Carlo expectation.

4.6.7 Conclusion

We have described a data-driven method to estimate the pion and kaon contamination in a data sample with a muon in the final state. The method has been applied to a set of muon triggered events, finding a fraction of prompt muons from heavy-flavour decays compatible with the value predicted by the minimum-bias simulation within systematic uncertainties.

Although the fraction of prompt muons increases at higher p_{T}, in the range of values considered in this study, we can conclude that the muon production is dominated by pion and kaon decays. It should also be noticed that this component is dependent on the track quality, since hadronic interactions lead to additional scattering and thus to missing detector hits along the track path.

[7] Note that the smear nuisance parameter covers this.

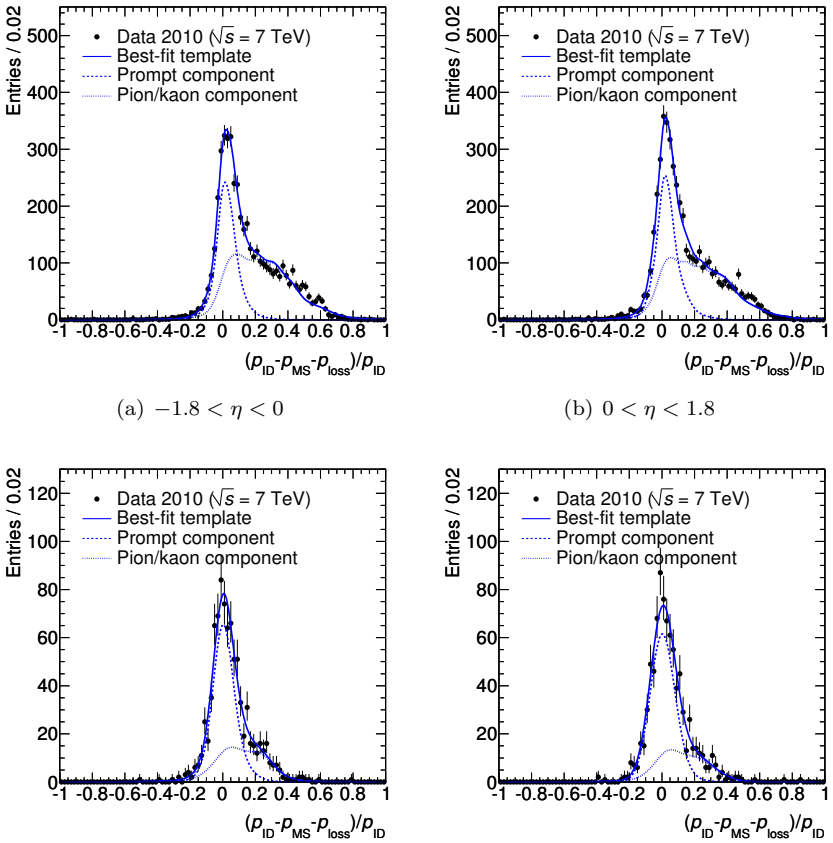

(a) $-1.8 < \eta < 0$ (b) $0 < \eta < 1.8$

(c) $-2.5 < \eta < -1.8$ (d) $1.8 < \eta < 2.5$

Figure 4.21: best-fit distributions obtained for $7\,\text{GeV} < p_{\text{T}} < 8\,\text{GeV}$ in four different pseudo-rapidity regions.

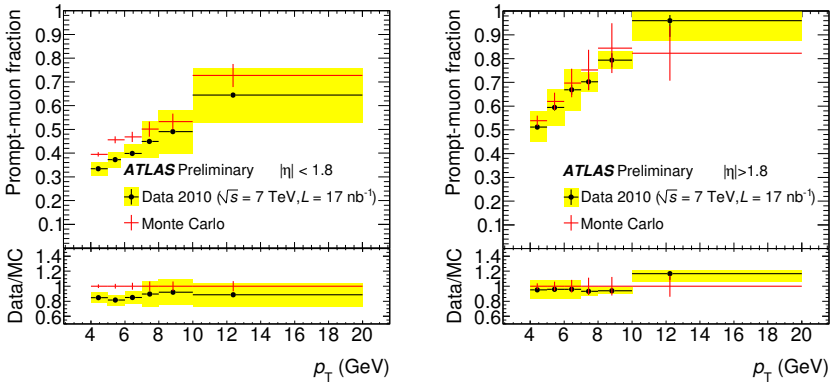

(a) barrel (b) end-cap

Figure 4.22: measured prompt component as function of p_{T} for muons with $|\eta| < 1.8$ (a) and $|\eta| > 1.8$ (b). The error bars are derived from the 68 % confidence level of the profile likelihood. The bands are instead calculated by summing in quadrature the fit and the systematics uncertainties on the templates. The lines without markers represent the predictions obtained from the minimum-bias simulated model, with their statistical uncertainties.

5

Calorimeter Muon Tagging

As described in Chapter 4, muon identification is mainly done by using information from the muon system. In the middle of the muon system, there is a gap in order to make space for services needed by the inner detector and calorimeter. This gap is small, $|\eta| < 0.1$, but the muon reconstruction efficiency is very low in that region (see Section 4.2.1). This particularly holds for the interesting, high-p_{T} muons, since they are not bent back into the muon system. In this chapter an alternative method for muon reconstruction is presented that is independent of the muon system. The method relies only on inner detector and calorimeter information. Since the calorimeter does not have a gap in the central part, calorimeter muon reconstruction is complementary to the ordinary muon reconstruction in that region. The efficiency gain is important for analyses that use multiple muons in the final state. An additional benefit from calorimeter muon reconstruction is that it is independent of the muon system and therefore can be used to study the ordinary muon reconstruction in the muon system.

The algorithm is outlined in Section 5.1 and the performance is discussed in Section 5.2. Finally an outlook to a possible improvement of the algorithm is given in Section 5.3. The algorithm was first developed by Gustavo Ordoñez and Nicolo de Groot [66]. I worked mainly on improvements on the extrapolation and the introduction of p_{T} dependent tagging (see Section 5.1.2 and Section 5.1.3). In addition I validated the performance of the algorithm on data (see Section 5.2) and studied the possibility of using a neural network (see Section 5.3).

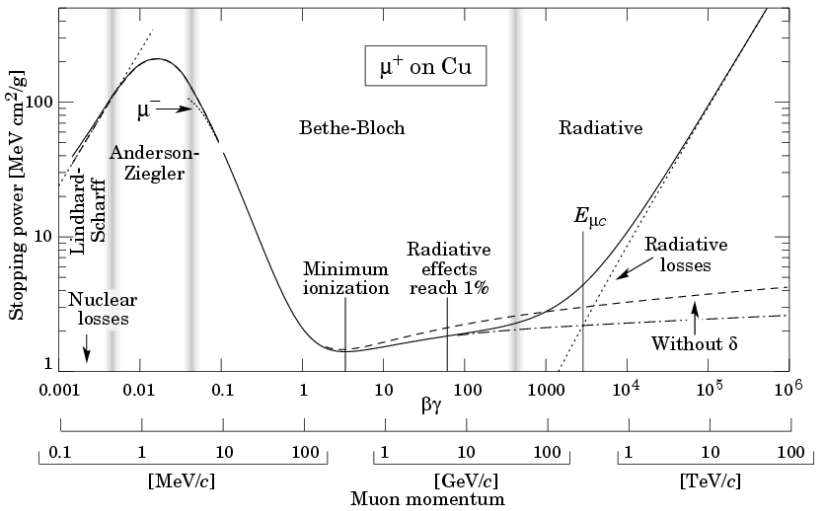

Figure 5.1: the contributions of muon energy loss through iron. Not all energy-loss mechanisms in the picture are described in the text. A more detailed treatment can be found in [68] or in section 27 from [4], where also the figure is taken from.

5.1 Description

The energy loss of a particle through matter has contributions from ionisation, bremsstrahlung, pair production and nuclear interactions [4]. As visible in Figure 5.1, for the high-p_{T} muons typically produced via weak interactions (10-100 GeV), the energy loss through ionisation is dominant. This means that the muon will not produce extended showers like electrons or hadrons. In addition, the muon energy loss through ionisation is close its value at the minimum. In general, particles that interact in this way with matter are called minimum ionising particles (MIPs). Since electrons and charged hadrons do not have this behaviour, this typical energy signature can be used for muon tagging of tracks.[1]

The outline of the muon-identification algorithm is as follows:

- select a reconstructed inner-detector track;

[1] The algorithm, actually being a MIP tagger, has been used for exotic-particle searches as well. See [67].

- extrapolate the track through the calorimeter and obtain the deposited energies in each cell;
- using the deposited energies, decide whether the track is a muon or not.

There are two separate tagging methods:

- require the deposited energies to lie within a window. This algorithm is called `CaloMuonTag` and is discussed in Section 5.1.3;
- calculate a muon likelihood ratio using the collected deposits. This algorithm is called `CaloLikelihoodRatio` and is discussed in Section 5.1.4.

The algorithm is written in `C++` and embedded in the `Athena` software framework [40]. Both methods are packaged into one calorimeter muon-identification framework called `CaloTrkMuId`. The driver algorithm, `CaloTrkMuIdAlg`, performs common operations and executes both tagging methods listed above. The driver algorithm is included in the default ATLAS *pp* reconstruction chain. This section proceeds by first describing the track selection in Section 5.1.1 and collection of the deposits in Section 5.1.2. This is then followed by the descriptions for each method.

5.1.1 Track Selection

Each reconstructed track is subjected to the following loose track-selection criteria:

- a transverse momentum larger than 2 GeV;
- at least one hit in the pixel detector;
- at least six hits in the SCT detector;
- relative track isolation, $p_{\mathrm{T}}^{\mathrm{iso}}/p_{\mathrm{T}}$, less than 8;
- energy isolation cuts as displayed in Table 5.1.

The track isolation in a cone of 0.45 around the considered track is defined as,

$$p_{\mathrm{T}}^{\mathrm{iso}} \quad = \quad \sum_{j} p_{\mathrm{T}\,j}\,, \tag{5.1}$$

where $p_{\mathrm{T},j}$ is the transverse momentum of an inner detector track j that is separated from the track by $\Delta R = \sqrt{\Delta\phi^2 + \Delta\eta^2} < 0.45$. Notice that the

Region	Cut
Barrel	$E^{\text{iso}} < 17\,\text{GeV}$
	$E_{\text{T}}^{\text{iso}}/p_{\text{T}} < 3$
Transition	$E^{\text{iso}} < 10\,\text{GeV}$
	$E_{\text{T}}^{\text{iso}}/p_{\text{T}} < 1.4$
End-cap	$E^{\text{iso}} < 13\,\text{GeV}$
	$E_{\text{T}}^{\text{iso}}/p_{\text{T}} < 1.6$

Table 5.1: energy isolation cuts used in the `CaloTrkMuId` algorithm. The barrel region is defined as $|\eta| < 1.5$, the transition region is defined as $1.5 < |\eta| < 1.8$ and the end-cap region is defined as $|\eta| > 2.5$.

sum does not include the p_{T} of the original track. For non-isolated tracks the deposits of adjacent particles mix with the deposits of the track under investigation. The non-isolated tracks therefore have a higher misidentification rate and a lower efficiency. In principle an isolation cut can also be applied at the physics-analysis stage instead of at reconstruction stage. However, applying the isolation cuts at reconstruction stage speeds up the algorithm by reducing the number of tracks that have to be extrapolated through the calorimeter.

Energy isolation is defined as the sum of all calorimeter cell energies that lie in a cone ΔR around the track. The energies deposited in cells traversed by the particle are subtracted. Since energy isolation takes the energy from neutral particles into account it is complementary to the track isolation cut. The energy-isolation cuts are displayed in Table 5.1. The cone size used is $\Delta R < 0.4$.

5.1.2 Collecting Deposits

In Table 5.2 an overview of the calorimeter subsystems used for muon identification is given. The forward hadronic calorimeter is not used since no tracks are reconstructed with $|\eta| > 2.5$. Since the calorimeters are not fully projective, the η coverage is approximate and depends on the radial or axial depth. Although the cylinder and wheel geometries are not genuinely different, the distinction is made to express the different segmentation of the layers. Cylindrical calorimeter geometries have radial segmentation, while the wheel-type calorimeters have an axial segmentation.

The symbolic name for each layer within a subsystem is formed by count-

Symbolic name	Description	Geometry	η-coverage	n_{layers}
EMB	EM barrel	cylinder	$\lvert\eta\rvert < 1.8$	3
EME	EM end-cap	wheel	$1.5 < \lvert\eta\rvert < 2.5$	3
TileBar	Hadronic barrel	cylinder	$\lvert\eta\rvert < 1.0$	3
TileExt	Hadronic barrel	cylinder	$1.0 < \lvert\eta\rvert < 1.7$	3
HEC	Hadronic end-cap	wheel	$1.5 < \lvert\eta\rvert < 2.5$	4

Table 5.2: the calorimeter sub-systems in ATLAS used for calorimeter muon identification.

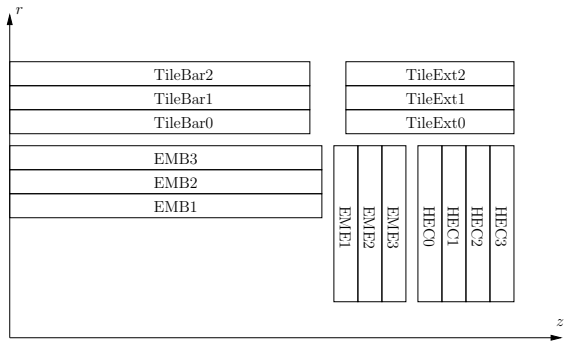

Figure 5.2: schematic illustration of the layout of the calorimeter layers used for muon identification. One quarter of the section with the rz-plane of the ATLAS calorimeter is shown. The figure is not to scale; for correct dimensions consult Section 3.2.3.

ing the number of layers inside-out, starting from zero. For example, the Tile calorimeter consists of layers TileBar0, TileBar1, TileBar2. Since no deposits are collected in the presamplers in front of the EMB and EME layers, the EMB0 and EME0 layers are omitted. In Figure 5.2 a schematic overview of the different layers is shown. A central track that passes through all the EMB and TileBar layers will hit the following layers: EMB1, EMB2, EMB3, TileBar0, TileBar1, TileBar2. A very forward track will hit the layers EME1, EME2, EME3, HEC0, HEC1, HEC2, HEC3. For tracks in the transition region more complicated sequences can be possible: EMB1, EME1, EME2, EME3, HEC0, TileExt0, TileExt1.

Since detailed extrapolation is CPU expensive, it would have been very time consuming to attempt an extrapolation to each layer. Instead the layers that are being hit are determined beforehand. As indicated at the end of the previous paragraph, the combination of crossed layers can be quite complex. In order to cover all cases, a CPU inexpensive straight-line extrapolation is attempted to every layer.

A layer in the calorimeter can be expressed as a cylinder both for the wheel- and cylinder-type geometries. However, determining if a layer will be hit by the track is done differently depending on the geometry. For cylinder type geometry, a straight-line extrapolation is performed to a cylindrical surface, while for end-cap layers the extrapolation attempts to reach a ring shaped surface.

Suppose the track has an origin at (x_0, y_0, z_0) and the direction of the momentum is specified in polar coordinates (θ, ϕ). Straight-line extrapolation to a cylindrical surface with radius r located axially in $(z_{\min}, z_{\max})$ is done by solving l from the equation

$$r^2 = (x_0 + l\cos(\phi)\sin(\theta))^2 + (y_0 + l\sin(\phi)\sin(\theta))^2.$$

The position along z then determines if this cylindrical surface is hit:

$$z = z_0 + l\cos(\theta) \quad \in \quad (z_{\min}, z_{\max}).$$

In the forward region, rings are constructed with inner radius $r_{\min}$ and outer radius $r_{\max}$. Let the ring be positioned at z, then the following condition needs to be satisfied

$$\begin{aligned} l &= \frac{z_{\text{ring}} - z_0}{\cos\theta}, \\ r^2 &= (x_0 + l\sin\theta\cos\phi)^2 + (y_0 + l\sin\theta\sin\phi)^2 \quad \in \quad (r^2_{\min}, r^2_{\max}) \end{aligned}$$

in order to hit this layer.

Using this list of calorimeter layers that will be hit, detailed extrapolation to the layers will be done. The detailed extrapolation uses accurate magnetic field maps and estimates the energy lost in the material by the muon. Due to the accurate magnetic field description the ϕ-coordinate is correctly estimated. This is a crucial feature for finding the correct cells crossed by the particle. Since the extrapolation is a relatively CPU expensive operation, processing time is saved by continuously caching the track parameters and initiating the next extrapolation starting from the previous one. The list of layers that are hit are therefore ordered in distance to the track's origin.

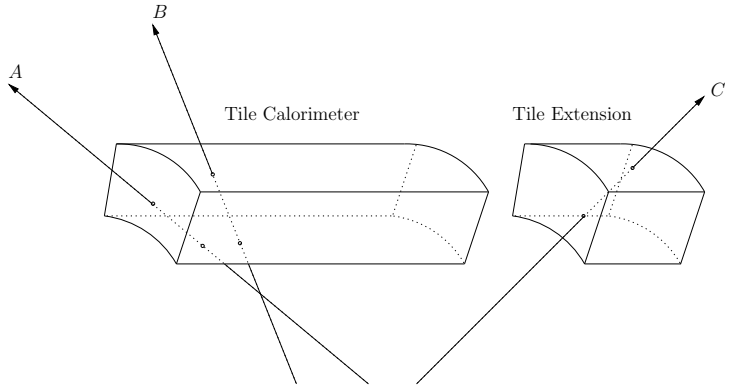

Figure 5.3: possible ways of a track penetrating a calorimeter layer.

For every calorimeter layer, which is represented by a cylindrical shell in the barrel, the track position at the entrance and at the exit of the layer are determined. In Figure 5.3 three different configurations, case A, B and C, of tracks hitting a calorimeter layer are shown. The track is extrapolated to the cylinder representing the inner surface of the calorimeter layer. For case C the track misses the surface and the extrapolation is initiated to its ring-shaped boundary. In order to save CPU time, the extrapolation is actually first performed to a cylinder of infinite length, followed by a check if the track hits the calorimeter surface. If that is not the case, a new extrapolation is initiated to the ring-shaped boundary starting from the track position at the infinite-length cylinder. If this extrapolation fails, the track has missed the layer completely. This rarely happens since the linear extrapolation approximates the accurate extrapolation very well in the rz-plane. The procedure to deal with all these configurations is summarised in the flowchart in Figure 5.4.

When the extrapolation succeeds the track parameters at the exit are determined. This procedure is similar to the procedure for determining the entrance parameters; also here the cylindrical surface is attempted first. If the parameters are outside the cylinder bounds, a new extrapolation is initiated to the ring shaped outer side.

For the end-cap layers, the strategy followed is similar, but the cylinder/ring order is switched: instead of extrapolating to an infinite length cylinder, a disk with an infinite radius is used. It is then checked to hit the ring representing the calorimeter boundary. If this fails, it is attempted to extrapolate to a cylinder

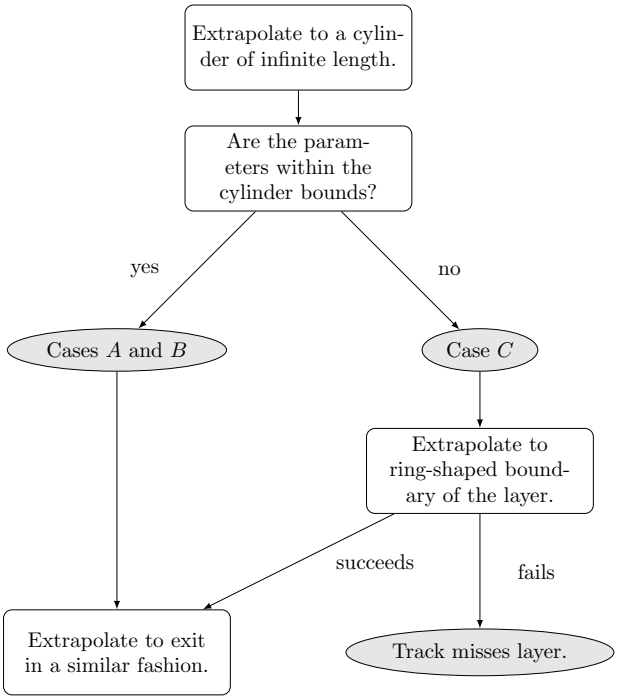

Figure 5.4: flowchart of the extrapolation to the layers in the barrel (see text and Figure 5.3).

with a radius equal to the inner radius of the layer.

The cells that have been crossed can now be collected after having determined the points where the track enters and leaves all calorimeter layers. There are two different methods due to the different cell structures found in the calorimeters.

For the calorimeters based on the LAr technology, the cell structure is projective, which means that one cell can be uniquely identified for a coordinate in (η, ϕ). In the LAr calorimeter, the cell that matches the (η, ϕ)-coordinate at entrance is collected. If the cell that matches the (η, ϕ)-coordinate at the exit is different, this cell is collected as well and the deposited energies are summed. Usually one cell is collected. However, tracks can cross boundaries in ϕ due to the bending in the magnetic field. Tracks that are displaced along the beam line with respect to the ATLAS centre, such as the ones encountered in cosmics, can cross boundaries in η as well.

The hadronic barrel calorimeters (TileBar and TileExt) do not have a projective cell structure, as can be seen from Figure 3.8. The A, B and D cell structures are rectangular while the BC cell structure has been made semi-projective by stacking two rectangles on top of each other, shifting the upper one to larger values of $|z|$. In Figure 5.5, the definitions of the cell dimensions are shown. In the ϕ-direction, the width of the cell is given by $\phi^{\min}$ and $\phi^{\max}$. Let the track's entrance parameters be given by $(\phi_0^{\text{trk}}, z_0^{\text{trk}})$ and the track's exit parameters are given by $(\phi_1^{\text{trk}}, z_1^{\text{trk}})$, then a cell is collected if it satisfies the following conditions:

hit at entrance: if $\phi^{\min} < \phi_0^{\text{trk}} < \phi^{\max}$ and $z^{\min} < z_0^{\text{trk}} < z^{\max}$ is satisfied;

hit at exit: if $\phi^{\min} < \phi_1^{\text{trk}} < \phi^{\max}$ and $z^{\min} < z_1^{\text{trk}} < z^{\max}$ is satisfied;

crossed: if $\phi^{\min} < \phi_0^{\text{trk}} < \phi^{\max}$ and $\phi^{\min} < \phi_1^{\text{trk}} < \phi^{\max}$ is satisfied in combination with $z_0^{\text{trk}} < z_0^{\min}$ and $z_1^{\text{trk}} > z_1^{\max}$ (see Figure 5.6).

5.1.3 CaloMuonTag

The `CaloMuonTag` algorithm is a cut-based approach to identification of muons. There are three categories of cuts:

signal requirements: these are lower bounds on the measured energies in the different layers. Since the muon is not absorbed in the calorimeter[2], the

[2]This of course presumes that its momentum is large enough; a muon crossing the central calorimeter has an energy loss of approximately 3 GeV.

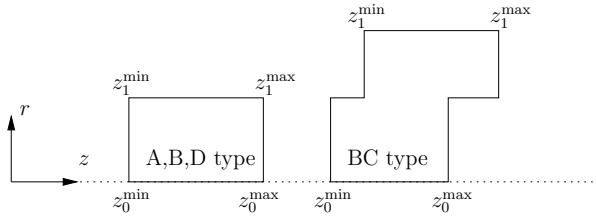

Figure 5.5: Tile-cell dimensions.

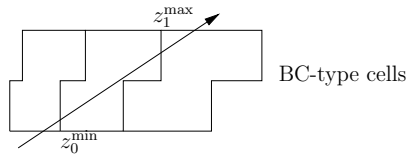

Figure 5.6: example of a track crossing cells in the Tile-calorimeter. Although only illustrated for BC cells, cell crossing can also occur for the A,B and D cells.

deposits extend into the last layer. For low-p_{T} tracks the discriminating power mainly comes from these cuts, since low-p_{T} hadrons often get absorbed before reaching the last layer;

vetoes: these are upper bounds on the measured energies. These cuts are very powerful for high-p_{T} tracks, since a hadron typically will shower and produce higher energy deposits. There are also veto-cuts in the electromagnetic calorimeter providing discrimination between electrons and muons;

compatibility cuts: these are cuts on the difference between the measured deposit and the calculated energy loss of the muon traversing the material: $\Delta E = E_{\mathrm{param}} - E_{\mathrm{measured}}$. The advantage of these cuts over the cuts above is that these cuts take into account the path-length of the material traversed.

For low-p_{T} tracks, the signal requirement in the last layer is a very powerful tool for tagging the muon. However, some efficiency is lost due to these requirements. At high p_{T}, the vetoes provide a powerful rejection against electrons and hadrons. In addition, the signal requirements are less effective, since the hadron showers extend deeper into the calorimeter. For this reason, the cuts are made p_{T}-dependent.

In Table 5.3 the actual cut-values are displayed. For low p_{T} the windows are narrow while for high p_{T} mainly the vetoes are working. The low-p_{T} region is defined as $p_{\mathrm{T}} < 15\,\mathrm{GeV}$, while the high-$p_{\mathrm{T}}$ region is defined as $p_{\mathrm{T}} > 35\,\mathrm{GeV}$. In between the cuts are linearly interpolated. The cut values are found through an optimisation procedure on a simulated data set.

In the high-p_{T} region the signal cuts are effectively disabled. Due to calorimetric noise, which sometimes causes the collected cell energies to be negative, the signal requirements for high p_{T} are negative. For the TileBar1 and TileExt2 layers, the cut value is actually much lower than the noise in those layers. Due to the linear extrapolation this actually means that the signal requirement is effectively dropped at a transverse momentum lower than 35 GeV.

The `CaloMuonTag` algorithm provides a tag level for each track. The tag level depends on the number of layers through which the particles passed, which depends only on η for particles produced at the centre of the detector. If it has reached the last hadronic layer (i.e. TileBar2, TileExt2 or HEC3) and passes all cuts the tag level 1 is assigned. If the particle does not pass through the last layer, but does pass through the one-to-last layer the tag level is 2. Tag level 3 is only assigned to a very small region where only one hadronic layer in the barrel or only two hadronic layers in the end-cap are collected.

5.1.4 CaloLikelihoodRatio

The `CaloLikelihoodRatio` algorithm uses a likelihood ratio that is built in the following way:

$$\mathcal{R} \;=\; \frac{\mathcal{L}_{\mu}}{\mathcal{L}_{\mu} + \mathcal{L}_{\mathrm{bkg}}}, \tag{5.2}$$

where $\mathcal{L}_{\mu}$ and $\mathcal{L}_{\mathrm{bkg}}$ are the likelihoods for respectively muons and non-muons. They are defined as follows:

$$\begin{array}{rcl} \mathcal{L}_{\mu} & = & \prod_i P_i(E_i|\mathrm{muon}), \\ \mathcal{L}_{\mathrm{bkg}} & = & \prod_i P_i(E_i|\mathrm{pion}), \end{array} \tag{5.3}$$

where $P_i(E_i|\mathrm{muon})$ is the probability that a muon has created a deposit E_i in layer i and $P_i(E_i|\mathrm{pion})$ is the probability that a non-muon (pion/hadron) track has created a deposit E_i in layer i.

Note that the definition of the likelihood ratio in Eq. 5.2 is slightly different from the usual one:

$$\mathrm{LR} \;=\; \frac{\mathcal{L}_{\mathrm{sig}}}{\mathcal{L}_{\mathrm{bkg}}}. \tag{5.4}$$

Cut	Low-p_{T} cut-value (MeV)	High-p_{T} cut-value (MeV)
EMB1 Veto	200	600
EMB2 Veto	500	1000
EMB3 Veto	300	400
EME1 Veto	900	900
EME2 Veto	1900	1900
EME3 Veto	900	900
TileBar0 Signal	80	−200
TileBar1 Signal	500	−1000
TileBar2 Signal	80	−200
TileBar0 Veto	2500	7000
TileBar1 Veto	2500	7000
TileBar2 Veto	2500	7000
TileExt0 Signal	0	−300
TileExt1 Signal	500	−400
TileExt2 Signal	250	−1000
TileExt0 Veto	2000	6000
TileExt1 Veto	2500	8000
TileExt2 Veto	2500	8000
HEC0 Signal	0	−1000
HEC1 Signal	0	−1000
HEC2 Signal	100	−1000
HEC3 Signal	250	−1000
HEC0 Veto	1500	8000
HEC1 Veto	2000	8000
HEC2 Veto	2000	8000
HEC3 Veto	2000	8000
TileBar0 Compatible	−300	−1000
TileBar1 Compatible	−550	−1200
TileBar2 Compatible	−300	−1000
TileExt0 Compatible	−500	−1000
TileExt1 Compatible	−500	−1200
TileExt2 Compatible	−500	−1500

Table 5.3: default cut values for the `CaloMuonTag` algorithm.

p_T binning		η binning	
Name	Region	Name	Region
Low p_T	$p_T \leq 11\,\text{GeV}$	Central	$\lvert\eta\rvert \leq 1.4$
Medium p_T	$11\,\text{GeV} < p_T < 51\,\text{GeV}$	Transition	$1.4 < \lvert\eta\rvert < 1.6$
High p_T	$p_T \geq 51\,\text{GeV}$	Forward	$\lvert\eta\rvert \geq 1.6$

Table 5.4: p_T and η binning of the cached distributions in the likelihood algorithm.

which is unity if the background and signal are equally likely. However, Eq. 5.2 can be rewritten in terms of the usual LR through

$$\mathcal{R} = \frac{1}{1 + \text{LR}^{-1}}, \tag{5.5}$$

which has its values in the domain $(0, 1)$.

The probability distributions from Eq. 5.3 are derived from single-particle simulated samples in three different regions in η and in three different regions in p_T as displayed in Table 5.4. The muon pdfs are constructed using single muon samples, while the background pdfs are constructed using single pion samples. In the likelihood algorithm the cluster that has the best match to the track is also used for additional information. As shown in Figure 5.7, the $E_{\text{cluster}}/E_{\text{track}}$ distributions have a good separation between muons and background.

5.2 Performance

5.2.1 Cosmic Calorimeter Muons

The Earth is hit by high energy cosmic particles producing showers in the atmosphere. In these showers large quantities of high-p_T muons are created. If these muons have a high enough energy, they can penetrate the soil and reach the detector. These cosmic particles are a very clean muon source since nearly all other particles will be absorbed before reaching the detector. The soil in this case works like a muon filter in a similar fashion as the calorimeter subsystems.

When the LHC was undergoing commissioning (and during its repair period, see Section 3.1) these cosmic muons were used extensively for commissioning and calibration of the detector subsystems and the reconstruction software. This was also done for the calorimeter identified muons. It also served as a test whether

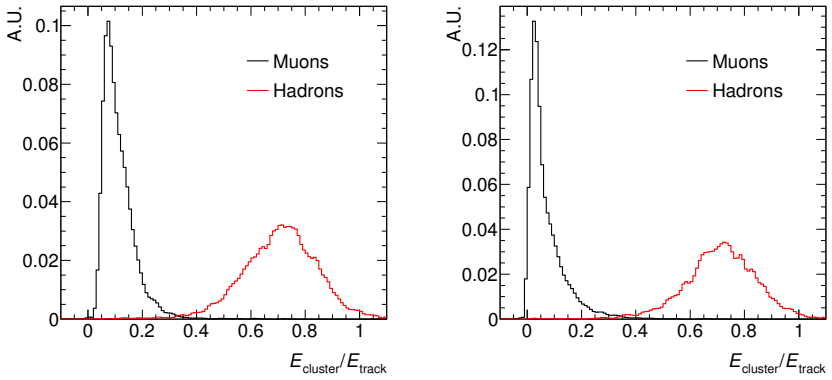

(a) (b)

Figure 5.7: the ratio of the energy deposited in the cluster with respect to the energy of the track for medium p_T tracks in the central region (a) and the forward region (b).

the track extrapolation was working as expected. Since tracks from cosmic muons do not necessarily originate from the beam-spot centre in ATLAS they are generally harder to extrapolate well.

The plots in this section are made from one cosmic run in October 2008.[3] Tracks were selected to have a transverse momentum in excess of 5 GeV, in addition to the ordinary track selection cuts. In Figure 5.8, the η, ϕ and p_T distributions are displayed in histogram style for the tracks that were selected, while the tracks that are tagged are displayed by the data points. From the η distribution one can see a large peak which corresponds to a shaft directly above ATLAS that was used for lowering the detector equipment. One can see from the p_T distribution that the tagging efficiency becomes higher at high p_T.

A fake-rate test is also attempted using these cosmic muons. A quintuple of fakes is created by rotating the original by $\pi/6$, $2\pi/6$, ... The η values of the track are reversed. From this quintuple, the third element is thrown away

[3] At that time, the p_T-dependent tagging was not yet developed and the `CaloMuonTag` algorithm was tuned differently. Nonetheless, the results from this analysis have been included in this thesis since they provide insights whether the extrapolation is functioning correctly. When writing this thesis, the extrapolation methodology has not changed from the one used in this analysis on cosmics presented here.

since it might coincide with the incoming muon for central η and high p_{T}[4]. For every track four extrapolations are done and the number of tagged muons are counted. From this analysis, the probability that such a fake track is tagged is computed to be less than 3 ‰. It should be noted that this is not equivalent to the fake rate per track since a correctly reconstructed track will leave deposits and is able to trigger vetoes. It does however give an idea of the fake rate for incorrectly reconstructed tracks.

5.2.2 Validation on Data

In this section the deposited energies in data are compared to the simulated values. After requiring a muon trigger, the data is still dominated by multi-jet events with a non-isolated muon from hadron decay. Since the calorimeter muon identification algorithm is not optimised for finding these muons, it is chosen to specifically select Z events.

The data set considered is a subset of the full 2010 data set.[5] It corresponds to an integrated luminosity of $19.08\,\mathrm{pb}^{-1}$, which accounts for requiring good data quality (see Section 6.1). A single muon trigger at the event-filter level is required to pass a threshold of 13 GeV. A muon is selected when the cuts as displayed in Table 5.5 are passed. In addition, Z events are selected by requiring exactly two muons of opposite charge, separated by an angle $\Delta\phi > 2$. One of the two calorimeter muons is required to loosely coincide with the trigger by applying a $|\eta| < 2.4$ trigger-acceptance cut. Identical event selection is performed for a number of simulated samples. The `Pythia` [16] generator is used to generate the electroweak channels: $Z \to \mu\mu$, $Z \to \tau\tau$, $W \to \mu\nu_\mu$, $W \to \tau\nu_\tau$ as well as the QCD processes $b\bar{b}$ and $c\bar{c}$. The `Powheg` [69] generator is used to generate the $t\bar{t}$ process.

In Figures 5.9-5.13 the distributions of the collected deposits in data are compared to the simulated deposits. The measured deposits are well represented by the simulation, which is important in order to have reliable performance predictions. Even the peaks at zero are well represented. These peaks are caused by dead cells, and are visible in EMB2, EME2, and the Tile calorimeters. The agreement in the electromagnetic end-cap is slightly off. Since the main purpose of including the electromagnetic calorimeters is to reject electrons and since the EMB electron veto cuts are very loose (see Table 5.3), this does not have a large influence on the performance.

[4] At low p_{T} the track will bend away in the magnetic field of the inner detector.
[5] It is actually the last pp data-taking period of 2010, called 'period I'.

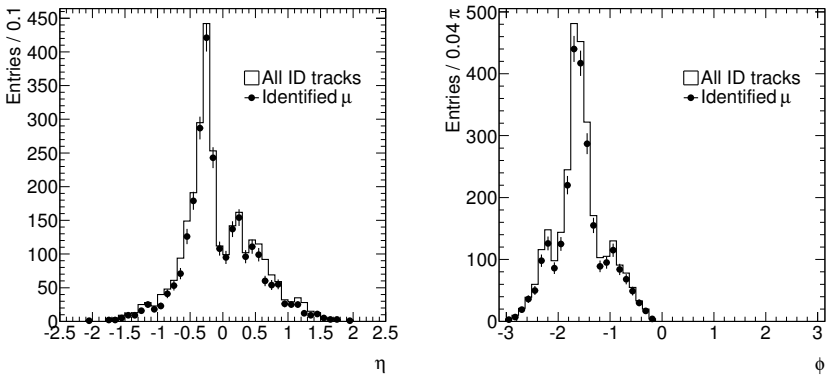

Figure 5.8: calorimeter muon-identification performance on cosmics.

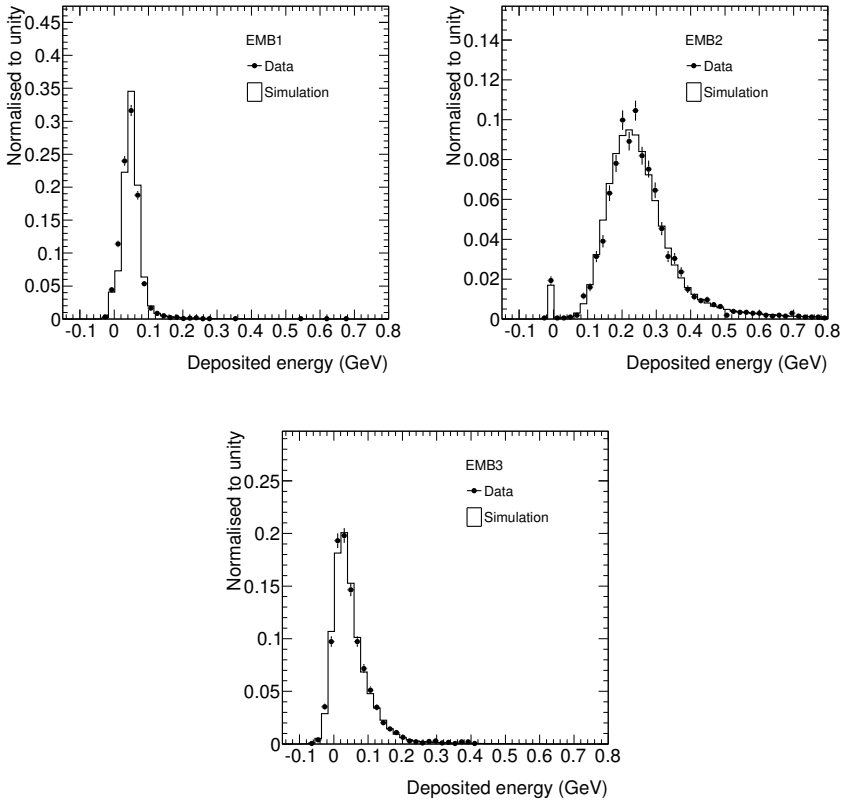

Figure 5.9: validation of the simulated deposited energies in the barrel electromagnetic calorimeter.

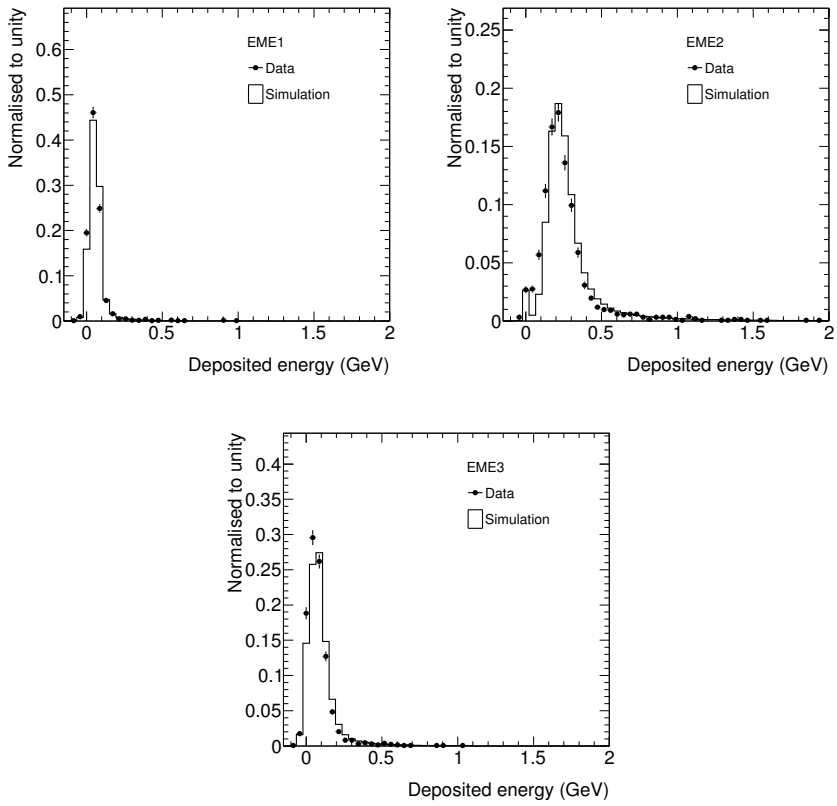

Figure 5.10: validation of the simulated deposited energies in the end-cap electromagnetic calorimeter.

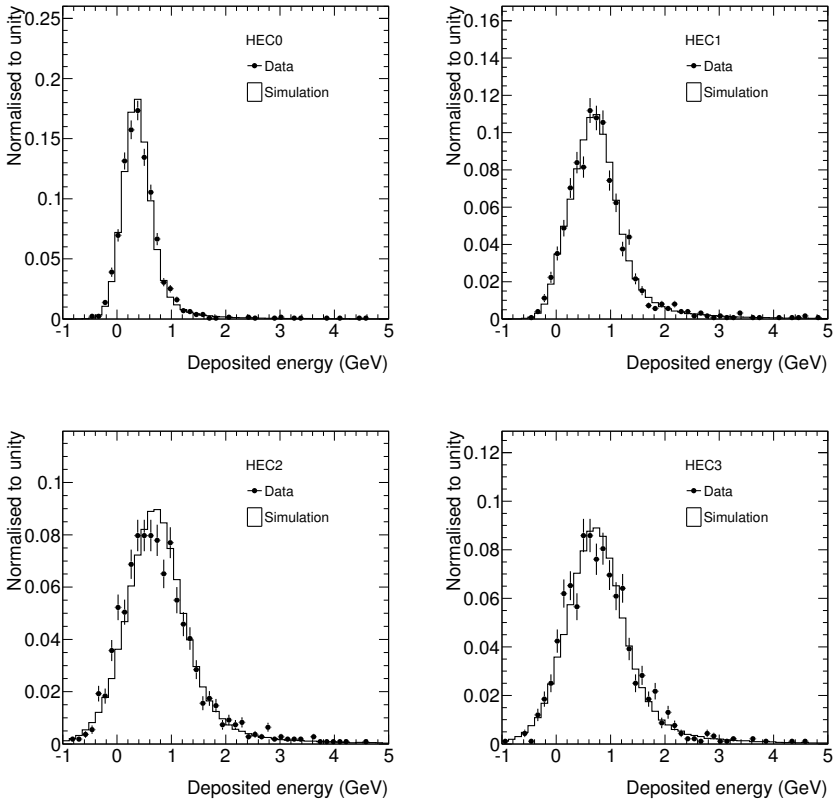

Figure 5.11: validation of the simulated deposited energies in the end-cap hadronic calorimeter.

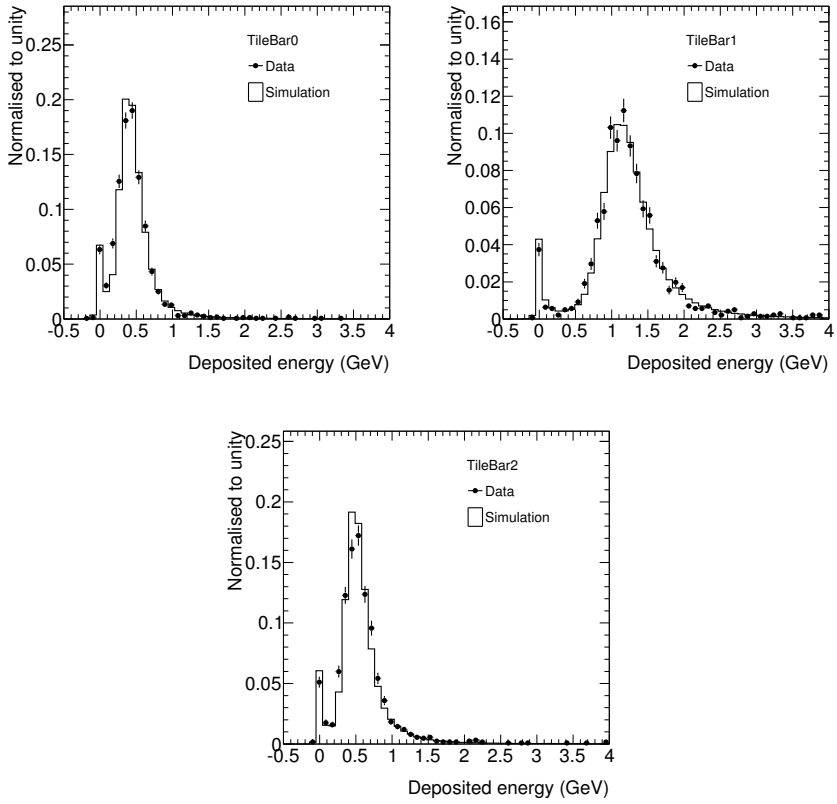

Figure 5.12: validation of the simulated deposited energies in the barrel hadronic calorimeter.

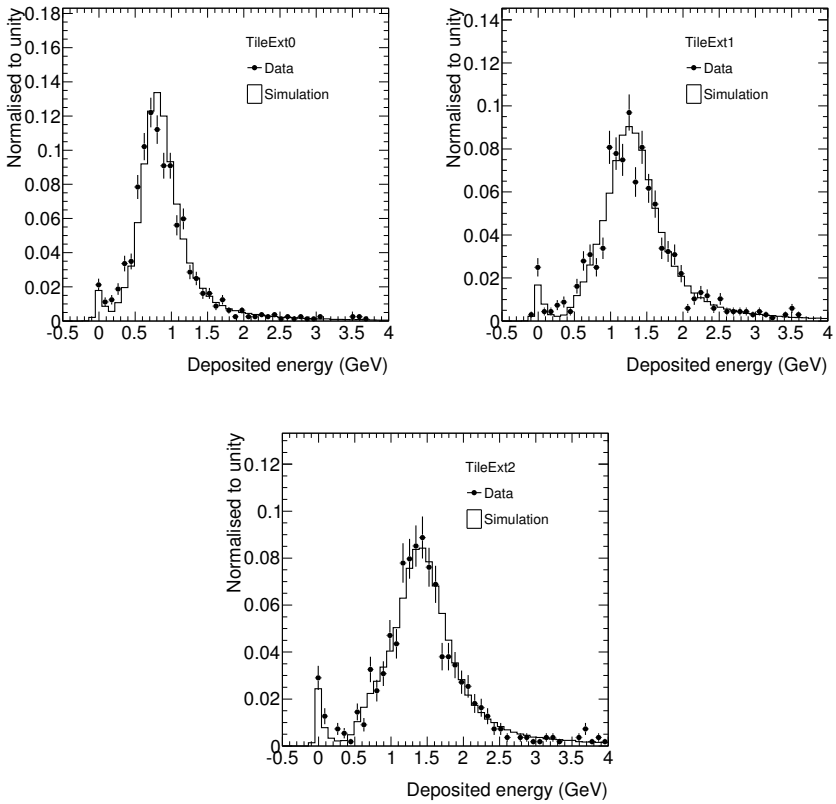

Figure 5.13: validation of the simulated deposited energies in the barrel extended hadronic calorimeter.

Algorithm	Calorimeter muons, found by `CaloMuonTag` and `CaloLikelihoodRatio`
Kinematics	$p_{\mathrm{T}} > 20\,\mathrm{GeV}$, $\lvert\eta\rvert < 2.5$
ID track quality	At least 1 pixel hit and at least 6 SCT hits
TRT hits $\lvert\eta\rvert < 1.9$	Number of hits and outliers should be larger than 5 and the number of outliers should be less than 90 % of the total number of hits and outliers
TRT hits $\lvert\eta\rvert > 1.9$	If the number of hits and outliers is larger than 5, the number of outliers should be less than 90 % of the total number of hits and outliers
Isolation	Relative track isolation $p_{\mathrm{T}}^{\mathrm{iso}}(\Delta R \leq 0.4)/p_{\mathrm{T}}^{\mu} < 0.2$

Table 5.5: selection cuts for calorimeter muons.

5.2.3 Simulated Performance

In this section the performance of `CaloTrkMuId` in terms of efficiency and fake rate will be estimated from simulation. The analysis is done on a sample of $Z \to \mu\mu$ and a sample of $t\bar{t}$ events.

Again the selection of calorimeter muons is the same as given in Table 5.5. No trigger is required for the Monte Carlo study. This is needed to study the calorimeter muons around $|\eta| < 0.1$ since also the trigger suffers from the acceptance gap at $|\eta| < 0.1$.

A correctly reconstructed muon is well-defined in simulated data. During simulation it is archived which particle produced which detector hit. A fitted track therefore has an accurate truth-particle match. Only very few tracks have no truth match assigned to them. Most of these have an ambiguous truth match, which can be caused by a track which has joined hits of different truth particles.

The efficiency is measured by dividing the number of correctly reconstructed calorimeter muons by the total number of generated muons in the event. Since `CaloTrkMuId` is not aiming at reconstructing non-prompt muons found in or near jets, the truth muons are required not to originate from a hadron decay. This cut is applied both at the truth level of the track-match, as well as the generated muons in the event. No cuts are placed on the muons in order to determine the fake rate.

In Figure 5.14, the efficiency for the $Z \to \mu\mu$ sample is shown in η and p_{T}. The efficiency dip around $|\eta| < 0.1$ is caused by a small gap in the TRT region. In Figure 5.15, the fake rate is shown as function of p_{T} and η. Due to a more

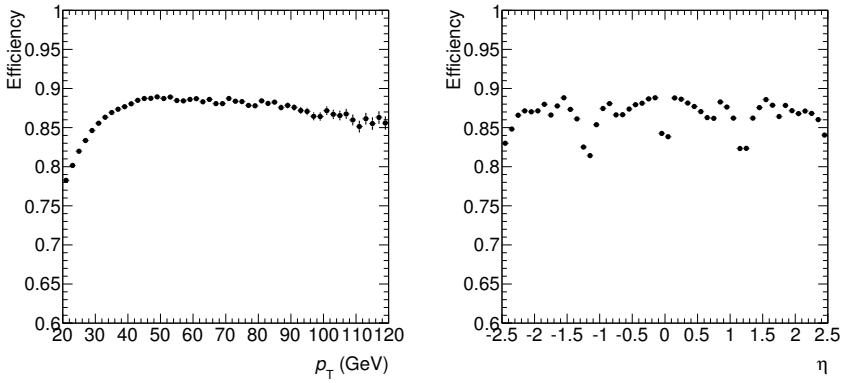

Figure 5.14: the simulated efficiencies for muons in $Z \to \mu\mu$ events as function of p_{T} and η.

difficult tagging in the noisy HEC environment and due to the topology of the $Z \to \mu\mu$ sample, which has very little high-p_{T} hadronic tracks in the forward region, the fake rate is peaking in the forward region.

The $t\bar{t}$ simulation provides a more challenging sample. In Figure 5.16, the efficiency is shown. A drop of approximately 5 % can be observed compared to the $Z \to \mu\mu$ efficiency. Although any muon from b hadron decay is not counted in the efficiency calculation, the more busy $t\bar{t}$ events cause some prompt muons to be in the vicinity of jets. Since tagging is unreliable there, these muons are removed by the energy isolation cuts. The fake rate in Figure 5.17 is higher than the one found in the $Z \to \mu\mu$ sample (notice the different scales). Again this is caused by the more busy environment of $t\bar{t}$ events.

5.2.4 Performance on Data

On data the performance is measured by studying muons simultaneously reconstructed by the muon spectrometer and by the calorimeter muon identification algorithms. Again the same subset of the 2010 data, corresponding to $19.08\,\mathrm{pb}^{-1}$, has been used to study this. A muon trigger at event level with 13 GeV is required and each calorimeter muon is required to pass the cuts displayed in Table 5.5.

Every event containing at least one calorimeter muon or at least one com-

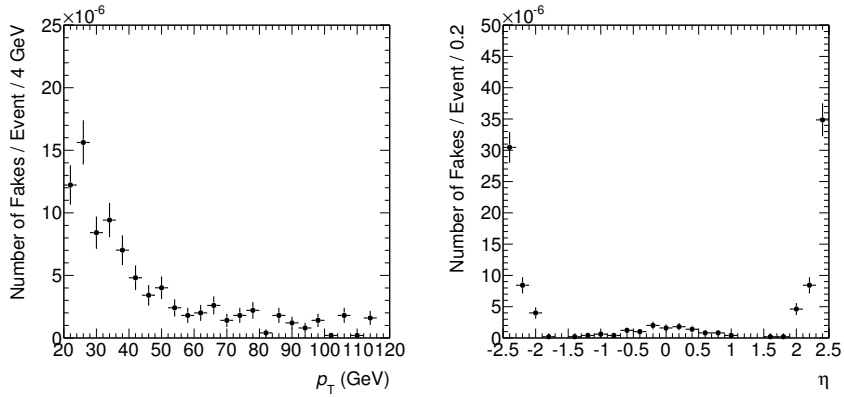

Figure 5.15: the simulated fake rate for $Z \to \mu\mu$ events as function of p_{T} and η.

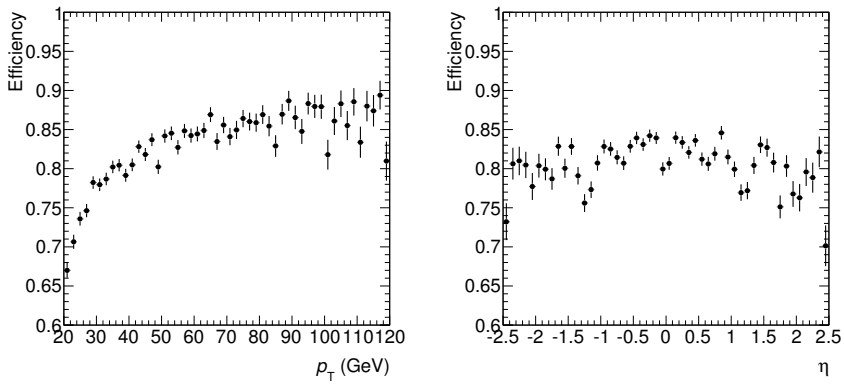

Figure 5.16: the simulated efficiency for prompt muons in $t\bar{t}$ events as function of p_{T} and η.

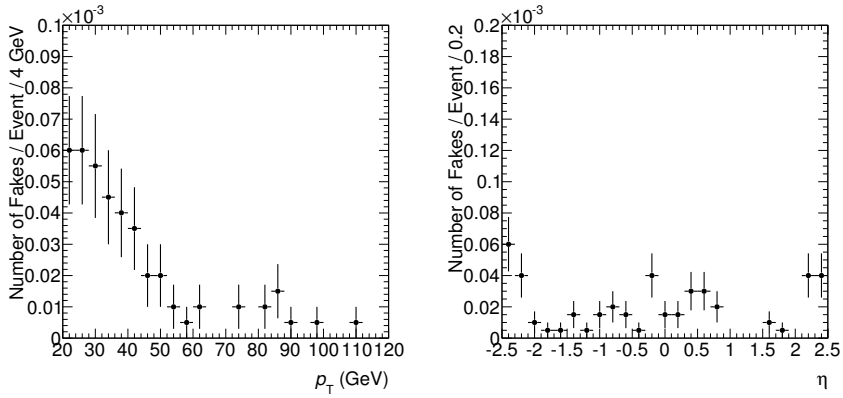

Figure 5.17: the simulated fake rate for $t\bar{t}$ events as function of p_{T} and η.

bined muon is kept. The combined muons are required to be simultaneously found by also the calorimeter muons by requiring $\Delta R = \sqrt{\Delta\eta^2 + \Delta\phi^2} < 0.01$. For the calculation of the distances $\Delta\eta$ and $\Delta\phi$ the inner detector part of the track of the combined muon is used. The region $|\eta| < 0.1$ is excluded since the coverage of the muon spectrometer is very limited there. In order to select prompt muons the following additional cuts are applied:

- relative isolation: $p_{\mathrm{T}}^{\mathrm{iso}}(\Delta R \leq 0.4)/p_{\mathrm{T}} < 0.1$;
- impact parameter: $|d_0| < 0.1\,\mathrm{mm}$.

In Figure 5.18 the fraction of combined muons matched to calorimeter muons is shown. This is an estimator of the calorimeter-muon efficiency. It should be noticed that this estimator is slightly biased since the collection of combined muons does contain a small fraction of tracks misidentified as muons.

In Figure 5.19 the distributions in η and p_{T} of the calorimeter muons that are not matched to a combined muon are shown. This is an estimator of the fake rate in data, which in turn is biased due to the fact that combined muon reconstruction does not have a 100 % efficiency.

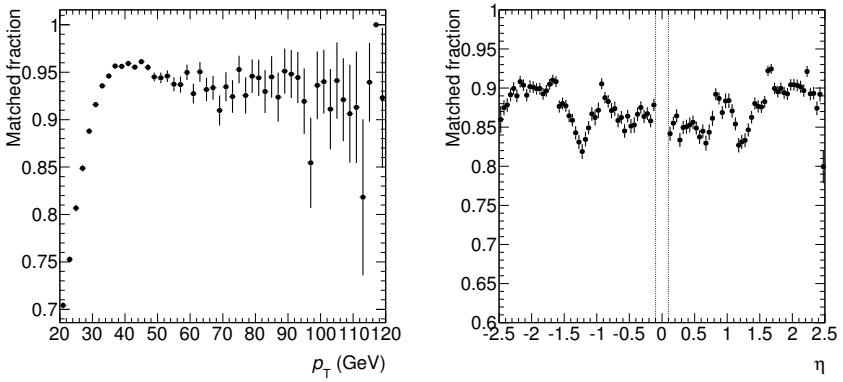

Figure 5.18: the performance of calorimeter muon identification relative to combined-muon performance in p_T and η.

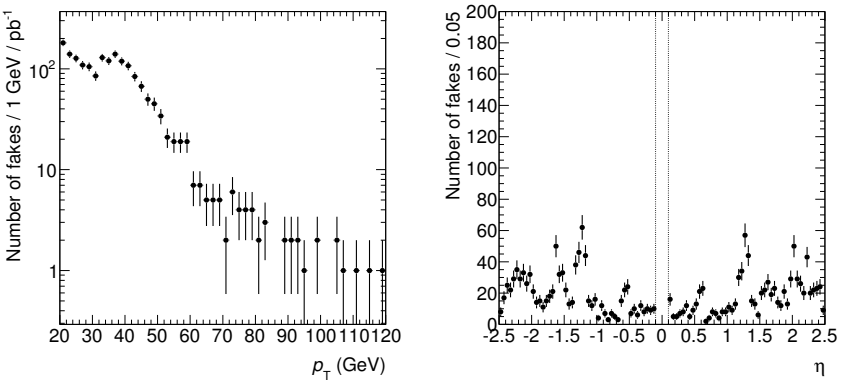

Figure 5.19: the number of calorimeter muons not matched to combined muons as function of p_T and η.

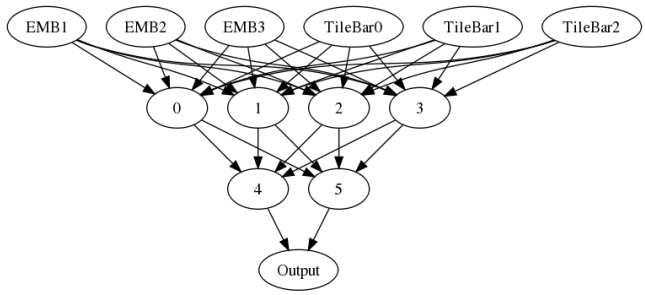

Figure 5.20: the neural network used for muon tagging.

5.3 Outlook

The deposited energies in each layer are heavily correlated. A muon leaves a trail of moderate energies throughout the calorimeter, while the background consists of several signal shapes. Low-energy hadrons leave moderate deposits in the first layers, but are not likely to leave any substantial deposits in the last layers. High energy hadrons leave large deposits which can reach the last layer of the hadronic calorimeter. The current tagging algorithms do not take into account the correlations between the layers. In this section, the possibility of using a neural network for tagging muons in the calorimeter is studied.

The type of neural network used is a multilayer perceptron (MLP). An MLP neural network consists of an input layer, one or more hidden layers and an output layer. Each layer has a number of nodes/neurons which are connected to the nodes of the next layer. The MLP used here is strictly feed-forward, which means that there are no connections from a node to another node that is in a layer closer to the input layer. In Figure 5.20 the actual neural network used for this analysis is shown.

Each link/arrow in Figure 5.20 has a weight, w_{i,j_i}, where i denotes the layer and j_i is the node index in that layer. Each node in the neural network has an activation function of the form

$$f(x) \quad = \quad \frac{1}{1+e^{-x}}, \tag{5.6}$$

which looks like a smoothed/continuous step-function. The value x is the

weighted sum of all the links inputting to that node:

$$x_{i+1,j_{i+1}} = \sum_{j_i} w_{i,j_i} \cdot f(x_{i,j_i}). \tag{5.7}$$

The value of the output node is a function of the values of the input nodes, $\mathbf{x}_0$ and the weights. Training of the neural network proceeds via the minimisation of the error function ϵ:

$$\epsilon = \sum \mathbb{E}\Big[(\mathrm{NN}(\mathbf{x}_0) - y)^2\Big], \tag{5.8}$$

where $\mathrm{NN}(\mathbf{x}_0)$ is the output of the neural network and y is the desired output (classification). The sum is taken over all input vectors in the data set.

The `root` package [70] offers an implementation of a multilayer perceptron in the class `TMultiLayerPerceptron`. It uses the Broyden-Fletcher-Goldfarb-Shanno (BFGS) method [71] in order to minimise the error function. A $p_{\mathrm{T}} > 10\,\mathrm{GeV}$ cut has been applied to the tracks that are preselected using the selection criteria listed in Section 5.1.1. Since there are many different configurations of cells that are collected, the neural network has been limited to the barrel region and it is required that the number of collected cells is equal to six. This means that there is only one configuration of cells possible: EMB1, EMB2, EMB3, TileBar0, TileBar1, TileBar2. The values on the six input nodes in Figure 5.20 are divided by the parameterised energy loss in that layer. This gives signal distributions peaking at a ratio of one, with a slightly extended tail to higher values due to Landau fluctuations. The desired value on the output node is one when it is a muon and zero if it is not a muon. A sample of 20000 $t\bar{t}$ events have been used for training. The $t\bar{t}$ process is chosen since it is a difficult sample due to the high number of high-p_{T} tracks.

In Figure 5.21 the minimisation of the error function is shown as function of the number of training iterations, called epochs. The solid line indicates the performance on the training sample, while the dashed line indicates the performance on an independent sample. This independent sample is called the test sample and large differences in performance between testing and training sample indicate *overtraining*. Overtraining means that the neural network becomes sensitive to statistical fluctuations in the training sample, which do not represent general features. Overtraining is more likely to occur for complicated neural networks with a lot of weights. The complexity of the neural network has been chosen by taking into account the overtraining and the sensitivity. Although from Figure 5.21 a slight overtraining is observed, the performance on the test sample is still enhanced (i.e. it is not increasing).

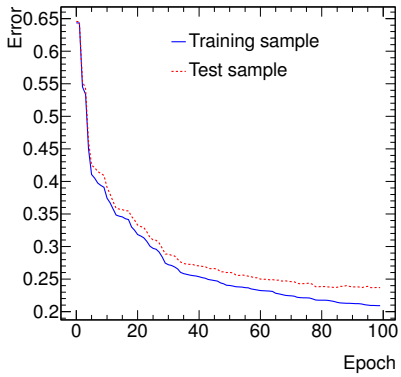

Figure 5.21: neural-network training curves.

The performance is assessed in another independent test sample of 40000 $t\bar{t}$ events. The neural-network output nicely separates the tracks with a truth-muon match and the tracks that do not have muon match. This is shown in Figure 5.22(a). In Figure 5.22(b), the efficiency versus the background rejection is shown. The best possible curve is a square curve, which indicates that it is possible to reject all background without losing efficiency.

The performance of the neural network is also assessed on data. Truth-muon matching is approximated by matching to combined muons in the same way as it is done in Section 5.2.4. The 20000 $t\bar{t}$ events are kept as training sample. The results on data are shown in Figure 5.23. Again the $|\eta| < 0.1$ region where the combined muon reconstruction suffers from the acceptance gap of the muon spectrometer has been cut out. It seems to perform worse than the Monte Carlo training sample. It is suspected that this is due large fraction of non-isolated muons from hadron decays in the data sample, which are generally harder to reconstruct in the calorimeter.

In order to assess the dependence of the performance on possible differences due to mismodelling of the simulated input distributions and their correlations, the neural network has been trained on data and tested on the $t\bar{t}$ sample. The fraction of prompt muons in the data sample can be enlarged by requiring that energy isolation relative the to transverse momentum is smaller than 0.1. If this requirement is dropped, the sensitivity of the neural network is compromised because the deposits of close-by tracks mix and obscure the muon signal in the calorimeter. The performance that can be obtained on the $t\bar{t}$ sample by training

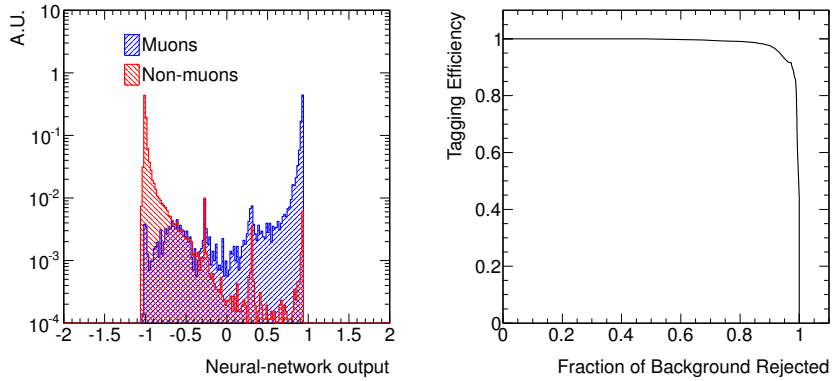

Figure 5.22: neural-network output (a) and the corresponding performance curve (b) on a simulated sample of $t\bar{t}$ events.

on data with these strict isolation requirements is shown in Figure 5.24.

The application of a neural network for calorimeter muon identification has been researched only recently. Some research still needs to be done in order to successfully include it in the baseline muon reconstruction. At this point the neural network is only applied to the barrel region where the configuration of cells is always the same. Extending it to the full η-acceptance of the inner detector would require a large training sample to include all the different cell configurations. Since the deposits are divided by the parameterised energy loss, all distributions, irrespective of which layer or subsystem, have the same profile. Some research needs to be done in how sensitive the neural network is from differences in resolution between the subsystems. It might be possible to group together all tracks that have a certain number of deposits on track.

In addition, the computing performance in terms of CPU (and memory) should be evaluated as well and the `C++` muon object should be extended in order to contain the neural-network output.[6]

[6]The inertia of the massive ATLAS event data model should not be underestimated. The energy required in order to maintain this and ensure compatibility with previous versions is much more than any accelerator can and will produce in the coming decades...

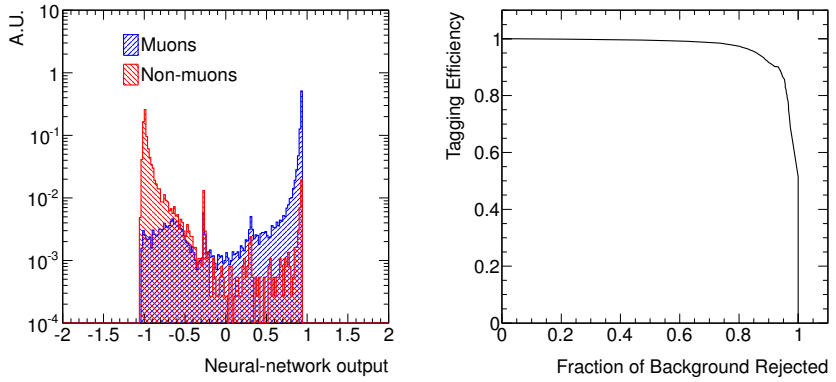

Figure 5.23: neural-network output (a) and the corresponding performance curve (b) on data.

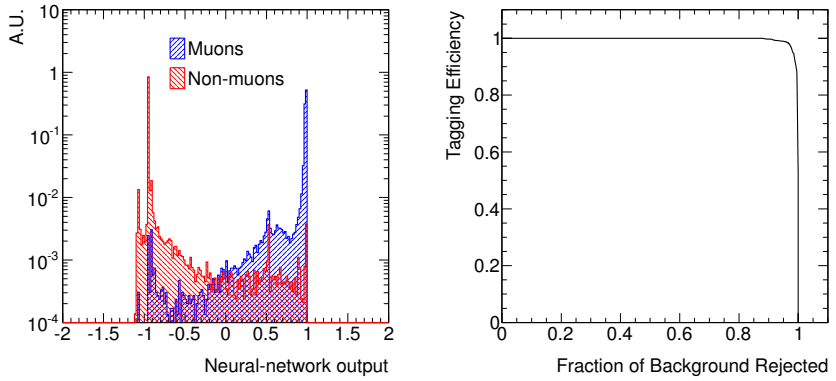

(a) (b)

Figure 5.24: neural-network output (a) and the corresponding performance curve (b) on the $t\bar{t}$ sample. The neural network is trained on isolated tracks in data.

6

W+jets Analysis

In this chapter, the cross section of $W \to \mu\nu_\mu$ is measured as a function of the jet multiplicity. The first part of the analysis deals with the event selection and background subtraction. The jet multiplicity distribution is corrected for detector effects in the second part.

The event selection is detailed in Section 6.1. The simulated signal and background samples are described in Section 6.2. The data-driven estimation of the QCD, or multi-jets background, has been a focal point of my work and is described in full detail in Section 6.3. The subtraction of the other backgrounds including the associated systematic uncertainty is covered in Section 6.4. The correction of the jet multiplicity distribution for detector effects (unfolding) is done in Section 6.5. In Section 6.6, the cross section measurement is finalised and the results are discussed.

The analysis is done within a subgroup within ATLAS. The official ATLAS record can be found here [72].

6.1 Event Selection

A typical $W \to \mu\nu_\mu$ event is characterised by exactly one muon and missing transverse energy due to the neutrino. The following backgrounds have to be considered.

QCD In jets from QCD processes many hadrons are formed. Some of them

have a muonic decay channel. Although the probability of producing a high-p_{T} muon is very low and the bulk is cut away by requiring the muon to be isolated and prompt, multi-jet QCD processes have a very large cross section and form a potentially large background.

Top production Top-quarks decay exclusively via the emission of a W. In events where this W boson decays into a lepton-neutrino pair, the signature of the signal process is imitated. In events that have a high jet multiplicity, $t\bar{t}$ forms a significant background although the cross section is small compared to the W's. Single-top production is also included.

Electroweak backgrounds These consist of $Z \to \mu\mu$, where one muon escapes undetected and in fact also generates the missing transverse energy. The other electroweak backgrounds, $Z \to \tau\tau$ and $W \to \tau\nu_\tau$, are dominated by events where the τ decays into a muon. Also contributing, although with a smaller cross section, is the production of vector boson pairs. This background consists of WW, WZ and ZZ production.

The data set used for this analysis consists of the data taken in 2010. The selection of data starts by requiring that the LHC provides collisions with stable beams. In the detector, the muon, calorimeter and inner-detector subsystems are required to be operational. Furthermore, run-by-run quality assessment of roughly two-minute blocks (lumiblocks) of data-taking is done. This quality assessment is automatised, but supervised. The quality flag, which indicates the performance, is determined by hand, aided by algorithms checking possible deviations from the nominal performance. Only data is selected for which both magnet systems are switched on at full power, the muon trigger is working properly and the muon reconstruction is performing as expected. The jet and missing transverse energy reconstruction is also required to operate nominally.

The entry-point for the event selection is requiring a muon trigger. Since the instantaneous luminosity went up during the year, different triggers are used to avoid using trigger pre-scales (see Section 3.2.5). The triggers used are listed in Table 6.1 together with the integrated-luminosity span over which they were used.

The next step is to select collision candidates, which means that at least one vertex must be reconstructed. Many vertices can be present in one event due to pile-up. The *primary vertex* is defined as the vertex that has the largest sum of transverse momentum squared. In order to reduce background from cosmic muons, the primary vertex is required to be within 200 mm of the beam-spot centre. At least three tracks have to be associated to the primary vertex.

Trigger level	Threshold (GeV)	Integrated luminosity (pb^{-1})
Event filter	10	2.9
Event filter	13	15.3
Event filter (tight)	13	17.3

Table 6.1: muon triggers used for the $W \to \mu\nu_\mu$ analysis.

For the muon candidates, only combined muons of chain 1 are considered (see Section 4.2). They are required to have a transverse momentum that exceeds 20 GeV. In addition the muon has to satisfy the quality cuts listed in Table 6.2.

The *track isolation*, $p_{\mathrm{T}}^{\mathrm{iso}}(\Delta R)$, is calculated using the inner-detector track associated to the combined muon. $p_{\mathrm{T}}^{\mathrm{iso}}(\Delta R)$ is the scalar sum of all the transverse momenta in a cone of size ΔR centred around the muon track. The sum excludes tracks that have a transverse momentum below 1 GeV. Also the transverse momenta of the muon track itself is not included in the sum.

The muon impact parameter with respect to the primary vertex, d_0, is defined in Section 4.1. Since the W boson decays instantaneous, this should be compatible with zero. It is chosen to cut on impact-parameter significance, $d_0/\sigma(d_0)$, since it has a higher efficiency for the signal process and a higher rejection of background processes.

The isolation requirement and the cut on impact parameter significance drastically reduce muons produced from hadron decay in jets and effectively suppress the QCD multi-jet background.

Before the trigger acceptance cut ($|\eta| < 2.4$) is applied, the number of muon candidates within $|\eta| < 2.5$ should be exactly equal to one. This final cut on the number of muons suppresses the $Z \to \mu\mu$ background.

The transverse momentum of the neutrino is estimated by the missing transverse energy. Events are only selected when $E_{\mathrm{T}}^{\mathrm{miss}} > 25\,\mathrm{GeV}$. The missing transverse energy is refined using the identification of the different objects as described in Section 4.4. In order to have a reliable missing transverse energy, the cleaning cuts mentioned in Section 4.4.1 are applied.

Since the neutrino longitudinal momentum is not known, the invariant mass

$$\begin{aligned} M_W^2 &= (p_\mu + p_\nu)^2 \\ &\approx 2|\mathbf{p}_\mu| \cdot |\mathbf{p}_\nu| \cdot \big(1 - \cos(\Delta\psi)\big), \end{aligned} \tag{6.1}$$

cannot be calculated. In the second line the neutrino and muon mass are set to zero and $\Delta\psi$ is the angle between $\mathbf{p}_\mu$ and $\mathbf{p}_\nu$ in the plane spanned by these

Algorithm	Combined muon (chain 1)
Kinematics (1)	$p_{\mathrm{T}} > 20\,\mathrm{GeV}$, $\lvert\eta\rvert < 2.5$
ID track quality	At least 1 pixel hit and at least 6 SCT hits Require hit in inner layer pixel layer if expected Number of holes in pixel and SCT should be less than 2
TRT hits $\lvert\eta\rvert < 1.9$	Number of hits and outliers should be larger than 5 and the number of outliers should be less than 90 % of the total number of hits and outliers
TRT hits $\lvert\eta\rvert > 1.9$	If the number of hits and outliers is larger than 5, the number of outliers should be less than 90 % of the total number of hits and outliers
Isolation	Relative track isolation $p_{\mathrm{T}}^{\mathrm{iso}}(\Delta R \leq 0.2)/p_{\mathrm{T}}^{\mu} < 0.1$
Vertex compatibility	$\lvert d_0/\sigma(d_0)\rvert < 3$ $\lvert z_0\rvert < 10\,\mathrm{mm}$
Number of muons	Exactly one passing the criteria above
Kinematics (2)	$\lvert\eta\rvert < 2.4$

Table 6.2: muon selection requirements.

vectors. By projection of the muon and neutrino momentum onto the transverse plane, the W transverse mass,

$$M_{\mathrm{T}}^{W} = \sqrt{2p_{\mathrm{T}}^{\mu}p_{\mathrm{T}}^{\nu_\mu}(1-\cos(\phi^{\mu}-\phi^{\nu_\mu}))}, \tag{6.2}$$

is obtained, which can be calculated by replacing the transverse momentum of the neutrino with $E_{\mathrm{T}}^{\mathrm{miss}}$:

$$M_{\mathrm{T}}^{W} = \sqrt{2p_{\mathrm{T}}^{\mu}E_{\mathrm{T}}^{\mathrm{miss}}(1-\cos(\phi^{\mu}-\phi^{E_{\mathrm{T}}^{\mathrm{miss}}}))}. \tag{6.3}$$

This distribution peaks at the W mass for events in which the muon and the neutrino are emitted with the same absolute pseudorapidity or θ. For events in which the centre of mass of the interacting partons is boosted along the beam line, the transverse mass takes on lower values. It is required that the transverse mass exceeds 40 GeV.

After the event has been selected, the number of jets is counted. A jet is counted when:

- its p_{T} is greater than 30 GeV. The p_{T} of the jet is calculated in the EM+JES scheme (see Section 4.3.1);
- its rapidity is in the range $|y| < 4.4$;
- the distance of the jet to the muon is $\sqrt{(\Delta\eta)^2 + (\Delta\phi)^2} < 0.5$. This cut is introduced in order not risk a bias in the jet energies by assigning the topoclusters of the muon to the jet. For the $W \to e\nu_e$ + jets analysis this is more important since the electron produces more energetic topoclusters than the muon does. In order to retain compatibility with the electron analysis, this cut also applied on the muon channel. This cut is also applied on the truth-level jet definition (see Section 6.5.2);
- the fraction of tracks associated with the jet originating from the primary vertex is larger than 75 %. Forward jets that have no tracks associated are not subjected to this cut.

6.2 Simulated Data Sets

Simulated data samples have been generated for the signal process and for all of the backgrounds mentioned in the previous paragraph. In Table 6.3 the Monte Carlo samples are listed. The processes are normalised to the cross sections that are listed in the third column.

The $W \to \mu\nu_\mu$ and $Z \to \mu\mu$ samples generated by `AlpGen` [73] are generated in six subsamples with $n = 0, \ldots, 5$ partons in the final state. Parton showering and hadronisation is done by `HERWIG` [17, 18] while `Jimmy` [74] takes care of the underlying event. The MLM matching procedure is applied in order to prevent double counting in the parton shower. The `AlpGen` generator calculates for each subprocess the cross section. The sum of the cross sections for the six samples is corrected to the NNLO cross section calculations [75] for $W \to \mu\nu_\mu$ and $Z \to \mu\mu$[1]:

$$\begin{aligned} \sigma(W \to \mu\nu_\mu) &= 10.46 \pm 0.52\,\mathrm{nb}, \\ \sigma(Z \to \mu^+\mu^-) &= 1.069 \pm 0.054\,\mathrm{nb}. \end{aligned}$$

The values displayed in Table 6.3 are already corrected to these values.

[1] Since the Z mixes with the photon, the process generated is actually $Z/\gamma^* \to \mu\mu$. An invariant mass exceeding 60 GeV is required.

Process	Generator	Cross section (pb)	Filter efficiency
$W \to \mu\nu_\mu + 0p$	AlpGen	8283	1
$W \to \mu\nu_\mu + 1p$	AlpGen	1561	1
$W \to \mu\nu_\mu + 2p$	AlpGen	452.2	1
$W \to \mu\nu_\mu + 3p$	AlpGen	122.0	1
$W \to \mu\nu_\mu + 4p$	AlpGen	30.82	1
$W \to \mu\nu_\mu + 5p$	AlpGen	8.297	1
$W \to \mu\nu_\mu$	Pythia	10.46	1
$W \to \mu\nu_\mu$	Sherpa	10.46	1
$W \to \tau\nu_\tau$	Pythia	10.46×10^3	1
$Z \to \mu\mu + 0p$	AlpGen	833.2	1
$Z \to \mu\mu + 1p$	AlpGen	167.1	1
$Z \to \mu\mu + 2p$	AlpGen	50.25	1
$Z \to \mu\mu + 3p$	AlpGen	13.85	1
$Z \to \mu\mu + 4p$	AlpGen	3.424	1
$Z \to \mu\mu + 5p$	AlpGen	0.9601	1
$Z \to \tau\tau$	Pythia	1069	1
$t\bar{t}$	Powheg	164.6	0.543
WW	HERWIG	17.44	0.388
WZ	HERWIG	5.734	0.308
ZZ	HERWIG	1.265	0.212
single top Wt-channel	MC@NLO	13.10	1
$t \to \mu\nu_\mu$, t-channel	MC@NLO	6.34	1
$t \to \mu\nu_\mu$, s-channel	MC@NLO	0.43	1

Table 6.3: Monte Carlo samples used for the $W \to \mu\nu_\mu$ analysis. The number of radiated partons in the matrix-element calculation for the $W \to \mu\nu_\mu$ and $Z \to \mu\mu$ samples are denoted by np. The filter efficiency is explained in the text.

Two additional samples of the signal process $W \to \mu\nu_\mu$ are generated by `Pythia` [16] and `Sherpa` [21] for the evaluation of the systematic uncertainties. The `Sherpa` sample uses the CKKW algorithm to match partons from the matrix element with the partons in the parton shower.

The $t\bar{t}$ sample is generated using `Powheg` [69] at NLO. A lepton filter is applied at the generation stage, requiring the leptonic decay of the W from the top or anti-top decay. The efficiency of this filter is $\epsilon_{t\bar{t}}^{\text{filter}} = 0.543$. The cross section displayed in Table 6.3 is multiplied by this efficiency in order to obtain the correct normalisation.

Three samples, WW, WZ, ZZ are generated by `HERWIG`. The events are filtered for the presence of an electron or a muon. The following NLO cross sections are used to normalise the samples:

$$\begin{aligned} \sigma(WW) &= 44.9 \pm 2.2\,\text{pb}, \\ \sigma(WZ) &= 18.5 \pm 1.3\,\text{pb}, \\ \sigma(ZZ) &= 5.96 \pm 0.3\,\text{pb}. \end{aligned}$$

These cross sections are production cross sections (i.e. they do not require one of the bosons to decay into muon) and therefore they are multiplied by the filter efficiencies in Table 6.3 in order to obtain the right normalisation. The three samples are summed together to form the diboson background.

The single top background is generated using the `MC@NLO` [76] generator. The three channels of single top, the s-channel, the t-channel and the Wt channel are all generated separately. In the s- and t-channels, the W from the t decay is forced to decay into a muon. This is not identical to applying a filter, since filters are usually applied after the hadronisation and decay. The quoted cross section in the table is therefore the production cross section multiplied by the branching ratio of W decaying into a muon (10.8%). This is not the case for the Wt sample.

The following sets of parton distribution functions (PDF sets) are used in the event generation. For the `AlpGen` samples the `CTEQ6L1` [77] PDF set is used. For the `Pythia` samples the `MRST2007lomod` PDF set [78] is used. The `Sherpa`, `Powheg` and `MC@NLO` samples are generated using the `CTEQ6.6M` set [79].

The QCD sample is a di-jet sample generated by `Pythia`. It is divided in six slices of different p_{T} of the final state partons in the LO $2 \to 2$ process of the hard scattering. A muon filter, requiring at least one muon with $p_{\text{T}} > 8\,\text{GeV}$ and $|\eta| < 3$, is applied at generation phase. The efficiencies and cross sections of the different slices are shown in Table 6.4.

Parton p_{T} (GeV)	Generated cross section (pb)	Filter efficiency
8−17	9.86×10^{9}	6.90×10^{-5}
17−35	6.78×10^{8}	1.15×10^{-3}
35−70	4.10×10^{4}	5.35×10^{-3}
70−140	2.19×10^{3}	1.30×10^{-2}
140−280	8.77×10^{4}	2.21×10^{-2}
280−560	2.35×10^{3}	3.01×10^{-2}

Table 6.4: QCD cross sections and filter efficiencies.

Full detector simulation has been run for the generated events (see Section 3.2.6). This is followed by running reconstruction on the simulated detector response.

6.2.1 Simulation Corrections

The performance of the object identification in the simulated data is corrected to adequately represent the data. In this section the various corrections are covered.

Pile-up

All simulated samples are overlaid with minimum-bias events in order to simulate the effect of pile-up. However, the amount of pile-up simulated does not exactly represent that in the data. Actually, the amount of pile-up continuously increased with increasing instantaneous luminosity during the data taking in 2010. The simulated events are therefore weighted in order to represent the pile-up as observed in data. In Figure 6.1, the data distribution of the number of primary vertices N_{vertex} is compared to the reweighted simulated sample. The pile-up weights are extracted from the N_{vertex} distribution before event selection. This has been done separately for each trigger period. The distributions shown in Figure 6.1 are after the full event selection.

Muon Trigger and Reconstruction

Three different triggers are used in data as listed in Table 6.1. In simulation the trigger required is chosen randomly. The probability to choose one particular trigger is then proportional to the integrated luminosity on data for which this

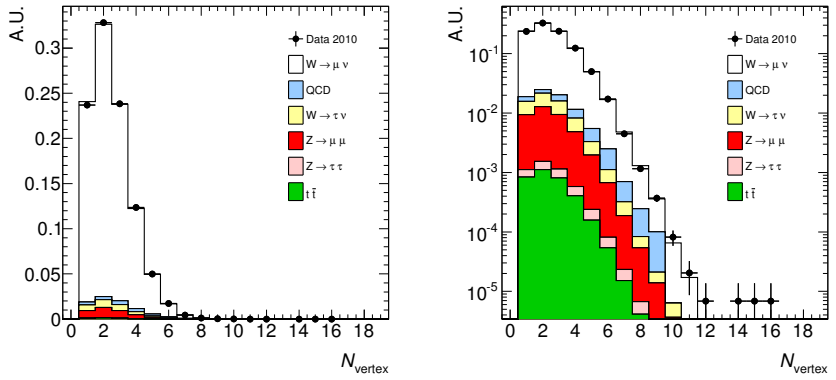

Figure 6.1: the distribution of the number of vertices N_{vertex} after the full event selection after reweighting on a linear scale in 6.1(a) and log-scale in 6.1(b).

trigger was used. Since the instantaneous luminosity increased slowly during the year, the amount of pile-up for the loose triggers is lower than for the tighter ones. The vertex weight mentioned in the previous paragraph takes this into account and is obtained simultaneously with the randomly selected trigger.

As described in Section 4.2.1, the muon efficiency is measured on data using the tag-and-probe method. In bins of η and p_{T}, the ratio of the efficiency measured in data to that in simulation is calculated. This defines a scale factor. Every event in Monte Carlo is weighted with this scale factor in order to represent the efficiency of muon reconstruction in data. The trigger efficiencies have been determined also using the tag-and-probe method [80]. Like for the reconstruction efficiency, the simulated data are reweighted with a scale factor. Separate scale factors have been derived for each trigger period.

The muon momentum resolution is slightly worse in data than in simulation. The simulated momentum resolution can always be tuned better than the resolution in data, since the alignment of the detector is known exactly in simulation. The advantage of this is that the momentum resolution in data can easily be mimicked by smearing simulated momenta. When running over simulated data, the simulated muon transverse momentum p_{T}^{μ} is changed in the following way:

$$p_{\text{T}}^{\prime\mu} \quad = \quad \text{Gauss}\big(p_{\text{T}}^{\mu}(1+\delta(\eta^{\mu})), \sigma_{p_{\text{T}}}^{\mu}(p_{\text{T}}^{\mu}, \eta^{\mu})\big), \tag{6.4}$$

with $\delta(\eta^\mu)$ the deviation of the momentum scale from unity and $\sigma_{p_\mathrm{T}}(p_\mathrm{T}^\mu, \eta^\mu)$, the muon momentum resolution. As explained in Section 4.2.1, the momentum scale and resolution are defined in four bins in η^μ. The dependence of the resolution on p_T^μ is parameterised. Of course this correction is applied before the muon selection is done.

Jets and Missing Transverse Energy

Jet momenta are corrected for the jet energy scale and are smeared with the jet energy resolution. Since the missing transverse energy estimate depends on the measurements of the jet transverse energies and the muon momentum, the smeared values replace the original values and the missing transverse energy is recalculated. The actual smearing values are obtained from the study described in Section 4.3.2.

6.3 Data-Driven QCD Background Estimation

At the LHC, the cross section for QCD multi-jet production is many orders larger than the cross section for W production. A reconstructed muon in QCD events can either originate from experimental effects, like punch-through, or from the decay of a hadron into a muon. The simulation of the QCD processes come with large uncertainties deriving from both theoretical and experimental effects. These uncertainties, magnified by the huge cross section, call for a data-driven estimate of the multi-jets background.

6.3.1 Method

The determination of the yield of multi-jet events starts with a template fit of the missing-transverse-energy distribution in every jet multiplicity bin. In a template fit the sum of two (or more) input distributions, called templates, is fitted to the data. The shapes of the input distributions are fixed and the only free parameters are the relative normalisations of the templates in the summed distribution. The fit is done using two template distributions:

multi-jet events: this distribution is obtained from data by identifying a region which is dominated by multi-jet events;

electroweak and top: this distribution is obtained from simulated data. The signal process and all the backgrounds, except multi-jets, are included and weighted with the predicted cross sections.

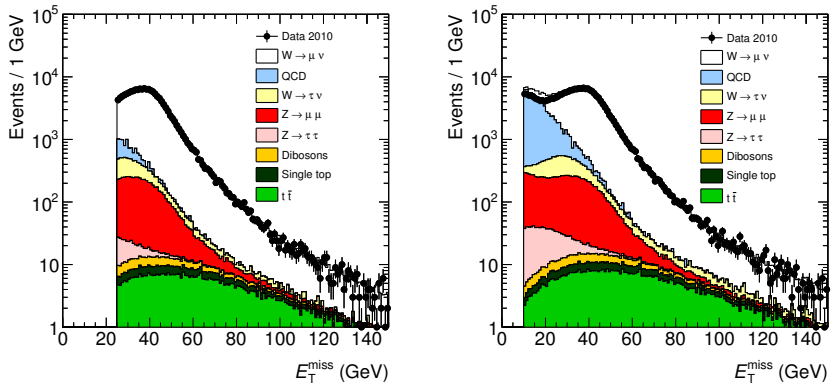

Figure 6.2: the missing transverse energy distribution with standard event selection cuts 6.2(a) and with looser cuts 6.2(b). The QCD distribution is obtained from simulation.

In order for the template fitting procedure to work, the two template distributions should be different. In Figure 6.2(a), the $E_{\mathrm{T}}^{\mathrm{miss}}$ distribution is shown after the standard event selection cuts. In Figure 6.2(b), the distribution of $E_{\mathrm{T}}^{\mathrm{miss}}$ is shown after loosening the following cuts:

- $M_{\mathrm{T}}^{W} > 40\,\mathrm{GeV} \quad \rightarrow \quad M_{\mathrm{T}}^{W} > 20\,\mathrm{GeV}$;
- $E_{\mathrm{T}}^{\mathrm{miss}} > 25\,\mathrm{GeV} \quad \rightarrow \quad E_{\mathrm{T}}^{\mathrm{miss}} > 10\,\mathrm{GeV}$.

Since the QCD distribution is more pronounced with the looser cuts, this has been chosen as a working point for the template fit. However, the QCD yields obtained from the fit, $N_{\mathrm{QCD}}^{\mathrm{fitted}}$, have to be known after applying these cuts. The calculation can be factorised as follows:

$$\begin{aligned} N_{\mathrm{QCD}} \quad = \quad & N_{\mathrm{QCD}}^{\mathrm{fitted}} \cdot f\big(E_{\mathrm{T}}^{\mathrm{miss}} > 25\,\mathrm{GeV}\big) \times \\ & f\big(M_{\mathrm{T}}^{W} > 40\,\mathrm{GeV} \mid E_{\mathrm{T}}^{\mathrm{miss}} > 25\,\mathrm{GeV}\big), \end{aligned} \tag{6.5}$$

where $f(E_{\mathrm{T}}^{\mathrm{miss}} > 25\,\mathrm{GeV})$ is the fraction of QCD events to pass the $E_{\mathrm{T}}^{\mathrm{miss}} > 25\,\mathrm{GeV}$ cut. An equivalent selection efficiency factor, $f(M_{\mathrm{T}}^{W} > 40\,\mathrm{GeV} \mid E_{\mathrm{T}}^{\mathrm{miss}} > 25\,\mathrm{GeV})$, is applied to correct for the looser M_{T}^{W} cut during the fit. These two fractions are derived from data using a control region.

6.3.2 Control Region

The muon production in the multi-jets background is dominated by the decay of heavy flavoured hadrons into a final state with a muon. These hadrons usually have a relatively long lifetime. This effect is measurable by the impact parameter d_0 with respect to the primary vertex.

In Figure 6.3(a), the impact parameter significance is shown. It is visible that the QCD distribution dominates in the region for which $|d_0/\sigma_{d_0}|$ is large. This region is a good candidate for obtaining the $E_{\mathrm{T}}^{\mathrm{miss}}$ and M_{T}^{W} distributions for the multi-jet events in a data-driven way. The baseline selection included required $|d_0/\sigma_{d_0}| < 3$. In this section, this region is called the *signal region*. The *control region* is defined by $|d_0/\sigma_{d_0}| > 3$, which is a reversal of the impact-parameter significance cut in the baseline selection as reported in Table 6.2. In order to be consistent with the baseline selection, an event is put in the control region only if there is exactly one muon with a large impact parameter and if there are no muons that satisfy the signal requirements. If (at least) one signal muon is found, the event is discarded as a control region candidate.

Correlations

In order to obtain correct results using the multi-jet templates from the control region, the control region shapes should be similar to the signal region shapes. Effectively this means that there should be negligible correlations between the impact parameter and the M_{T}^{W} and $E_{\mathrm{T}}^{\mathrm{miss}}$ distributions.

The topology of b jets is not identical to that of c jets. A priori it is not known if the missing transverse energy distribution in the control region is representative of the signal region. The control region will bias towards a higher fraction of b quarks, since the impact parameter of b hadrons is larger on average than that of c hadrons. In Figure 6.3(b) the simulated missing transverse energy distribution is plotted for events where the muon is produced by the decay of a b or a c hadron. The figure shows that the b-flavour bias will not have a large effect on the obtained $E_{\mathrm{T}}^{\mathrm{miss}}$ distribution.

During the development of the fit method it was first tried to use completely relaxed cuts on $E_{\mathrm{T}}^{\mathrm{miss}}$ and M_{T}^{W}. Since the bulk of the QCD events populates the $E_{\mathrm{T}}^{\mathrm{miss}}$ distribution at low values, this leads to a more sensitive fit. In Figure 6.4, the angle between the missing transverse energy and the transverse momentum of the muon are shown for the different jet multiplicities when both the M_{T}^{W} and $E_{\mathrm{T}}^{\mathrm{miss}}$ cuts are completely relaxed. The QCD distribution in this figure is obtained from the control region. For small angles a discrepancy is observed. It

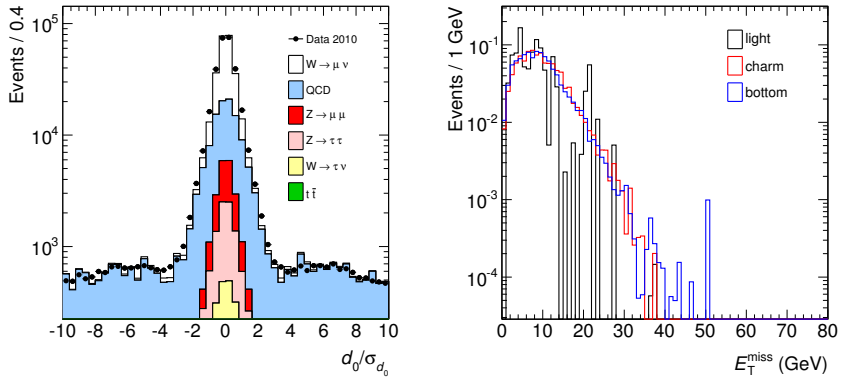

(a) (b)

Figure 6.3: the muon impact parameter significance 6.3(a) and the missing transverse energy distribution for the different flavour components 6.3(b).

is assumed that this is caused by the QCD control box distribution, which does not seem to describe the signal region well for these small angles. As visible in Figure 6.5, the $M_{\mathrm{T}}^{W} > 20\,\mathrm{GeV}$ and $E_{\mathrm{T}}^{\mathrm{miss}} > 10\,\mathrm{GeV}$ cuts help to improve the agreement.

The simulated QCD samples are used to study the behaviour of the control region with respect to the signal region. In Figure 6.6 the predicted missing transverse energy distribution of the control and signal region are compared. The same is done in Figure 6.7 for the transverse mass. The left plot shows a direct comparison of the distributions, while the right plot shows the ratio of the selection fractions obtained in the control region and the signal region as a function of the cut-value. If the control region represents the signal region, this ratio should be equal to one. The statistical uncertainties are indicated by bands around the graphs. The meaning of the dashed, horizontal lines will be explained in Section 6.3.4, which deals with the systematic uncertainties.

Contamination of the Control Region

The control region should be as pure as possible, but it is unfortunately impossible to have no contamination at all. In Figure 6.8, the control-region distributions are shown for the different jet multiplicities. It is visible that the 0-jet bin

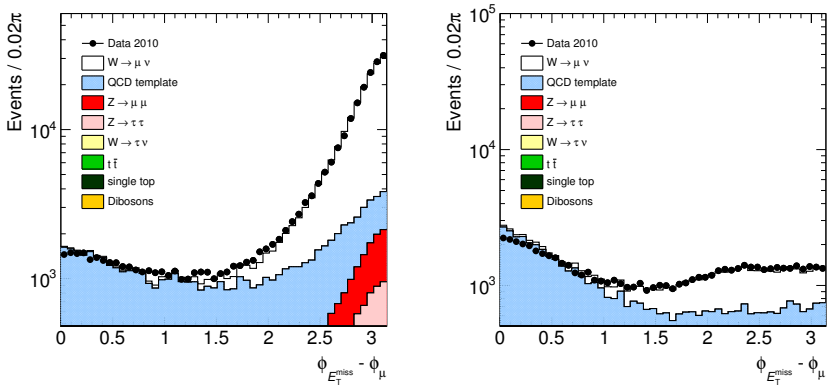

(a) $N_{\text{jets}} = 0$ (b) $N_{\text{jets}} = 1$

(c) $N_{\text{jets}} = 2$ (d) $N_{\text{jets}} = 3$

Figure 6.4: the angle between $E_{\text{T}}^{\text{miss}}$ and muon p_{T} for the different jet multiplicities when no $E_{\text{T}}^{\text{miss}}$ and M_{T}^{W} cuts are applied on the control region.

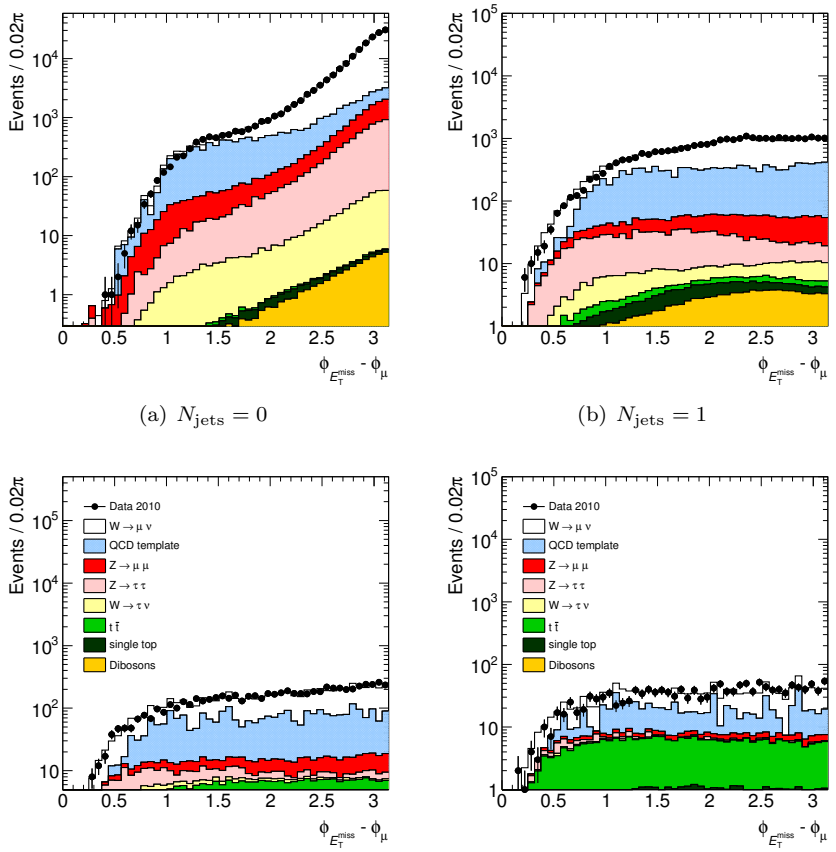

(a) $N_{\text{jets}} = 0$

(b) $N_{\text{jets}} = 1$

(c) $N_{\text{jets}} = 2$

(d) $N_{\text{jets}} = 3$

Figure 6.5: the angle between $E_{\text{T}}^{\text{miss}}$ and muon p_{T} for the different jet multiplicities when $E_{\text{T}}^{\text{miss}} > 10\,\text{GeV}$ and $M_{\text{T}}^{W} > 20\,\text{GeV}$ cuts are applied. The legends for the $N_{\text{jets}} = 0$ and $N_{\text{jets}} = 1$ are omitted because of a lack of space. They are identical to the other figures on this page.

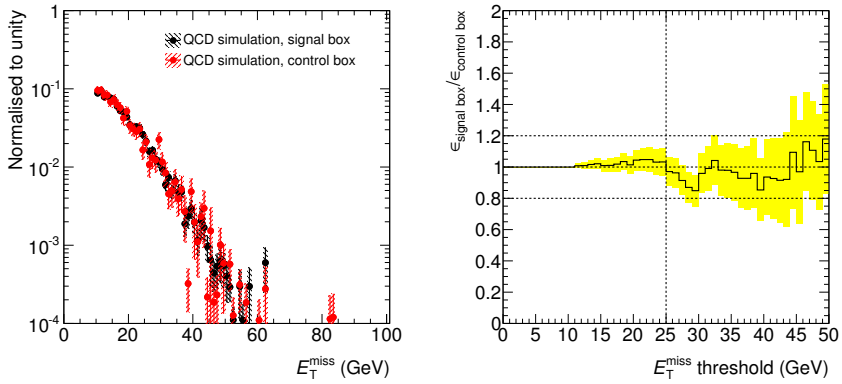

Figure 6.6: comparison of the missing transverse energy distribution in the control box and signal box (a) and the ratio of the selection efficiency of the signal box with the selection efficiency of the control box as a function of cut value (b).

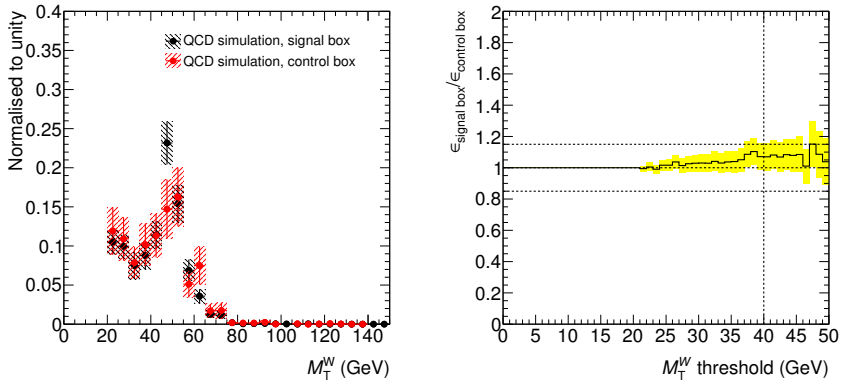

Figure 6.7: comparison of the transverse mass distribution in the control box and signal box (a) and the ratio of the selection efficiency of the signal box with the selection efficiency of the control box as a function of cut value (b).

suffers most from contamination and that the contributing process are $Z \to \tau\tau$ and $W \to \mu\nu_\mu$. The contaminations are also specified per jet multiplicity bin in Table 6.5.

The contaminations are subtracted from the control region using the Monte Carlo predictions. Subtracting the predicted contaminations from the missing transverse energy distribution in the control region leads to a few bins with negative entries. The number of bins for which this is the case is small. Moreover, since the contaminations are mainly located at higher values of $E_{\mathrm{T}}^{\mathrm{miss}}$, this has most profound effect on the determination of the selection efficiencies displayed in Eq. 6.5 and a small effect on the fit results. For this reason the selection efficiencies are calculated in the following way:

$$f(x > x_0) = \frac{\int_{x_0}^{\infty} \mathrm{d}x N_{\mathrm{control}}(x) - \int_{x_0}^{\infty} \mathrm{d}x N_{\mathrm{EW}+t}(x)}{\int_{0}^{\infty} \mathrm{d}x N_{\mathrm{control}}(x) - \int_{0}^{\infty} \mathrm{d}x N_{\mathrm{EW}+t}(x)} \tag{6.6}$$

where $N_{\mathrm{control}}(x)$ is the control region distribution obtained from data and $N_{\mathrm{EW}+t}(x)$ is the sum of the electroweak and top predictions for variable x. The variable x designates $E_{\mathrm{T}}^{\mathrm{miss}}$ or M_{T}^{W} and x_0 is the cut value as shown in Eq. 6.5. For all jet multiplicities there is enough statistics to avoid the problem of having negative entries. In the fit however, the binning is much smaller and few bins have negative entries. These are set to zero. This is then followed by a scaling that restores the integral of the template distribution back to its value before the negative bin correction.

6.3.3 Fit Procedure

As explained before, the fit procedure is a template fit. In contrast to the fit procedure used in Section 4.6, which used an unbinned maximum likelihood fit, here a binned maximum-likelihood fit is used. The log-likelihood used in this method includes an extra term for the statistical uncertainty on the template distributions:

$$\log \mathcal{L} = \sum_i \left(d_i \log f_i - f_i\right) + \sum_{j,i} \left(a_{ji} \log A_{ji} - A_{ji}\right). \tag{6.7}$$

Here i denotes the bin index in the histogram, d_i is the number of events in data in bin i, a_{ji} is the histogram for template j which is drawn from the truth

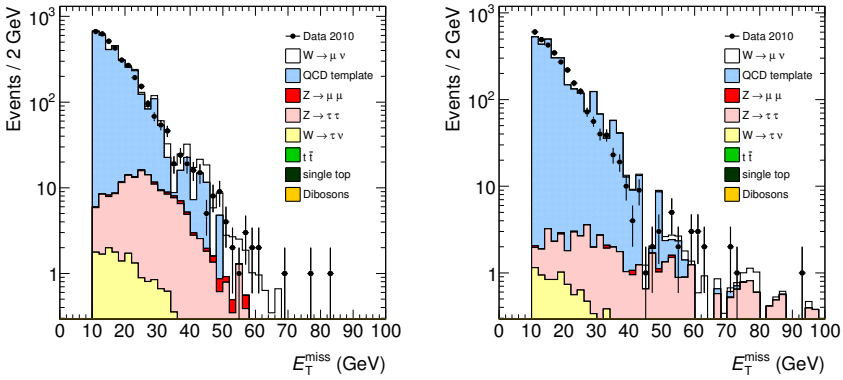

(a) $N_{\text{jets}} = 0$ (b) $N_{\text{jets}} = 1$

(c) $N_{\text{jets}} = 2$ (d) $N_{\text{jets}} = 3$

Figure 6.8: from the top-left to bottom-right, the control box $E_{\text{T}}^{\text{miss}}$ distributions for $N_{\text{jets}} = 0, \ldots, 3$ and $N_{\text{jets}} \geq 4$. The QCD histogram is obtained from the Monte Carlo prediction, but scaled to the event yield in data, which is corrected for the predicted contaminations.

Process	$N_{\text{jets}} = 0$	$N_{\text{jets}} = 1$	$N_{\text{jets}} = 2$	$N_{\text{jets}} = 3$	$N_{\text{jets}} \geq 4$
$W \to \mu\nu_\mu$	3.69 ± 0.10 %	0.38 ± 0.03 %	0.30 ± 0.05 %	0.26 ± 0.07 %	0.43 ± 0.18 %
$Z \to \mu\mu$	0.16 ± 0.02 %	0.03 ± 0.01 %	0.02 ± 0.00 %	0.03 ± 0.01 %	0.02 ± 0.01 %
$Z \to \tau\tau$	4.02 ± 0.16 %	1.52 ± 0.11 %	1.75 ± 0.26 %	0.89 ± 0.34 %	1.51 ± 0.81 %
$W \to \tau\nu_\tau$	0.48 ± 0.02 %	0.35 ± 0.02 %	0.32 ± 0.03 %	0.26 ± 0.06 %	0.18 ± 0.11 %
$t\bar{t}$	0.00 ± 0.00 %	0.01 ± 0.00 %	0.14 ± 0.02 %	0.92 ± 0.10 %	4.08 ± 0.48 %
single t	0.00 ± 0.00 %	0.00 ± 0.00 %	0.02 ± 0.00 %	0.05 ± 0.01 %	0.19 ± 0.04 %
Dibosons	0.00 ± 0.00 %	0.01 ± 0.00 %	0.03 ± 0.00 %	0.04 ± 0.01 %	0.08 ± 0.02 %

Table 6.5: the predicted fraction of events that are contaminating the control region for each process.

N_{jets}	after fit	$E_{\text{T}}^{\text{miss}}$ cut	M_{T}^{W} cut
0	17454 ± 373	1627 ± 98	1193 ± 84
1	10100 ± 241	1159 ± 68	594 ± 48
2	2326 ± 124	461 ± 47	201 ± 31
3	504 ± 58	146 ± 26	57 ± 16
≥ 4	140 ± 37	28 ± 14	16 ± 11

Table 6.6: fitted QCD yields after the template fit and after reapplying the $E_{\text{T}}^{\text{miss}}$ and M_{T}^{W} cuts.

(binned) distribution A_{ji}. The number of predicted events is denoted by f_i and is given by:

$$f_i = \sum_j p_j A_{ji}, \tag{6.8}$$

where p_j is the fraction of template j contributing to bin i. The confidence intervals obtained this way include the statistical uncertainty on the templates as well as the statistical uncertainty on the data. The fit method is described in [81], and is implemented in the `ROOT` framework [70] where it is available under the name of `TFractionFitter`.

In Figure 6.9 the fit results are shown for every jet multiplicity bin. The QCD template distribution obtained from the control region is shown on top of the sum of the predicted distribution of the electroweak and top processes. The open histogram is the fit result which takes the statistical uncertainty on the input templates into account.

In Table 6.6 the fitted QCD yields with relaxed $E_{\text{T}}^{\text{miss}}$ and M_{T}^{W} cuts are reported in the first column. In the second and third columns the yields are calculated when the $E_{\text{T}}^{\text{miss}} > 25\,\text{GeV}$ and the $M_{\text{T}}^{W} > 40\,\text{GeV}$ cuts are respectively applied. The uncertainties in the table are purely statistical.

6.3.4 Systematic Uncertainties

The following systematic uncertainties are taken into account:

- binning dependence of the fit. The number of bins in the $E_{\text{T}}^{\text{miss}}$ histograms used as input to the fit is increased and reduced by a factor of 2.

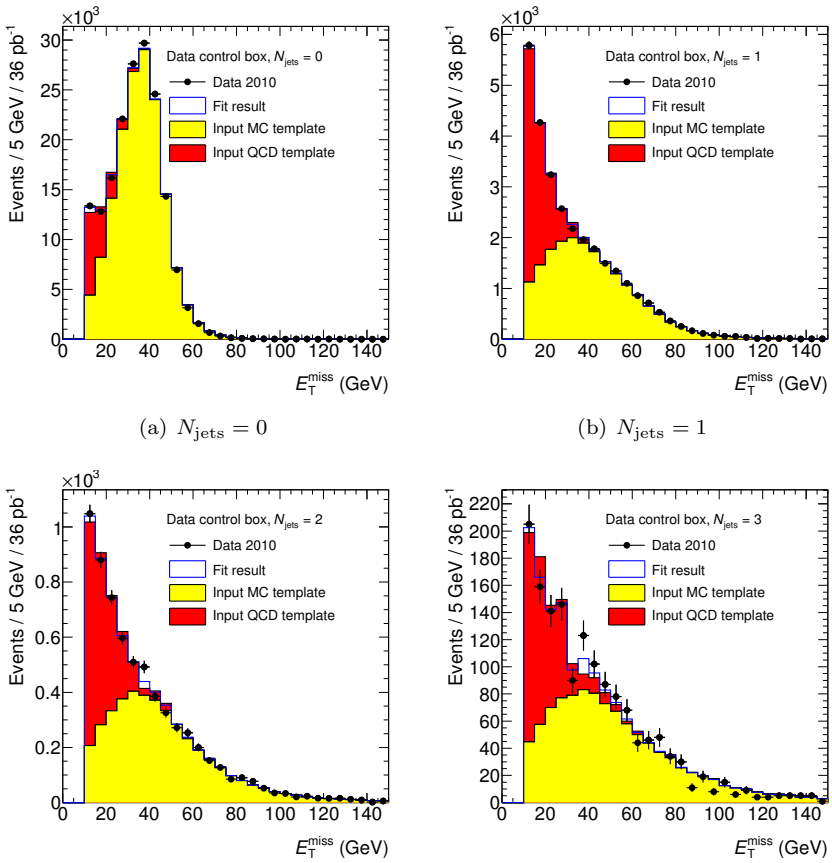

(a) $N_{\text{jets}} = 0$ (b) $N_{\text{jets}} = 1$

(c) $N_{\text{jets}} = 2$ (d) $N_{\text{jets}} = 3$

Figure 6.9: template fit results of the missing transverse energy.

- control-sample contamination. The amount of non-QCD events to be subtracted from the control sample is varied by ±3.4%, following the uncertainty on the integrated luminosity.

- jet energy scale. The jet energy scale influences the templates from simulation by migration of events from one jet bin to another. In addition, the jet energy scale influences the reconstruction of the missing transverse energy and hence the transverse mass. The electroweak template is rebuilt by varying the jet energy scale up and down with its 1σ uncertainty.

- jet energy resolution. The reasoning is identical to why the JES uncertainty is included. The simulated templates are rebuilt by smearing the jet energies with a width that is increased or decreased by 1σ uncertainty on the jet energy resolution relative to simulation.

Each of these systematic effects produces a result which differs from the baseline set-up, as shown in Figure 6.10. All the differences, taken separately per jet multiplicity bin, are added in quadrature to calculate the total systematic uncertainty.

Two additional systematic effects are evaluated as a relative uncertainty common to all jet multiplicity bins:

- fit technique reliability. As a closure test, the fit method is applied to a sample of simulated events (pseudo-data), and the estimated yield is compared to the known yield. In order to have two statistically independent populations of events to build the templates and the pseudo-data, the simulated non-QCD events are split in two subsamples of equal size. The QCD events contributing to the pseudo-data are obtained from the signal region, which is statistically independent from the control region. The QCD sample is therefore not split. The results are summarised in Figure 6.11 for the different jet multiplicity bins. As can be noticed, the estimates are in good agreement with the known yields. The difference between the fitted and true yield, relative to the fitted yields from the closure is multiplied by the fitted yields on data to form the systematic uncertainty.

- $E_{\mathrm{T}}^{\mathrm{miss}}$- and M_{T}^{W}-cut efficiencies. The efficiencies in the simulated signal and control sample are compared in Figure 6.6 and Figure 6.7. A maximum relative variation of 20% and 15% respectively are observed and indicated by the horizontal lines. This translates into an overall relative uncertainty of 25%. The large uncertainty is quite conservative. However,

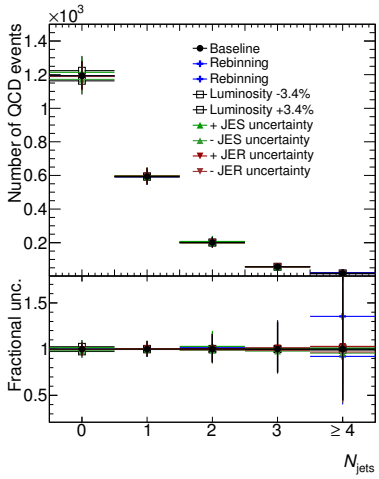

Figure 6.10: the difference of the estimated QCD yields from varying the sources of systematic uncertainty.

the 'oscillations' produced by the limited statistics prevent setting stricter bounds.

6.3.5 Results

In Figure 6.12, the QCD estimates are shown graphically and in Table 6.7 the numbers are given. In the figure, the yellow error bands are formed by summing the statistical and systematic uncertainties.

Up to three jets, the dominant source of uncertainty is the 25% systematic uncertainty on the selection efficiency. In the four-jet bin, the statistical uncertainty becomes comparable to the systematic uncertainty. Within the uncertainties, the Monte Carlo is in agreement with the data-driven results. The prediction is used in Figure 6.13 to show the QCD contribution to the transverse-mass distribution.

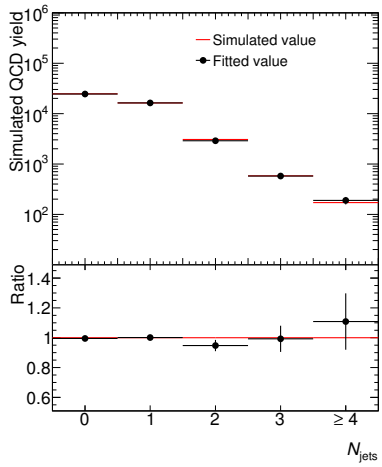

Figure 6.11: the results of the closure test for the template fit of the missing transverse energy.

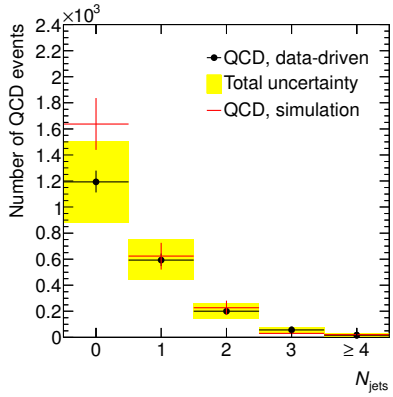

Figure 6.12: final QCD estimates. The bands indicate quadratic sum of the statistical and systematic uncertainty, the error bars indicate the statistical uncertainty only.

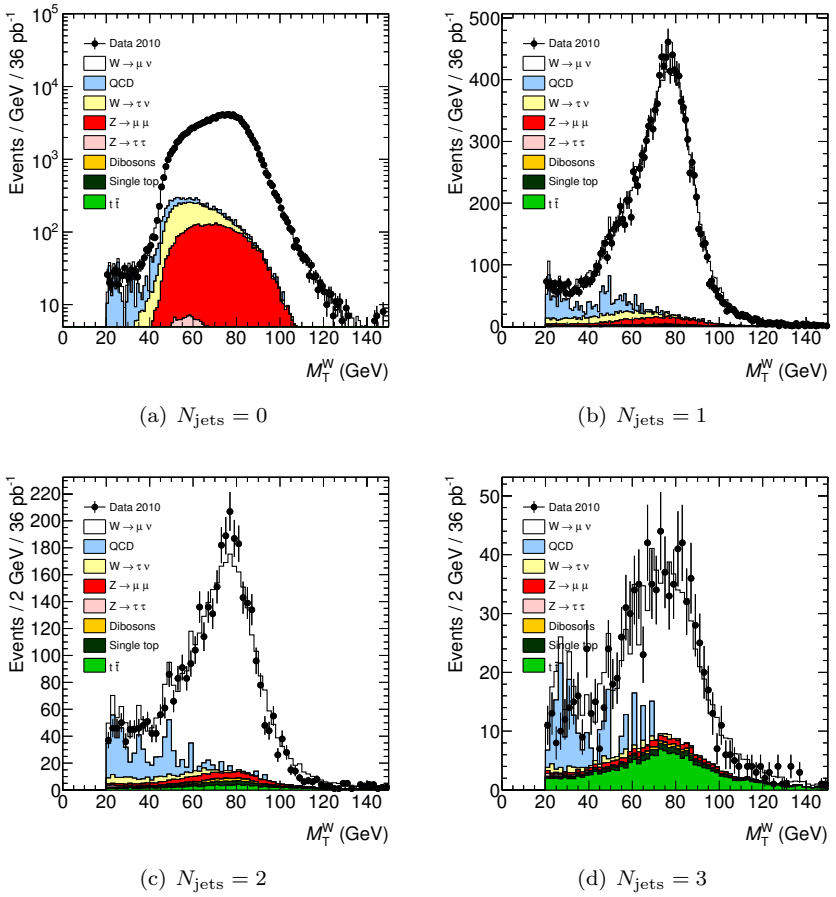

(a) $N_{\text{jets}} = 0$

(b) $N_{\text{jets}} = 1$

(c) $N_{\text{jets}} = 2$

(d) $N_{\text{jets}} = 3$

Figure 6.13: the transverse-mass distributions per jet multiplicity bin using the data-driven templates and fit results.

N_{jets}	Number of QCD events		Data total			Prediction		
0	1193	$^{+86}_{-82}$ (stat.) $^{+301}_{-301}$ (syst.)	130673	±	361	1638	±	199
1	594	$^{+50}_{-47}$ (stat.) $^{+149}_{-149}$ (syst.)	14421	±	120	623	±	103
2	201	$^{+32}_{-29}$ (stat.) $^{+50}_{-51}$ (syst.)	3390	±	58	227	±	55
3	57	$^{+17}_{-14}$ (stat.) $^{+14}_{-14}$ (syst.)	883	±	30	31	±	11
≥ 4	16	$^{+13}_{-9}$ (stat.) $^{+4}_{-7}$ (syst.)	413	±	20	20	±	8

Table 6.7: final results of the QCD estimation procedure.

6.4 Background Subtraction

Except for the multi-jet background, the background estimates are derived from simulated data. As explained in Section 6.2.1, there are many corrections applied. The derivation of these corrections is described in Chapter 4. However, since these corrections come with uncertainties the following systematic uncertainties have to be taken into account with respect to the modelling of the reconstruction in simulation:

Jet energy scale The jet counting is done after shifting the jet energy scale within 1σ uncertainty up and down. The jet energy scale uncertainty depends on η and p_{T}. In addition, the pile-up term depends on the number of the reconstructed primary vertices in the event.

Jet energy resolution The reconstructed energies of the simulated jets are smeared by a Gaussian. After the smearing procedure the jet energy resolution (JER) for the simulated events matches the JER for the events found in data. However, the selection is repeated by modifying the width of the Gaussian within uncertainties.

Trigger efficiency The ratio of the trigger efficiency of the simulated data sets with data is not exactly equal to one. This is taken into account by applying a scale factor $\epsilon_{\text{data}}/\epsilon_{\text{MC}}$ to the weights of the simulated events. The trigger used in simulated data is randomly chosen with probabilities

proportional to the integrated luminosity in which time a trigger is used on data. The scale factor depends on the trigger type, p_{T} and η of the muon. These scale factors are varied between the 1σ uncertainties.

Muon reconstruction efficiency As for the trigger, scale factors have also been derived for the muon reconstruction efficiency. These are p_{T} and η dependent and are also varied within their 1σ uncertainties.

Muon momentum scale The muon momentum scale is a systematic shift applied to the transverse momenta of all muons. It is determined in muon resolution studies and the selection is redone by changing the scale between the 1σ uncertainties. The scale factor only depends on η.

Muon momentum resolution The muon momentum resolution in simulated data is smeared with a Gaussian. The width of the Gaussian is varied within the 1σ uncertainties.

Additionally there are uncertainties not related to the modelling of the detector in simulation. The uncertainty on the luminosity is 3.4% [82]. Since predicted background yields are proportional to the luminosity, they are varied within this uncertainty.

Finally there are theoretical uncertainties on the cross sections. The predicted background yields are varied within the theoretical uncertainties of the cross sections (see Section 6.2).

The multi-jets background is subtracted using the estimated yields derived in Section 6.3.

The final systematic uncertainty is derived from all these samples by the quadratic sum of the differences with respect to the baseline. A comparison of the jet multiplicity spectrum is shown in Figure 6.14. In this figure, the systematic uncertainty on the Monte Carlo prediction is indicated by the shaded area. In Figure 6.15, the background predictions are subtracted from data. The bands indicate the systematic uncertainty due to the background subtraction. This includes the Monte Carlo statistical uncertainty.

6.5 Unfolding

6.5.1 Introduction

The jet multiplicity spectrum as obtained in the previous section is not particularly useful for general theory comparisons, since it depends on the ATLAS

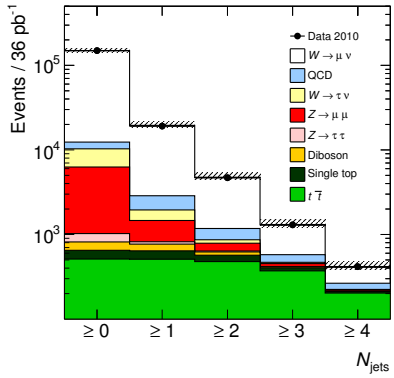

Figure 6.14: the jet multiplicity spectrum. The shaded bands indicate the systematic uncertainty on the Monte Carlo predictions.

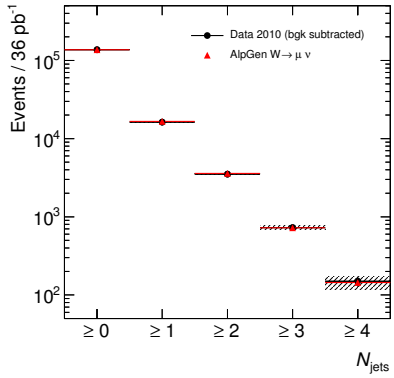

Figure 6.15: the jet multiplicity spectrum after background subtraction. The shaded bands indicate the systematic uncertainty due to the background subtraction and the triangles show the predicted spectrum using the `AlpGen` generator.

detector and status of the reconstruction software. This means that ATLAS specific reconstruction effects are included (folded in) and that the results are not universal: reconstruction-level results from CMS and ATLAS are generally different since both detectors are not identical. The measurements cannot be compared to theory predictions before passing generated events through time consuming detector simulation.

Let the true spectrum of an observable be called $p_{\text{truth}}(x)$ and the spectrum measured in ATLAS $p_{\text{det}}(x)$, then

$$p_{\text{det}}(x) \quad = \quad f\big(p_{\text{truth}}(x)\big), \tag{6.9}$$

where f is called the folding function. The folding function accounts for all detector effects such as detection inefficiencies, instrumental backgrounds and resolution effects. For instance, the folding function f for the jet energy smearing can be expressed in terms of a convolution with a Gaussian:

$$p_{\text{det}}(E_{\text{jet}}) \quad = \quad \int \mathrm{d}E'_{\text{jet}} \cdot p_{\text{truth}}(E'_{\text{jet}}) \cdot \frac{1}{\sqrt{2\pi\sigma^2}} e^{-\frac{(E'_{\text{jet}}-E_{\text{jet}})^2}{2\sigma^2}} \tag{6.10}$$

where σ is the experimental resolution. Here the Gaussian is normalised to unity, but the normalisation factor could also be modified in order to account for jet detection inefficiency. In addition, fake jets due to noise also add to the reconstruction level spectrum. The process of obtaining the truth-level spectrum by determining f and applying the inverse to the reconstruction-level spectrum is called unfolding.

Throughout this section we will often switch between quantities obtained from the simulated spectra, and the spectra obtained in real life. The virtual spectra are denoted with a tilde: e.g. $\tilde{p}_{truth}$ is the generated (truth) spectrum which caused $\tilde{p}_{\text{det}}$ in subsequent simulation. The measured reconstruction level spectrum is denoted p_{det}, while the 'real-life' true distribution is called p_{truth}.

The simplest example of unfolding is *bin-by-bin unfolding*. In this case the spectra of p_{truth} and p_{det} are approximated by histograms. For each bin i, a correction factor c_i is derived from simulated spectra $\tilde{p}_{\text{det}}$, $\tilde{p}_{\text{truth}}$:

$$\tilde{p}_{\text{det},i} \quad = \quad c_i \cdot \tilde{p}_{\text{truth},i}. \tag{6.11}$$

The unfolded spectrum is then easily obtained by inverting the correction factors c_i and applying it to the measured spectrum:

$$p_{\text{truth},i} \quad = \quad \frac{1}{c_i} \cdot p_{\text{det},i}. \tag{6.12}$$

A drawback of bin-by-bin unfolding is that it neglects correlations between bins. A solution is provided by another method called *matrix unfolding*:

$$\tilde{p}_{\mathrm{det},i} = \sum_j C_{ij} \cdot \tilde{p}_{\mathrm{truth},j}, \tag{6.13}$$

where C_{ij} is the unfolding matrix. By matrix inversion:

$$p_{\mathrm{truth},i} = \sum_j \left(C^{-1}\right)_{ij} p_{\mathrm{det},j}, \tag{6.14}$$

the truth-level spectrum can be obtained from the measured spectrum. If the matrix has no large off-diagonal elements, bin-by-bin unfolding is satisfactory. In unfolding the N_{jets} spectrum, this is not the case. In general, bin-by-bin unfolding cannot be used to correct for large resolution effects, since these will automatically imply off-diagonal elements in the unfolding matrix. The drawback of matrix unfolding is that the matrix needs to be inverted, which can magnify statistical fluctuations in the final result. These fluctuations can be suppressed by regularised matrix unfolding [83].

Another method, called Bayesian unfolding, starts from Bayes' theorem:

$$P(C_i|E_j) = \frac{P(E_j|C_i)P(C_i)}{\sum_{i'} P(E_j|C_{i'})P(C_{i'})}, \tag{6.15}$$

where C_i refers to a cause and E_j refers to an event. In this case, C_i, is an event with N true jets, while E_j corresponds to M measured jets. The unfolding matrix is $P(E_j|C_i)$ and is determined from simulation. The truth spectrum prior to the measurement is given by $P(C_i)$ and the inferred truth spectrum given the measurement is $P(C_i|E_j)$. If we calculate $P(C_i|E_j)$, it is possible to estimate the truth distribution:

$$P(C_i) = \frac{1}{\epsilon_i} \sum_j P(C_i|E_j) \frac{n(E_j)}{N}, \tag{6.16}$$

with ϵ_i the efficiency for measuring C_i and N the total number of events generated. Using the estimated truth distribution as the prior to the next iteration, the procedure is iterated until convergence is reached. A detailed description of this method can be found in [84].

6.5.2 Unfolding the Jet Multiplicity Spectrum

In this section the N_{jets} spectrum will be unfolded using Bayesian unfolding. The simulated $W \to \mu\nu_\mu$ events are used to construct the unfolding matrix.

The simulated data sets contain information on the generated particles in the event, the Monte Carlo event record. The anti-k_{T} algorithm (see Section 4.3) is applied on the generated particles for jet finding at truth level. In contrast to jets found in reconstruction, neutrinos and muons are also included. The generator-level jets are subjected to the same kinematic cuts as the reconstruction-level jets:

- $p_{\mathrm{T}} > 30\,\mathrm{GeV}$;
- $|y| < 4.4$;
- $\Delta R(\mathrm{lepton}, \mathrm{jet}) < 0.5$.

Jets that are originating from the overlaid pile-up interactions do not contribute to the number of truth jets.

The cross section measurement is limited to a fiducial region that is defined by the following cuts that resemble the event selection cuts:

- $\tilde{p}_{\mathrm{T}}^{\mu} > 20\,\mathrm{GeV}$;
- $|\tilde{\eta}^{\mu}| < 2.5$;
- $\tilde{p}_{\mathrm{T}}^{\nu_l} > 25\,\mathrm{GeV}$;
- $\tilde{M}_{\mathrm{T}}^{W} > 40\,\mathrm{GeV}$.

Whenever the generated event passes the above cuts, the number of truth jets is counted. If the reconstructed objects in the simulation of the same event passes the reconstruction cuts as described in Section 6.1, the number of reconstruction-level jets are counted. At this point there are four cases:

matched events: the event is selected both by the cuts at truth level and at reconstruction level. Every such event contributes to the unfolding matrix;

inefficiency: the event is located within the fiducial region, but the event is not reconstructed as such. This can be due to quality cuts, reconstruction inefficiencies or migration out of the fiducial region due to detector resolutions;

fake events: the event is not selected within the cross section kinematic region but the event is selected based on the reconstructed object. It should be noted here that the fake events arise mainly at the boundary of the kinematic region where the resolutions of the $E_{\mathrm{T}}^{\mathrm{miss}}$ and muon momentum reconstruction migrate reconstructed events into the kinematic region;

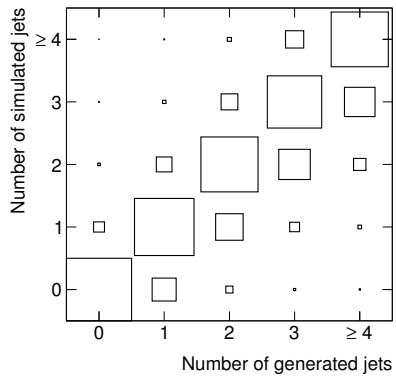

Figure 6.16: the unfolding matrix derived from the `AlpGen` sample. Each column is normalised to unity. The area of the squares is proportional to the size of the matrix elements.

not in fiducial region: this occurs when the event is discarded by both the selection on the event record and the selection on the reconstructed objects. These events are forgotten and do not have any influence on the unfolding.

Corrections for fake entries are done by bin-by-bin unfolding. The unfolding matrix for the `AlpGen` sample is shown in Figure 6.16.

The statistical uncertainties after unfolding are obtained by a *toy Monte Carlo experiment*. An ensemble of new N_{jets} distributions is generated. The bin-averages and bin-spreads of the ensemble are made compatible with the bin-values and bin-statistical uncertainties of the original distribution. This is done by throwing a Gaussian distributed random number centred around the current bin content. The width of this Gaussian is equal to the statistical uncertainty of that particular bin.

Each distribution in the ensemble is unfolded. This provides a distribution for each bin in the unfolded spectrum. The 68% confidence bands are then derived by identifying the region around the central value that contains 68%. The statistical uncertainties indicated in the unfolded spectra are corresponding to the usual 68% confidence intervals.

6.5.3 Systematic Uncertainties

For each source of systematic uncertainty described in Section 6.4, the unfolding matrix is built and the full analysis is repeated. The total systematic uncertainty due to these sources is obtained by taking the square root of the quadratic sum of the differences of each source with respect to the central value obtained using no systematics variations.

In addition to these sources of systematic uncertainty, additional systematic uncertainties are included for the unfolding process:

closure: in Figure 6.17 a closure test of the method is shown for the `AlpGen` and `Sherpa` signal samples. In calculating the closure, the simulated reconstructed spectrum is unfolded and compared to the true distribution. From the figure it is visible that the closure of the method is very good. The differences with respect to unity are largest in the 0-jet bin, where it accounts for less than 0.24‰. Nonetheless, the absolute value of any differences of the ratio with respect to unity are propagated to the systematic uncertainty as a relative uncertainty.

sample: the unfolding method relies on a good description of the unfolding matrix. Since the unfolding matrix is built from truth jets, it depends on the showering algorithms employed in the Monte Carlo generator. To quantify this uncertainty, the unfolding matrix is constructed using the `AlpGen` sample and the `Sherpa` sample. The difference of `Sherpa` with respect to the central value is quadratically added as an additional source of systematic uncertainty. The unfolding matrix for `AlpGen` is

$$\begin{pmatrix} 9.73\times10^{-1} & 1.38\times10^{-1} & 1.29\times10^{-2} & 1.22\times10^{-3} & 4.36\times10^{-4} \\ 2.54\times10^{-2} & 8.04\times10^{-1} & 1.77\times10^{-1} & 2.38\times10^{-2} & 2.48\times10^{-3} \\ 1.37\times10^{-3} & 5.48\times10^{-2} & 7.43\times10^{-1} & 2.31\times10^{-1} & 3.60\times10^{-2} \\ 6.58\times10^{-5} & 2.62\times10^{-3} & 6.29\times10^{-2} & 6.72\times10^{-1} & 2.29\times10^{-1} \\ 7.31\times10^{-6} & 1.42\times10^{-4} & 3.75\times10^{-3} & 7.20\times10^{-2} & 7.32\times10^{-1} \end{pmatrix},$$

while the unfolding matrix for `Sherpa` is

$$\begin{pmatrix} 9.79\times10^{-1} & 1.38\times10^{-1} & 1.64\times10^{-2} & 1.34\times10^{-3} & 0 \\ 2.06\times10^{-2} & 8.11\times10^{-1} & 1.82\times10^{-1} & 2.77\times10^{-2} & 5.51\times10^{-3} \\ 5.21\times10^{-4} & 4.90\times10^{-2} & 7.39\times10^{-1} & 2.41\times10^{-1} & 4.44\times10^{-2} \\ 1.24\times10^{-5} & 2.22\times10^{-3} & 5.91\times10^{-2} & 6.51\times10^{-1} & 2.37\times10^{-1} \\ 5.19\times10^{-7} & 5.21\times10^{-5} & 3.27\times10^{-3} & 7.83\times10^{-2} & 7.13\times10^{-1} \end{pmatrix}.$$

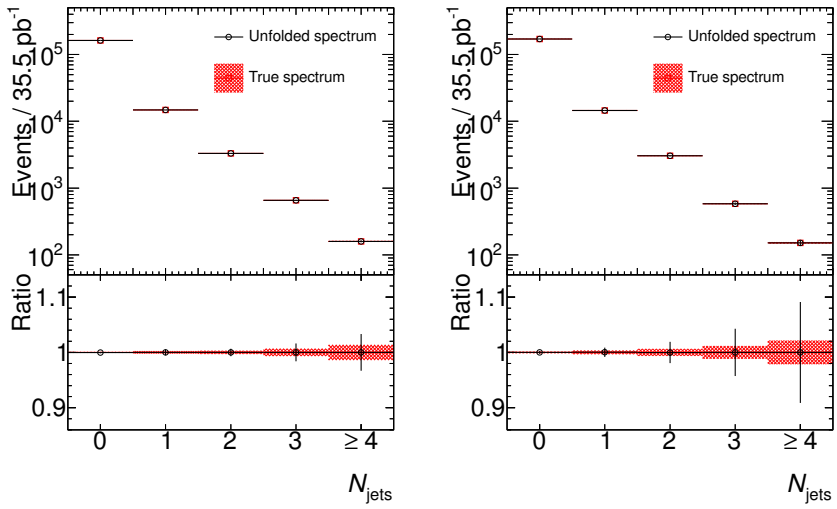

(a) (b)

Figure 6.17: the closure of the method on the `AlpGen` sample (a) and the `Sherpa` sample (b).

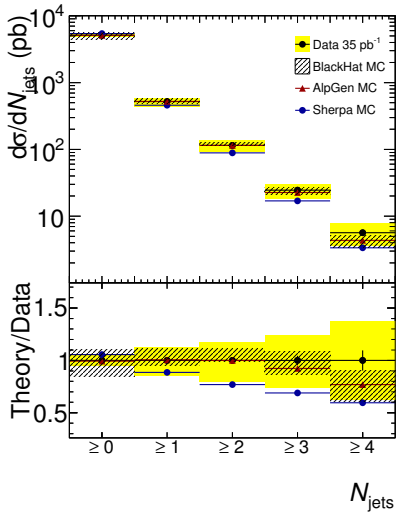

Figure 6.18: the cross section of $W \to \mu\nu_\mu$ as a function of the inclusive number of jets.

6.6 Results

In Figure 6.18, the measured cross section of $W \to \mu\nu_\mu$ is shown as a function of the jet multiplicity. The cross section is computed for the fiducial region as defined in the previous section. Due to the scaling with the inverse of the integrated luminosity, an additional 3.4 % overall systematic uncertainty is added in quadrature. The overview of all systematic uncertainties is given in Table 6.8

The NLO predictions are provided by the `BlackHat-Sherpa` collaboration [85]. The following uncertainties are associated to them:

renormalisation and factorisation scales: the central value for the renormalisation and factorisation scales are set to $H_T/2$. The value H_T is defined as the scalar sum of the transverse momenta of the lepton, neutrino and all the partons. Although usually higher order calculations are less susceptible to changes of these unphysical scales, they were independently varied in four steps between $H_T/4$ and H_T. The largest deviations are taken as the scale uncertainty. This is done independently for each jet bin;

Source	$N_{\text{jets}} \geq 0$	$N_{\text{jets}} \geq 1$	$N_{\text{jets}} \geq 2$	$N_{\text{jets}} \geq 3$	$N_{\text{jets}} \geq 4$
+ JES	0.35%	−10.98%	−15.32%	−21.65%	−32.42%
− JES	−0.31%	9.01%	13.46%	19.84%	32.67%
+ JER	0.00%	−1.86%	−1.88%	−2.49%	−2.65%
− JER	0.00%	1.50%	1.45%	2.18%	3.66%
+ Trigger eff.	−2.11%	−2.61%	−2.91%	−3.83%	−5.46%
− Trigger eff.	2.38%	2.71%	3.03%	4.00%	5.71%
+ μ reco. eff.	−0.88%	−0.90%	−1.02%	−1.35%	−1.88%
− μ reco. eff.	0.94%	0.91%	1.03%	1.37%	1.91%
+ Scale p_{T}^{μ}	−0.16%	−0.20%	−0.18%	−0.23%	−0.38%
− Scale p_{T}^{μ}	0.16%	0.20%	0.17%	0.20%	0.30%
+ Resolution p_{T}^{μ}	0.01%	−0.01%	0.04%	0.01%	0.11%
− Resolution p_{T}^{μ}	−0.01%	0.03%	0.02%	−0.07%	−0.28%
+ QCD	−0.40%	−1.73%	−2.99%	−5.17%	−8.25%
− QCD	0.40%	1.69%	2.82%	4.59%	7.01%
+ background σ	−0.36%	−0.61%	−1.41%	−4.10%	−8.59%
− background σ	0.37%	0.67%	1.76%	5.48%	11.80%
+ Luminosity	−3.53%	−3.70%	−4.16%	−5.50%	−7.64%
− Luminosity	3.78%	3.96%	4.45%	5.89%	8.20%
No JVF cut	0.01%	−2.31%	−3.34%	−4.77%	−6.98%
Unfolding closure	0.00%	0.01%	0.00%	0.00%	0.00%
Unfolding `Sherpa`	3.44%	6.93%	8.20%	7.78%	6.96%
Total	5.75%	12.64%	17.78%	23.75%	37.69%
	−5.48%	−14.24%	−19.92%	−26.08%	−37.41%

Table 6.8: final systematic uncertainties in the $W \to \mu\nu_{\mu}$+jets analysis.

PDF uncertainty: the PDF set CTEQ6.6M [79] is used. This PDF set depends on 22 independent parameters, and the values for these parameters are fixed by many measurements. These parameters are all varied within 1σ uncertainties and the variations in the predicted cross sections are added in quadrature. The MSTW08 [86, 87, 88] and NNPDF2.0 [89] agree within the uncertainty obtained using the envelope.

Moreover three additional uncertainties need to be added to compensate for the fact that `BlackHat-Sherpa` collaboration provided only parton level predictions. These uncertainties are derived from the uncertainties on three correction factors C_{UE}, C_{had} and C_{QED}. They are described below.

The correction factor C_{had} corrects for the hadronisation, i.e. going from parton to particle level. It has been derived using an `AlpGen` $W \to e\nu_e$ sample with no underlying event simulation:

$$C_{\mathrm{had}} = \frac{\sigma(x|\text{particle level})}{\sigma(x|\text{parton level})}, \tag{6.17}$$

where in general $\sigma(x|\text{condition})$ is the differential cross section with respect to observable x given the condition.[2] Two different samples are then created by using `Jimmy` in one case and `Pythia` in the other case to simulate the hadronisation. The baseline value has been taken from the `Jimmy` sample, while the `Pythia` sample is only used to extract the uncertainty.

The correction factor C_{UE} corrects for the missing underlying event simulation in the `BlackHat` sample. It is defined as:

$$C_{\mathrm{UE}} = \frac{\sigma(x|\text{UE on})}{\sigma(x|\text{UE off})}. \tag{6.18}$$

Similarly, `Jimmy` UE simulation has been used to constitute the baseline, while `Pythia` has been used to derive the uncertainty.

Finally, the correction factor C_{QED} corrects for the emission of infrared photons off of the muon. For this purpose the `AlpGen` $W \to \mu\nu_\mu$ sample has been used. The four-momentum of the muon before the emission of photons is now called the *bare muon*, while the *dressed muon* is obtained from summing all the four-momenta in a cone of 0.1 around the muon's initial direction. Similarly to the previous two definitions C_{QED} is defined as

$$C_{\mathrm{QED}} = \frac{\sigma(x|\text{dressed leptons})}{\sigma(x|\text{bare leptons})}. \tag{6.19}$$

[2] In this thesis, only $x = N_{\mathrm{jets}}$ is considered.

The baseline value is derived from `AlpGen`, using `Photos` for photon emission. The uncertainty is derived from a `Sherpa` sample.

As visible from Figure 6.18, the Monte Carlo predictions and the measurement agree very well. The prediction from the `AlpGen` sample agrees with the `BlackHat` sample, but the `Sherpa` sample has a discrepancy especially in the ≥ 2 bin. However, all three predictions are in agreement within the systematic uncertainty of the measurement.

The `Pythia` Monte Carlo sample is not shown. As expected, the `Pythia` sample only agrees well for the low jet multiplicity bins. At higher jet multiplicities, the $2 \rightarrow 2$ matrix-element method of `Pythia` can be ruled out in its current status to predict W + jets backgrounds in analyses where multiple jets are present.

6.7 Discussion

The W + jets process is well suited to study perturbative QCD. Since every process is initiated by two colliding partons at a hadron collider, it essential that the QCD modelling in the event generators is well understood. The Drell-Yan scattering and the W + jets process have been used to study these aspects of QCD in previous experiments as well [90, 91, 92]. This is motivated by the leptonic decay of the Z/γ^* and the W, which provide clear experimental signatures.

Although the W + jets process has already been studied extensively, re-evaluating the predictive power of event generators for this process at the LHC energies is useful for many reasons. First of all, the W + jets process is sensitive to the parton distribution functions. The PDFs can be calculated at a suitable factorisation scale μ_f for the LHC by using the evolution equations. However, this presumes that the PDFs should be known for every value of the momentum fraction x as well as that the parton distributions for all types of partons should be known. Since no experiment can probe the PDFs down to $x = 0$, this means that there is an uncertainty due to the PDFs at the LHC. It should be noted that the production mechanism for W bosons in a $p\overline{p}$ collider is dominated by the valence quarks. Instead at the LHC, a pp collider, at least one of the two colliding partons has to be a sea quark or a gluon.

Another interesting aspect of W + jets production is its dependence on the perturbation expansion in the coupling parameter. This is closely related to the strong coupling α_s and its dependence on the renormalisation scale. The renormalisation scale dependence generally decreases by including higher order

terms. However, these calculations are very difficult and only NLO predictions up to four jets are available with the current computing power and computational techniques.

Similar analyses at the Tevatron [91, 92] have shown that the MCFM generator [93, 94], providing NLO calculations up to $N_{\text{jets}} = 2$, shows good agreements with their measurements. Recent developments from the BlackHat-Sherpa collaboration have extended the NLO calculation up to $N_{\text{jets}} = 4$. As presented in this thesis, the NLO spectrum is in agreement with the data up to these jet multiplicities.

Although not shown explicitly in Figure 6.18, the LO + parton-shower event generation from Pythia does not yield a good description of the jet multiplicity spectrum. Since the LO + parton-shower neglects interference terms, this is not a surprising result. Figure 6.18 shows that the MLM method applied in AlpGen, matching radiated partons at the matrix element level with the partons from the parton shower, provides results that are compatible with the measurement. It is argued that the slightly worse agreement of Sherpa with the measurement is due to a difference of the parameterisation of the renormalisation and factorisation scale [72]. The Sherpa sample uses $\mu^2 = m_W^2 + (p_{\text{T}}^W)^2$, while the AlpGen sample uses $\mu^2 = m_W^2 + \sum_{\text{partons}}(m^2 + p_{\text{T}}^2)$.

A good agreement between Monte-Carlo and data is important for physics studies in which the W boson appears as a background. Although this measurement could in principle be used directly, other analyses typically have other cuts in order to actually reduce the W background. Therefore the W + jets background predictions are usually provided by simulation. A priori it is not known if a safe extrapolation from Tevatron physics, colliding $p\overline{p}$ at a centre-of-mass energy which is about 3.5 times smaller, to LHC physics can be made.

Since jet counting is susceptible to experimental effects such as jet energy calibration and pile-up, studies like these are also perfect tools for commissioning of the detector. At this point the accuracy of the measurement is mainly limited by the jet energy scale uncertainty. This is expected to improve when data driven estimates will become available.

7

Summary and Conclusions

In this thesis three different analyses have been presented, all dealing with muons. In Section 4.6, the raw muon spectrum with very few selection cuts has been examined and the contribution of decays in flight of long-lived light hadrons has been derived. In Chapter 5, an alternative approach to muon reconstruction has been treated. The method described there does not rely on the muon spectrometer, instead it uses the calorimeters for muon identification of inner detector tracks. Finally, the differential cross-section of $W \to \mu\nu_\mu$ with respect to the jet multiplicity has been measured in Chapter 6.

Inclusive Muon Production

At low transverse momentum, muon production is dominated by the decay of light hadrons like pions and kaons. The expected kinks in inner-detector tracks from such decays are hard to detect due to the relatively large relativistic boosts. Also there is the possibility of the decay taking place close to the beam pipe or beyond the acceptance of the inner detector in the calorimeters. Therefore, the method developed relies on the momentum carried away by the neutrino and the energy lost in the calorimeters. For combined muons, a powerful discriminating distribution is the momentum difference of the muon spectrometer track with the inner detector track relative to the momentum measured in the inner detector. The momentum of the muon spectrometer track is extrapolated back to the inner detector, which corrects for the energy lost in the calorimeters and inner

detector. For muons originating from the decay of heavy-flavoured hadrons, the distribution is centred around zero, while the long-lived, light-flavoured hadrons have a tail to larger values.

The fraction of muons originating from light-flavoured hadron decay is estimated through a template fit. The input distributions are obtained from Monte Carlo simulations, but have been validated with data-driven methods. The uncertainty of the result from the shape of the input distributions is quantified by introducing three types of distortions, which are fitted simultaneously as nuisance parameters.

The fraction of light-flavoured hadrons decaying into muons decreases as the momentum of the muon increases. This is expected for two reasons. First, the relativistic boost increases at higher momentum. This increases the expected distance travelled by the hadron, decreasing the probability to decay. Second, the production of heavy-flavoured hadrons, takes place at higher momentum transfer. At the same time, the number of light hadrons rapidly decreases with increasing momentum.

The agreement between the simulated and measured values is not perfect. It is argued that this is caused by the leading-order simulation of the minimum-bias physics which does not reproduce well the heavy-flavoured hadron production.

Calorimeter Muon Identification

The muon is a minimum ionising particle and loses very little energy in the calorimeter. The muon is quite unique in that respect and in ordinary muon reconstruction, which uses the muon spectrometer, the calorimeter is merely used as a muon filter. However, the calorimeter can also be used to identify muons. This is particularly useful in order to recover muons flying through the acceptance gap of the muon spectrometer in the central area $|\eta| < 0.1$. For analyses that involve multiple muons, such as $H \to ZZ \to 4\mu$, the selection efficiency is proportional to the muon reconstruction efficiency to the fourth power. A small efficiency gain therefore can have a large effect. An additional benefit is that this reconstruction algorithm is independent of the muon spectrometer.

An indication of the performance before data taking has been made using inner-detector tracks reconstructed from cosmic muons. As it should be, most of the inner-detector tracks are correctly identified as muons. Cosmic tracks do not necessarily originate from the origin of the detector, so it requires a more general cell-collection procedure than in beam-beam collisions. The fact that the cosmic muons are correctly reconstructed with a high efficiency indicates that the extrapolation works well and that the algorithm is capable of dealing

with tracks that are displaced from the primary vertex.

The collected deposits in data are also compared to the expected deposits from simulation. A good agreement between prediction and measurement is found. This is necessary in order to have reliable performance estimates from Monte Carlo simulations.

The fake rate and efficiency are dependent on variables such as track quality, transverse momentum, psuedorapidity, tag level and isolation. Using the tight cuts displayed in Table 5.5, simulations indicate that the fake rate can be kept reasonably low even in the difficult $t\bar{t}$ process. However, if the calorimeter muons are to be used in physics analysis, a data-driven estimate of the fake rate is desirable.

Since the combined muon efficiency is very high and the fake rate is very low, an estimate of the performance on data is achieved by matching the calorimeter muons to combined muons. The performance estimates obtained in this way do not show unexpected results indicating any particular problem with calorimeter muon reconstruction on data. It should be noted that the estimates obtained in this way are slightly biased due to inefficiency and fakes in combined muon reconstruction.

Finally an outlook is given to exploiting a neural network for calorimeter muon identification. The results on the simulated $t\bar{t}$ sample are promising, but further research needs to be done in order to asses the performance on data and other simulated samples.

Jet Multiplicities in $W \to \mu\nu$ Events

The primary goal of the ATLAS experiment is to find the Higgs boson and, if it exists, new physics. One might wonder why a well-known particle like the W boson is studied in such great detail as it has been here.

A good understanding of the detector is crucial for new-physics searches. This means that all measured quantities should be calibrated correctly and that the performance of the reconstruction algorithms is measured. Only if this is ensured one can trust predictions and their associated uncertainties on the expected number of background events in, for example, a Higgs search. If detector calibrations are wrong, or detector simulation is mismodelled, this will definitely show up in an analyses such as the $W \to \mu\nu_\mu + \text{jets}$ analysis.

For the discovery of new physics, a deep understanding of the background is even more crucial than understanding the properties of the signal. Although in this thesis the $W \to \mu\nu_\mu$ process is treated as signal, for many other physics analyses the $W \to \mu\nu_\mu$ process is a large portion of the background. Any

analysis requiring a single muon and missing transverse energy will be contaminated by $W \to \mu\nu_\mu$ events. An example is the $t\bar{t}$ process, where one W decays into a muon. The $W \to \mu\nu_\mu$ + jets process also constitutes a background for many other other searches such as the $H \to W^+W^- \to \mu^+\mu^-\nu_\mu\overline{\nu}_\mu$ and many supersymmetry channels with one muon and missing energy.

The W + jets analysis also needs to deal with backgrounds from other standard model processes. The modelling of the QCD multijets background is particularly uncertain. In Chapter 6, particular attention is given to a data-driven method for estimating the multijets contribution. The QCD contribution is estimated from a template fit of the $E_{\mathrm{T}}^{\mathrm{miss}}$ distribution where the QCD template is obtained from a control region in data. Since the $E_{\mathrm{T}}^{\mathrm{miss}}$ and M_{T}^{W} cuts have to be loosened for a successful fit, these selection efficiencies are determined from the control region as well and they are applied to the fitted yields. The largest source of systematic uncertainty originates from a possible correlation of the variable defining the control box with the $E_{\mathrm{T}}^{\mathrm{miss}}$ or M_{T}^{W} variables.

From the results in the last chapter it can be concluded that the understanding of the $W \to \mu\nu_\mu$ process is very good. Although over the past years Monte Carlo generators have been tuned to the 1.96 TeV $p\overline{p}$ collisions at the Tevatron they provide an accurate description of the pp collisions at the LHC running at 7 TeV. The particle-level NLO predictions from the `BlackHat-Sherpa` collaboration are in good agreement with the measured distribution. This can also be concluded for the spectrum predicted by `AlpGen` and to a lesser extent for `Sherpa`. Both are using matching schemes (MLM respectively CKKW) in order to predict more accurately the number of jets in the final state.

This measurement is a good test of the modelling of perturbative QCD aspects. Predictions depend on the parton distribution functions, as well as the renormalisation- and factorisation scale. It also shows that the detector simulation needed for such an analysis is in a good state which is a remarkable achievement due to the relative short time span since the start of the LHC.

There are two more points of improvement to this analysis. First, using the 2011 data set, the N_{jets} can be studied at higher jet multiplicities, with $p_{\mathrm{T}}^{\mathrm{jet}} > 30\,\mathrm{GeV}$, than it has been done here. Second, the analysis would benefit from a data-driven derivation of the jet energy scale. At this point the accuracy of the measurement is mainly limited by the uncertainty on the jet energy scale. Many uncertainties on the jet energy scale are now driven by the understanding of the calorimeter response in simulation. Although the jet energy scale is expected to stay the dominant uncertainty, the analysis can still be improved by better understanding of the overall ATLAS performance.

Bibliography

[1] S. Weinberg, *The Quantum Theory of Fields (Volume III, Supersymmetry)*. Cambridge University Press, 2000. (Cited on page 2.)

[2] D. B. Kaplan, H. Georgi, and S. Dimopoulos, *Composite Higgs scalars*, Phys. Lett. **B136** (1984) no. 3, 187 – 190. (Cited on page 2.)

[3] D. F. Litim and T. Plehn, *Signatures of Gravitational Fixed Points at the Large Hadron Collider*, Phys. Rev. Lett. **100** (2008) 131 – 301. (Cited on page 2.)

[4] K. Nakamura (Particle Data Group), *Review of Particle Physics*, Journal of Physics G: Nuclear and Particle Physics **37** (2010) no. 7A, 075021. (Cited on pages 6, 49, and 84.)

[5] G. 't Hooft, *Dimensional regularization and the renormalization group*, Nucl. Phys. **B61** (1973) no. 0, 455 – 468. (Cited on page 6.)

[6] S. Weinberg, *New Approach to the Renormalization Group*, Phys. Rev. **D8** (1973) 3497–3509. (Cited on page 6.)

[7] R. Ellis, W. Stirling, and B. Webber, *QCD and Collider Physics*. Cambridge University Press, 1996. (Cited on pages 6, 13, 18, and 19.)

[8] M. Peskin and D. Schroeder, *An Introduction to Quantum Field Theory*. Perseus Books, 1995. (Cited on pages 6 and 13.)

[9] F. Englert and R. Brout, *Broken Symmetry and the Mass of Gauge Vector Mesons*, Phys. Rev. Lett. **13** (1964) 321–323. (Cited on page 10.)

[10] P. W. Higgs, *Broken Symmetries and the Masses of Gauge Bosons*, Phys. Rev. Lett. **13** (1964) 508–509. (Cited on page 10.)

[11] P. W. Higgs, *Spontaneous Symmetry Breakdown without Massless Bosons*, Phys. Rev. **145** (1966) 1156–1163. (Cited on page 10.)

[12] N. Cabibbo, *Unitary Symmetry and Leptonic Decays*, Phys. Rev. Lett. **10** (1963) 531–533. (Cited on page 12.)

[13] M. Kobayashi and T. Maskawa, *CP-Violation in the Renormalizable Theory of Weak Interaction*, Progress of Theoretical Physics **49** (1973) no. 2, 652–657. (Cited on page 12.)

[14] Z. Maki, M. Nakagawa, and S. Sakata, *Remarks on the Unified Model of Elementary Particles*, Progress of Theoretical Physics **28** (1962) no. 5, 870–880. (Cited on page 12.)

[15] M. Dobbs and J. B. Hansen, *The HepMC C++ Monte Carlo event record for High Energy Physics*, Comp. Phys. Comm. **134** (2001) no. 1, 41 – 46. (Cited on page 14.)

[16] T. Sjostrand, S. Mrenna, and P. Z. Skands, *PYTHIA 6.4 Physics and Manual*, JHEP **05** (2006) 026. (Cited on pages 14, 19, 69, 97, and 121.)

[17] G. Corcella et al., *HERWIG 6: an event generator for hadron emission reactions with interfering gluons (including supersymmetric processes)*, JHEP **01** (2001) 010. (Cited on pages 14, 19, and 119.)

[18] G. Corcella, I. Knowles, G. Marchesini, S. Moretti, K. Odagiri, et al., *HERWIG 6.5 release note*, `arXiv:hep-ph/0210213 [hep-ph]`. (Cited on pages 14 and 119.)

[19] R. R. Wilson, *The Tevatron*, Phys. Today **30N10** (1977) 23–30. (Cited on page 15.)

[20] L. Evans and P. Bryant, *LHC Machine*, JINST **3** (2008) S08001. (Cited on pages 15 and 25.)

[21] T. Gleisberg et al., *Event generation with SHERPA 1.1*, JHEP **02** (2009) 007. (Cited on pages 16 and 121.)

[22] *MSTW PDFs - HepForge*, `http://mstwpdf.hepforge.org/`, 2012. (Cited on page 17.)

[23] S. Catani et al., *QCD matrix elements + parton showers*, JHEP **0111** (2001) 063, `arXiv:hep-ph/0109231 [hep-ph]`. (Cited on pages 19 and 60.)

[24] A. Schalicke and F. Krauss, *Implementing the ME+PS merging algorithm*, JHEP **0507** (2005) 018. (Cited on pages 19 and 60.)

[25] S. Hoeche et al., *Matching parton showers and matrix elements*, `arXiv:hep-ph/0602031 [hep-ph]`. (Cited on pages 19 and 60.)

[26] LEP Injector Study Group, *LEP design report*, Tech. Rep. CERN-LEP-84-01, CERN, Geneva, 1984. (Cited on page 22.)

[27] N. Vogt-Nilsen, H. Blewett, and Organisation Européenne pour la recherche nucléaire, *Proceedings of the* 8^{th} *International Conference on High-energy Accelerators*. European Organization for Nuclear Research (CERN), 1971. (Cited on page 22.)

[28] J.-L. Caron, *The LHC injection complex. L'ensemble d'injection du LHC.*, AC Collection. Legacy of AC. Pictures from 1992 to 2002., May, 1993. (Cited on page 23.)

[29] J.-L. Caron, *Layout of the LEP tunnel including future LHC infrastructures.*, AC Collection. Legacy of AC. Pictures from 1992 to 2002., Feb, 1997. (Cited on page 24.)

[30] The CMS Collaboration, *The CMS experiment at the CERN LHC*, JINST **3** (2008) S08004. (Cited on page 25.)

[31] The LHCb Collaboration, *The LHCb Detector at the LHC*, JINST **3** (2008) S08005. (Cited on page 25.)

[32] J. C. Collins and M. J. Perry, *Superdense Matter: Neutrons or Asymptotically Free Quarks?*, Phys. Rev. Lett. **34** (1975) no. 21, 1353–1356. (Cited on page 25.)

[33] The ALICE Collaboration, *The ALICE experiment at the CERN LHC*, JINST **3** (2008) S08002. (Cited on page 25.)

[34] T. S. Pettersson and P. Lefèvre, *The Large Hadron Collider: conceptual design*, Tech. Rep. CERN-AC-95-05 LHC, CERN, Geneva, Oct, 1995. (Cited on page 25.)

[35] The ATLAS Collaboration, *The ATLAS Experiment at the CERN Large Hadron Collider*, JINST **3** (2008) S08003. (Cited on pages 25 and 57.)

[36] N. Wermes and G. Hallewel, *ATLAS pixel detector: Technical Design Report*. ATLAS-TDR-011. CERN, Geneva, 1998. (Cited on page 30.)

[37] The ATLAS Muon Group, *Monitored Drift Tubes Chambers for Muon Spectroscopy in ATLAS*, Tech. Rep. ATL-MUON-94-044, CERN, Geneva, Jun, 1994. (Cited on page 38.)

[38] S. Agostinelli et al., *G4–a simulation toolkit*, Nucl. Instr. Meth. Phys. Res. **A506** (2003) no. 3, 250 – 303. (Cited on page 42.)

[39] E. Richter-Was, D. Froidevaux, and L. Poggioli, *ATLFAST 2.0 a fast simulation package for ATLAS*, Tech. Rep. ATL-PHYS-98-131, CERN, Geneva, Nov, 1998. (Cited on page 42.)

[40] The ATLAS Collaboration, *Atlas Computing: technical design report*. ATLAS-TDR-017. CERN, Geneva, 2005. (Cited on pages 43 and 85.)

[41] R. Frühwirth, *Application of Kalman filtering to track and vertex fitting*, Nucl. Instr. Meth. Phys. Res. **A262** (1987) no. 2-3, 444 – 450. (Cited on page 45.)

[42] L. Bugge and J. Myrheim, *Tracking and track fitting*, Nuclear Instruments and Methods **179** (1981) no. 2, 365 – 381. (Cited on page 45.)

[43] P. Hough, *A method and means for recognizing complex patterns*, U.S. Patent 3,096,654, 1962. (Cited on page 46.)

[44] J. Illingworth and J. Kittler, *A survey of the Hough transform*, Computer Vision, Graphics, and Image Processing **44** (1988) no. 1, 87 – 116. (Cited on page 46.)

[45] The ATLAS Collaboration, *Performance of primary vertex reconstruction in proton-proton collisions at* $\sqrt{s} = 7\,\text{TeV}$ *in the ATLAS experiment*, Tech. Rep. ATLAS-CONF-2010-069, CERN, Geneva, Jul, 2010. (Cited on page 46.)

[46] R. Frühwirth, W. Waltenberger, and P. Vanlaer, *Adaptive Vertex Fitting*, Tech. Rep. CMS-NOTE-2007-008, CERN, Geneva, Mar, 2007. (Cited on page 46.)

[47] The ATLAS Collaboration, *Alignment of the ATLAS Inner Detector Tracking System with 2010 LHC proton-proton collisions at* $\sqrt{s} = 7\,\text{TeV}$, Tech. Rep. ATLAS-CONF-2011-012, CERN, Geneva, Mar, 2011. (Cited on pages 46 and 48.)

[48] The ATLAS Collaboration, *Determination of the muon reconstruction efficiency in ATLAS at the Z resonance in proton-proton collisons at* $\sqrt{s} = 7\,\text{TeV}$, Tech. Rep. ATLAS-CONF-2011-008, CERN, Geneva, Feb, 2011. (Cited on pages 51, 52, and 53.)

[49] The ATLAS Collaboration, *Muon Momentum Resolution in First Pass Reconstruction of pp Collision Data Recorded by ATLAS in 2010*, Tech. Rep. ATLAS-CONF-2011-046, CERN, Geneva, Mar, 2011. (Cited on pages 54 and 55.)

[50] The ATLAS Collaboration, *Jet energy scale and its systematic uncertainty in proton-proton collisions at* $\sqrt{s} = 7\,\text{TeV}$ *in ATLAS 2010 data*, Tech. Rep. ATLAS-CONF-2011-032, CERN, Geneva, Mar, 2011. (Cited on pages 58, 59, 60, and 61.)

[51] The ATLAS Collaboration, *Study of the Response of the Hadronic Barrel Calorimeter in the ATLAS Combined Test-beam to Pions of Energies from 20 to 350 GeV for Beam Impact Points from 0.2 to 0.65*, Tech. Rep. ATL-TILECAL-PUB-2009-007, CERN, Geneva, Apr, 2009. (Cited on page 59.)

[52] The ATLAS Collaboration, *ATLAS Calorimeter Response to Single Isolated Hadrons and Estimation of the Calorimeter Jet Scale Uncertainty*, Tech. Rep. ATLAS-CONF-2011-028, CERN, Geneva, Mar, 2011. (Cited on page 59.)

[53] The ATLAS Collaboration, *Determination of the ATLAS jet energy measurement uncertainty using photon-jet events in proton-proton collisions at* $\sqrt{s} = 7\,\text{TeV}$, Tech. Rep. ATLAS-CONF-2011-031, CERN, Geneva, Mar, 2011. (Cited on page 60.)

[54] The ATLAS Collaboration, *Measurements of multijet production cross sections in proton-proton collisions at 7 TeV center-of-mass energy with*

the ATLAS Detector, Tech. Rep. ATLAS-CONF-2010-084, CERN, Geneva, Oct, 2010. (Cited on page 60.)

[55] The ATLAS Collaboration, *Jet energy resolution and selection efficiency relative to track jets from in-situ techniques with the ATLAS Detector Using Proton-Proton Collisions at a Center of Mass Energy* $\sqrt{s} = 7\,\text{TeV}$, Tech. Rep. ATLAS-CONF-2010-054, CERN, Geneva, Jul, 2010. (Cited on pages 60 and 62.)

[56] The ATLAS Collaboration, *Data-Quality Requirements and Event Cleaning for Jets and Missing Transverse Energy Reconstruction with the ATLAS Detector in Proton-Proton Collisions at a Center-of-Mass Energy of sqrts* $= 7\,\text{TeV}$, Tech. Rep. ATLAS-CONF-2010-038, CERN, Geneva, Jul, 2010. (Cited on pages 64 and 65.)

[57] The ATLAS Collaboration, *Performance of the Missing Transverse Energy Reconstruction and Calibration in Proton-Proton Collisions at a Center-of-Mass Energy of 7 TeV with the ATLAS Detector*, Tech. Rep. ATLAS-CONF-2010-057, CERN, Geneva, Jul, 2010. (Cited on pages 65 and 66.)

[58] *Proceeding of the* 35^{th} *International Conference of High Energy Physics.* 2010. (Cited on page 68.)

[59] The ATLAS Collaboration, *Extraction of the prompt muon component in inclusive muons produced at* $\sqrt{s} = 7\,\text{TeV}$, Tech. Rep. ATLAS-CONF-2010-075, CERN, Geneva, Jul, 2010. (Cited on page 68.)

[60] The ATLAS Collaboration, *Dimuon composition in ATLAS at 7 TeV*, Tech. Rep. ATLAS-CONF-2011-003, CERN, Geneva, Feb, 2011. (Cited on page 68.)

[61] ATLAS Collaboration, G. Aad et al., *ATLAS Monte Carlo tunes for MC09*, Tech. Rep. ATL-PHYS-PUB-2010-002, CERN, Geneva, Mar, 2010. (Cited on page 70.)

[62] P. Z. Skands, *The Perugia Tunes*, Phys. Rev. **D82** (2010) 074018. (Cited on page 70.)

[63] TeV4LHC QCD Working Group Collaboration, M. G. Albrow et al., *Tevatron-for-LHC Report of the QCD Working Group*, `arXiv:hep-ph/0610012`. (Cited on page 70.)

[64] K. S. Cranmer, *Kernel estimation in high-energy physics*, Comput. Phys. Commun. **136** (2001) 198–207, arXiv:0011057 [hep-ex]. (Cited on page 72.)

[65] S. A. Murphy and A. W. v. d. Vaart, *On Profile Likelihood*, Journal of the American Statistical Association **95** (2000) no. 450, pp. 449–465. (Cited on page 75.)

[66] G. Ordóñez Sanz, *Muon identification in the ATLAS calorimeters*. PhD thesis, Radboud University, Nijmegen, 2009. Presented on 12 Jun 2009. (Cited on page 83.)

[67] C. Ohm, D. Milstead, and T. Moa, *Searches for exotic stable massive particles with the ATLAS experiment*. PhD thesis, Stockholm University, Stockholm, 2011. Presented 04 Nov 2011. (Cited on page 84.)

[68] C. Grupen and B. Schwartz, *Particle Detectors*. Cambridge University Press, 2008. (Cited on page 84.)

[69] S. Alioli, P. Nason, C. Oleari, and E. Re, *A general framework for implementing NLO calculations in shower Monte Carlo programs: the POWHEG BOX*, JHEP **6** (2010) 043. (Cited on pages 97 and 121.)

[70] *ROOT, A Data Analysis Framework*, http://root.cern.ch/. (Cited on pages 110 and 134.)

[71] D. Shanno, *Conditioning of Quasi-Newton Methods for Function Minimization*, Mathematics of Computation **24** (1970) no. 111, 647–656. (Cited on page 110.)

[72] The ATLAS Collaboration, *Study of jets produced in association with a W boson in pp collisions at $\sqrt{s} = 7\,TeV$ with the ATLAS detector*, arXiv:1201.1276 [hep-ex]. (Cited on pages 115 and 153.)

[73] M. L. Mangano et al., *ALPGEN, a generator for hard multiparton processes in hadronic collisions*, JHEP **07** (2003) 001. (Cited on page 119.)

[74] J. Butterworth, J. Forshaw, and M. Seymour, *Multiparton interactions in photoproduction at HERA*, Zeitschrift für Physik C Particles and Fields **72** (1996) 637–646. (Cited on page 119.)

[75] The ATLAS collaboration, *Measurement of the $W \to l\nu$ production cross-section and observation of $Z \to ll$ production in proton-proton collisions at $\sqrt{s} = 7\,\text{TeV}$ with the ATLAS detector*, Tech. Rep. ATLAS-CONF-2010-051, CERN, Geneva, Jul, 2010. (Cited on page 119.)

[76] S. Frixione and B. R. Webber, *The MC@NLO 3.3 Event Generator*, `arXiv:hep-ph/0612272 [hep-ph]`. (Cited on page 121.)

[77] J. Pumplin, D. R. Stump, J. Huston, H.-L. Lai, P. Nadolsky, and W.-K. Tung, *New Generation of Parton Distributions with Uncertainties from Global QCD Analysis*, JHEP (2002) no. 07, 012. (Cited on page 121.)

[78] A. Sherstnev and R. Thorne, *Parton distributions for LO generators*, Eur. Phys. J. **C55** (2008) 553–575. (Cited on page 121.)

[79] P. M. Nadolsky et al., *Implications of CTEQ global analysis for collider observables*, Phys. Rev. **D78** (2008) 013004. (Cited on pages 121 and 151.)

[80] The ATLAS Collaboration, *Performance of the ATLAS Muon Trigger in p-p collisions at $\sqrt{s} = 7TeV$*, Tech. Rep. ATLAS-CONF-2010-095, CERN, Geneva, Oct, 2010. (Cited on page 123.)

[81] R. Barlow and C. Beeston, *Fitting using finite Monte Carlo samples*, Comp. Phys. Comm. **77** (1993) no. 2, 219 – 228. (Cited on page 134.)

[82] The ATLAS Collaboration, *Luminosity Determination in pp Collisions at $\sqrt{s} = 7\,\text{TeV}$ Using the ATLAS Detector at the LHC*, Eur. Phys. J. **C71** (2011) 1630. (Cited on page 141.)

[83] A. Hoecker and V. Kartvelishvili, *SVD approach to data unfolding*, Nucl. Instr. Meth. Phys. Res. **A372** (1996) 469–481. (Cited on page 144.)

[84] G. D'Agostini, *A Multidimensional unfolding method based on Bayes' theorem*, Nucl. Instr. Meth. Phys. Res. **A362** (1995) 487–498. (Cited on page 144.)

[85] C. Berger, Z. Bern, L. J. Dixon, F. Febres Cordero, D. Forde, et al., *Precise Predictions for W + 3 Jet Production at Hadron Colliders*, Phys. Rev. Lett. **102** (2009) 222001. (Cited on page 149.)

[86] A. Martin, W. Stirling, R. Thorne, and G. Watt, *Parton distributions for the LHC*, Eur. Phys. J. **C63** (2009) 189–285. (Cited on page 151.)

[87] A. Martin, W. Stirling, R. Thorne, and G. Watt, *Uncertainties on α_s in global PDF analyses and implications for predicted hadronic cross sections*, Eur. Phys. J. **C64** (2009) 653–680. (Cited on page 151.)

[88] A. Martin, W. Stirling, R. Thorne, and G. Watt, *Heavy-quark mass dependence in global PDF analyses and 3- and 4-flavour parton distributions*, Eur. Phys. J. **C70** (2010) 51–72. (Cited on page 151.)

[89] R. D. Ball, L. Del Debbio, S. Forte, A. Guffanti, J. I. Latorre, et al., *A first unbiased global NLO determination of parton distributions and their uncertainties*, Nucl. Phys. **B838** (2010) 136–206. (Cited on page 151.)

[90] The UA2 Collaboration, *A determination of the strong coupling constant α_s from W production at the CERN $p\overline{p}$ collider*, Phys. Lett. **B263** (1991) 563 – 572. (Cited on page 152.)

[91] The CDF Collaboration, *Measurement of the cross section for W-boson production in association with jets in $p\overline{p}$ collisions at $\sqrt{s} = 1.96\,\text{TeV}$*, Phys. Rev. **D77** (2008) 011108. (Cited on pages 152 and 153.)

[92] The DØ Collaboration, *Measurements of inclusive W + jets production rates as a function of jet transverse momentum in collisions at $\sqrt{s} = 1.96\,\text{TeV}$*, Phys. Lett. **B705** (2011) no. 3, 200 – 207. (Cited on pages 152 and 153.)

[93] J. Campbell and R. K. Ellis, *Next-to-leading order corrections to $W + 2$ jet and $Z + 2$ jet production at hadron colliders*, Phys. Rev. **D65** (2002) 113007. (Cited on page 153.)

[94] J. Campbell, R. K. Ellis, and D. Rainwater, *Next-to-leading order QCD predictions for $W + 2$ jet and $Z + 2$ jet production at the CERN LHC*, Phys. Rev. **D68** (2003) 094021. (Cited on page 153.)

Nederlandse Samenvatting

In dit proefschrift zijn drie verschillende analyses beschreven. In al deze analyses speelt het muondeeltje een rol. In paragraaf 4.6 is het muonspectrum bestudeerd waarbij er slechts lichte selectiecriteria op de gereconstrueerde muonen worden toegepast. In het bijzonder is gekeken naar de bijdrage van het verval van lichte hadronen naar muonen. Een alternatieve methode voor muonreconstructie is beschreven in hoofdstuk 5. Deze methode gebruikt slechts informatie uit de calorimeter om geladen deeltjes als muonen aan te merken en is daarom volledig onafhankelijk van het muon systeem. In het laatste hoofdstuk, hoofdstuk 6, is de werkzame doorsnede voor het $W \to \mu\nu_\mu$ proces in proton-proton botsingen als functie van het aantal jets gemeten.

Inclusieve Muon Productie

In het inclusieve muonspectrum speelt het geen rol door welk proces het muon geproduceerd is. De dominante bijdrage bij een geringe transversale impuls van het muon ten opzicht van de bundelrichting is het verval van hadronen met een kleine massa. De knik in het spoor die bij zo'n verval optreedt is vaak slecht waarneembaar vanwege de relatief grote relativistische impulsen. Tevens is er de mogelijkheid dat een deeltje nog voor de binnenste gevoelige lagen van de sporenkamers vervalt of er doorheen schiet en vervolgens vervalt in de calorimeter. De ontwikkelde methode is daarom gebaseerd op het verschil in impuls, veroorzaakt door de impuls van het neutrino en, bij een laat verval, een hoger energieverlies in de calorimeters. Voor muonen, die gereconstrueerd zijn door middel van het combineren van metingen in het muonsysteem en de

sporenkamer (gecombineerde muonen), blijkt het verschil van de impulsmetingen in beide systemen een onderscheidende variabele te zijn. Hiervoor dient wel de gemeten impuls gecorrigeerd te worden voor energieverlies in de calorimeter. De distributie in deze variabele is gecentreerd rondom de waarde nul voor muonen die afkomstig zijn van zware hadronen of direct verval van andere zware deeltjes. Voor de muonen die geproduceerd worden door het verval van lichte hadronen met een lange levensduur heeft de distributie een staart naar hogere waardes.

De fractie van de muonen, afkomstig van het verval van een lichte hadronen, wordt geschat door middel van een fit. Hierbij wordt het gemeten spectrum gefit aan de som van de twee sjabloondistributies die zijn bepaald door middel van Monte Carlo simulaties. Hoewel de sjabloondistributies geverifieerd zijn door ze te vergelijken met de data, is de onzekerheid in deze distributies gekwantificeerd door geparameteriseerde verstoringen toe te laten. Deze verstoringsparameters worden simultaan gefit als 'lastparameters' (zgn. nuisance parameters). Hierdoor wordt de onzekerheid die deze verstoringen introduceren in het fitresultaat meegenomen.

De fractie van lichte hadronen, vervallend in muonen, wordt kleiner naarmate de transversale impuls van het muon groter wordt. Hiervoor kunnen twee verklaringen gegeven worden. Ten eerste wordt, vanwege een grotere tijdsdilatatie, de verwachte afgelegde afstand van het vervallende hadron groter naarmate zijn energie toeneemt. Ten tweede vindt de productie van zware hadronen plaats bij een grotere impulsoverdracht tussen de protonen. Hierdoor hebben deze hadronen veelal een grotere impuls. Tevens neemt het aantal lichte hadronen snel af naarmate de transversale impuls toeneemt.

De overeenstemming tussen data en simulatie is niet perfect. Dit wordt toegedicht aan het feit dat de simulatie is gebaseerd op laagste orde termen, waardoor de simulatie van de productie van zware hadronen niet perfect is.

Identificatie van Muonen in de Calorimeter

De muonen die typisch geproduceerd worden bij de LHC verliezen weinig energie in de calorimeter. Dit is uniek voor het muon deeltje en de gangbare muonreconstructie maakt hiervan gebruik door de calorimeter te gebruiken als muonfilter. Het lage energieverlies van het muon in de calorimeter kan ook worden aangewend om muonen te detecteren. In het bijzonder kan dit gebruikt worden om muonen te detecteren die door een ongeïnstrumenteerd gebied in het muonsysteem in de centrale regio, $|\eta| < 0.1$, passeren. Vooral in analyses waarin veel muonen worden geëist, zoals dat voor de $H \to ZZ \to 4\mu$ analyse het geval

is, kan een kleine verbetering in de efficiëntie van de reconstructie leiden tot een aanzienlijk groter aantal geselecteerde gebeurtenissen.

Door het algoritme toe te passen op data van kosmische muonen is een indicatie van de prestatie van het algoritme gegeven in de tijd dat er nog geen proton-proton botsingen plaatsvonden. Zoals verwacht, worden de meeste geladen sporen correct aangeduid als een muon. Omdat de sporen die de kosmische muonen achterlaten niet noodzakelijk vanuit het midden van de detector komen is een algemenere procedure nodig om de juiste cellen aan te merken welke het muon doorkruist dan voor proton-proton botsingen. De hoge efficiëntie gezien in de analyse van kosmische muonen geeft aan dat het algoritme in staat is om deze sporen juist te extrapoleren door de calorimeter en dat het dus ook in staat is om muonen te herkennen die sporen achterlaten die niet noodzakelijk gericht zijn naar het centrum van de detector.

De energiedeposities in de calorimeter in data zijn ook vergeleken met simulaties. Deze blijken goed overeen te komen. Dit is noodzakelijk om betrouwbare verwachtingen te hebben ten aanzien van de prestaties van het algoritme.

De frequentie waarin een spoor foutief wordt aangemerkt als een muon alsmede de efficiëntie zijn afhankelijk van de kwaliteit van het spoor, zijn aangemerkte transversale impuls, azimutale hoek, isolatie en het kwaliteitsniveau dat het algoritme zelf geeft. Gebruikmakende van de strenge kwaliteitssnedes in Tabel 5.5 is aangetoond met behulp van simulatie dat de frequentie waarin een spoor foutief wordt aangemerkt als een muon relatief laag gehouden kan worden, zelfs voor het moeilijk $t\bar{t}$ proces. Echter, een herevaluatie hiervan, op basis van de data, is wenselijk als calorimeter muonen worden gebruikt in fysica-analyses.

Door de calorimeter muonen te vergelijken met gecombineerde muonen kan een schatting gemaakt worden hoe goed de prestaties van het algoritme op data zijn. Dit is mogelijk omdat de reconstructie van gecombineerde muonen erg zuiver en efficiënt is. Deze resultaten laten geen onverwachte problemen zien als het algoritme op data werkt. Het moet worden opgemerkt dat, ondanks de goede prestaties van gecombineerde reconstructie, deze schattingen niet volledig zuiver zijn omdat ook de gecombineerde reconstructie niet volledig perfect is.

Ten slotte wordt er gekeken naar de mogelijkheid om neurale netwerken toe te passen in het identificatieproces. De resultaten op gesimuleerde $t\bar{t}$ data zien er veelbelovend uit, maar meer onderzoek zal moeten worden verricht naar de prestaties op andere processen en op data.

Jet Multipliciteiten in het $W \to \mu\nu$ Proces

Het hoofddoel van het ATLAS experiment is het vinden van het Higgsboson, alsmede het zoeken naar nieuwe fysica. De lezer kan zich afvragen waarom het W-boson in zulk groot detail is bestudeerd als hier in dit proefschrift.

Een goed begrip van de detector is cruciaal voordat nieuwe fysica gevonden kan worden. Dit houdt in dat de relevante gemeten grootheden correct gekalibreerd moeten zijn, en dat de prestaties van de reconstructie-algoritmes gemeten is. Slechts wanneer dit het geval is, kan men de simulaties van de bekende fysica vertrouwen die verwachtingen geven voor de hoeveelheid achtergrond in een zoektocht naar bijvoorbeeld het Higgsboson. Als er problemen zijn met de kalibratie of als de detectorsimulatie verkeerd is gemodelleerd, zal dit zeker tot uiting komen in de W + jets analyse.

Om nieuwe fysica te ontdekken is een goed begrip van de achtergrond vaak essentiëler dan een goed begrip van het signaal. Hoewel in dit proefschrift het W + jets proces wordt behandeld als signaal, is het voor veel andere fysica-analyses juist een achtergrond. Elke fysica-analyse die selecteert op tenminste één muon en ontbrekende transversale impuls, welke een maat is voor de energie van niet detecteerbare deeltjes zoals het neutrino, zal in meer of mindere mate te maken hebben met de W+jets achtergrond. Voorbeelden hiervan zijn o.a. het $t\bar{t}$-proces en de zoektocht naar het Higgsboson in het $H \to W^+W^- \to \mu^+\mu^-\overline{\nu}_\mu\nu_\mu$ kanaal. Veel vervalskanalen van zoektochten naar supersymmetrie eisen een muon en ontbrekende transversale impuls.

De W + jets analyse heeft zelf ook te maken met achtergronden van processen uit het standaardmodel. In het bijzonder zijn de onzekerheden bij het modelleren van de productie van meerdere jets via QCD processen groot. In hoofdstuk 6 is aandacht besteed aan de ontwikkeling van een methode om uit de data de bijdrage van QCD processen te schatten. Dit wordt bepaald door middel van een fit met sjabloondistributies aan de $E_{\mathrm{T}}^{\mathrm{miss}}$-distributie in data. De QCD sjabloondistributie is in de data geïsoleerd. Om een succesvolle fit te bewerkstelligen moeten de $E_{\mathrm{T}}^{\mathrm{miss}}$- en M_{T}^{W}-snedes geopend worden. Na de fit worden deze selectie-efficiënties weer aangebracht door deze uit dezelfde controleregio te bepalen. Het niet kunnen uitsluiten van correlaties tussen de variabele die nodig is om de QCD processen te isoleren en de $E_{\mathrm{T}}^{\mathrm{miss}}$- en M_{T}^{W}-variabelen vormt hierbij de grootste bron van systematische onzekerheid.

De resultaten van het vorige hoofdstuk laten zien dat het begrip van het W + jets proces al erg goed is. De Monte Carlo generatoren zijn met behulp van 1.96 TeV $p\overline{p}$ botsingen op het Tevatron al goed getest, maar dit betekent niet noodzakelijk dat ze in staat zijn de LHC processen te beschrijven. De

berekeningen die door de `BlackHat-Sherpa` collaboratie zijn gemaakt, geven een goede beschrijving van het spectrum op deeltjesniveau. In deze berekeningen zijn hogere-order termen meegenomen. De overeenstemming valt binnen de onzekerheid van de meting. Hetzelfde kan gezegd worden voor de voorspelling van `AlpGen` en in mindere mate voor die van `Sherpa`.

Deze meting is een goede test voor bepaalde aspecten van de storingstheorie voor QCD. De voorspellingen hangen niet alleen af van de partonische distributiefuncties, maar ook van de renormalisatie- en factorisatieschalen. Overigens laat deze meting ook zien dat de detectorsimulatie al in een goede staat verkeert ondanks dat de LHC nog maar kort operationeel is.

Deze analyse kan op twee punten verbeterd worden. Met een hogere geïntegreerde luminositeit is het mogelijk om te kijken naar hogere jetmultipliciteiten dan hier gedaan is. Tevens zal de kalibratie van de jetenergieën, door gebruik te maken van data, minder grote systematische onzekerheden hebben dan nu het geval is. Momenteel is deze kalibratie de limiterende factor voor grotere precisie. Hoewel in deze analyse zeer waarschijnlijk kalibratie van de jetenergieën dominant blijft zal de precisie van analyse verbeteren naarmate de ATLAS detector nog beter begrepen is.

Acknowledgements

This thesis could not have been finished without the help of many people. First and most importantly, I would like to thank my promotor, Nicolo de Groot and my co-promotor, Frank Filthaut. Thank you for enabling me to work on such a large, prestigious project as ATLAS. I enjoyed being a part of the team that is venturing in the unexplored realms of fundamental physics.

I cannot forget to mention those that I worked with. Gustavo Ordoñez explained to me the main ideas behind CaloMuon tagging and Peter Kluit helped me getting started writing my first pieces of code in the bulky Athena framework. In the beginning I also worked on a Higgs analysis with John Ottersbach, Max Baak and Rikard Sandström. Although we never matured this analysis, I have definitely learned a great deal from this study. During my period at CERN, I closely worked together with Michele Consonni. Michele, thanks for being a pleasant office mate. I very much enjoyed working together with you. Many of the analyses presented in this thesis were developed through close collaboration with you.

In Nijmegen heb ik een fantastische tijd beleefd op de afdeling EHEF. Op de afdeling heerste altijd een goede sfeer en was er altijd animo voor een goede discussie over fysica en niet-fysica. Ik wil de hele afdeling bedanken voor het neerzetten van deze goede sfeer. In het bijzonder bedank ik het secretariaat, Marjo, Gemma en Annelies, voor het soepel laten verlopen van alle administratieve zaken. Antonio, Folkert, Geert-Jan, Gijs, Guus, Harm, Irene, José, Lucian, Magda, Melvin, Stefan J., Stefan G., Thijs, Yari, Yiannis, bedankt! Veel van jullie waren meer dan collega's en zag ik ook buiten werktijd: tijdens het wielrennen, in de kroeg, bij optredens, vakanties, etc.

Acknowledgements

I really enjoyed my time at CERN. Ido, John, Nicole, Rikard, many thanks for the raclette and 'kolonisten-evenings'. Although Nicole almost always won, it was still a lot of fun. Daan, Jochem, Niels, Nigel, thanks for the many cycling tours we did. Especially the tour around lake Geneva was great!

Mijn vrienden buiten werk om zijn altijd ook erg belangrijk voor mij geweest. Elise, Ellen, Niels, bedankt voor jullie jarenlange vriendschap en de ontelbare gezellige momenten. Ivo en Mathew, bedankt voor de urenlange jamsessies. Edward, Eeuwke, Pascal en Raymond, bedankt voor het rocken op de vele donderdagavonden. Ik hoop dat we binnenkort het publiek weer eens gaan trakteren op een mooie show!

Als laatste wil ik mijn ouders en mijn zus bedanken. Dankjewel voor de goede zorgen gedurende al die jaren, ook lang voordat mijn promotie begon.